Universidad de Oviedo
Universidá d'Uviéu
University of Oviedo

Programa de Doctorado en Materiales

Study of processes with a pair of top-antitop quarks and missing transverse energy in the final state in proton-proton collisions with the CMS detector at the Run 2 of the LHC

TESIS DOCTORAL

Juan Rodrigo González Fernández

Mayo 2019

Universidad de Oviedo

Universidá d'Uviéu

University of Oviedo

Programa de Doctorado en Materiales

Study of processes with a pair of top-antitop quarks and missing transverse energy in the final state in proton-proton collisions with the CMS detector at the Run 2 of the LHC

TESIS DOCTORAL

Dr. Javier Fernández Menéndez

Dr. José Enrique Palencia Cortezón

Universidad de Oviedo
Universidá d'Uviéu
University of Oviedo

RESUMEN DEL CONTENIDO DE TESIS DOCTORAL

1.- Título de la Tesis	
Español: Estudio de procesos con presencia de pares de quarks top-antitop y energía transversa faltante en colisiones protón-protón con el experimento CMS en el Run 2 del LHC.	Inglés: Study of processes with a pair of top-antitop quarks and missing transverse energy in the final state in proton-proton collisions with the CMS detector at the Run 2 of the LHC.

2.- Autor	
Nombre: Juan Rodrigo González Fernández	DNI:
Programa de Doctorado: Materiales	
Órgano responsable: Comisión Académica Programa de Doctorado en Materiales	

RESUMEN (en español)

En esta tesis se presentan medidas de la sección eficaz de producción de pares de quarks top-antitop ($t\bar{t}$) con diferentes condiciones de funcionamiento del acelerador y una búsqueda de nueva física en el marco de las teorías de supersimetría. Para ello, se han usado datos de colisiones protón-protón en el Gran Colisionador de Hadrones (LHC) del CERN, obtenidos con el detector CMS. Además, se presenta un estudio sobre los efectos de la radiación en la eficiencia de las cámaras de deriva (DT) de CMS.

Las DT se utilizan para identificar muones en la parte central de CMS con alta eficiencia. En 2026, el LHC se modificará para aumentar su luminosidad, incrementando notablemente la cantidad de radiación a la que serán sometidos los subdetectores de CMS. En este estudio se caracteriza la pérdida de eficiencia de las cámaras de deriva debido a los efectos de la radiación. Se observa una pérdida de eficiencia en cada cámara de hasta el 38%, pero la eficiencia de reconstrucción de muones se mantiene cerca del 100 % incluso al final de la toma de datos.

Además, la sección eficaz de producción de $t\bar{t}$ se ha medido usando los datos tomados en 2015 y 2016 a diferentes energías en el centro de masas. A $\sqrt{s}$ = 13 TeV, varias medidas se realizaron usando diferentes conjuntos de datos. Los resultados coinciden con las predicciones del Modelo Estándar. También se presenta la primera y única medida de la sección eficaz de $t\bar{t}$ a $\sqrt{s}$ = 5.02 TeV.

Por último, se expone una búsqueda de quarks stop. La producción de estas partículas con una masa cercana a la del quark top no puede ser probada en búsquedas genéricas de quarks stop debido a la gran cantidad de fondo de sucesos $t\bar{t}$. Esta búsqueda se realiza a partir de la medida de precisión de la sección eficaz de $t\bar{t}$ complementada con el estudio de un observable discriminante. No se observa ningún exceso y se establecen límites de exclusión para stops con una masa de hasta 208 GeV.

RESUMEN (en Inglés)

This thesis presents measurements of the top-antitop quark pair ($t\bar{t}$) production cross section and a search for new physics in the context of supersymmetry using data from proton-proton collisions at the CERN Large Hadron Collider (LHC), recorded by the CMS detector. Furthermore, a study of the effects of the radiation on the performance of the drift tubes (DT) chamber of the CMS detector is presented.

The main goal of the DT chambers is identifying muons going through CMS with a high efficiency. In 2026 the LHC will be upgraded to run at high luminosity conditions. The CMS detectors will have to deal with extreme radiation conditions. The studies presented in this thesis characterize the efficiency loss under high radiation conditions during a long period of time. The

hit efficiency is shown to decrease, but the global CMS muon reconstruction efficiency is shown to stay close to 100 %, even at the end of the data taking.

Besides, the $t\bar{t}$ production cross section is measured using data taken during 2015 and 2016 with different conditions of the LHC. The measurements are performed using different datasets at $\sqrt{s}$ = 13 TeV. The results are in agreement with the Standard Model predictions. The high precision of these measurements, with lower uncertainties than the best predictions, allows to test different aspects of the theory. The first and only measurement of the $t\bar{t}$ cross section at $\sqrt{s}$ = 5.02 TeV is also presented.

Finally, a search for the production of stop quarks is reported. The production of these particles with a mass close to that of the top quark cannot be probed by generic stop quark searches. The sensitivity to this process comes from a very precise estimate of the SM $t\bar{t}$ production and the use of a discriminant observable. No excess is found over the background prediction and exclusion limits are set up to a stop quark mass of 208 GeV.

SR. PRESIDENTE DE LA COMISIÓN ACADÉMICA DEL PROGRAMA DE DOCTORADO EN MATERIALES

Agradecimientos

Hace 9 años empecé el grado en Física en la Universidad de Oviedo. Ese curso conocí a Javi, al que admiré desde el primer momento, aunque entonces no me hubiera imaginado que acabaría siendo mi director de tesis. En el segundo semestre conocí a Chiqui, quien desde el primer minuto me metió el gusto por programar, y a Javier, que fue el primero en hablarnos de física más reciente que la de hace 150 años y que ha resultado ser el jefe que todo el mundo querría tener. Ahora, no puedo menos que agradeceros por haber sido los mejores mentores que se pueden tener. Gracias.

Más adelante, Kike me enseñaría a evitar lo innecesario y hacer lo necesario lo mejor posible, a basarme en lo que sé y no en lo que supongo o asumo, a ir a lo práctico antes que a lo ideal, a documentar lo que hago hoy, porque mañana ya no lo recordaría. Por todo ello, muchas gracias. También a Santi y Bárbara por vuestro apoyo y consejo durante estos años.

Gracias a mis compañeros y amigos: Nacho, Sergio, Pietro, Carlos, Víctor, Clara. Pedro, Nicoló y Cedric del IFCA. Miguel, Brais, Miriam y María de Santiago. Sergio y David (CIEMAT), Alex (IFIC), entre otros. A mis amigos: David, Dani y Nacho, Raúl y Vic, Fran, Patri, Hugo y muchos otros. A mis compañeros de Cielos Despejados. A mis mentores del IFCA y del CIEMAT: Parbol, Cristina, MaryCruz, Ignacio. Especiales gracias a mis padres y a mis hermanos, particularmente a Gabi, quien ha influenciado mi camino hasta aquí y con quien comparto la pasión por la ciencia.

I would like to express my sincere gratitude to P. Silva, A. Giammanco, M. Aldaya, M. Peruzzi, Jonatan, Luca, Rebeca, G. Krintiras, F. Cavallo, C. Battilana, Atiqah, for your contributions to the research presented in this thesis.

Por último, gracias a mi compañera de vida, Laura, por tu cercanía durante estos años.

Contents

List of Figures

List of Tables

A Laura

Chapter 1

Introduction

The Standard Model (SM) of particle physics is a theory that has shown to accurately describe all the subatomic phenomena ever observed and describes the behaviour of the elementary particles and their interactions through electromagnetic, weak, and strong forces. It was formulated during the 1970s, succesfully predicting the existence of the W and Z bosons, the top quark and the Higgs boson and their properties. The SM is a quantum field theory that classifies the elementary particles into fermions, with a half-integer spin value, and bosons, with integer spin. An introduction to the fundamental pieces of the SM is given in Chapter 2.

To study the most fundamental properties of matter, large particle accelerators are used to accelerate the colliding particles at a velocity close to the speed of light. The European Organization for Nuclear Research (CERN, from the French name: *Centre européenne pour la recherche nucléaire*) has played a major role in the discoveries that validated the SM during the last 50 years. The Large Hadron Collider (LHC) at CERN is the largest particle accelerator ever built. Proton-proton (pp) collisions are accelerated at the energy frontier and collide at the centre of large detectors, used to detect the new particles that emerge from the collisions.

The Compact Muon Solenoid (CMS) [1] is one of the four large experiments located at the LHC tunnel. It is a general-purpose detector that allows us to measure the fundamental parameters of the SM, such as the mass of the Higgs boson or the properties of the top quark. The results presented in this thesis are based on data collected by the CMS detector during 2015 and 2016. A more detailed description of the detector and the experimental methods used to reconstruct the particles coming from the pp collisions can be found in Chapter 3.

The CMS detector is composed of various subdetectors, designed to measure different particles and their properties. The drift tubes (DT) system is one of the subdetectors, used to measure the trajectories of muons produced in the collisions, allowing to efficienctly identify muons and trigger the data taking. During all data-taking periods, the CMS drift tubes have been reconstructing muons with an efficiency close to 99%. The performance of this subdetector has been stable during almost 10 years of data taking, allowing to achieve several milestones, as the discovery of the Higgs boson. To continue exploring the energy frontiers of particle physics, a major upgrade of the LHC and the CMS detector is planned [2]. During the operation of the upgraded machine, the LHC at high luminosity (HL-LHC), the DT chambers will receive a huge amount of radiation that will affect their performance. In this thesis, a study of the effect of the radiation on the expected performance of the CMS DT system during the HL-LHC is presented in Chapter 4.

The top quark is the heaviest known particle. Thanks to its unique properties, this particle is key to understand some of the most fundamental aspects of the SM, including the mass of the Higgs boson and other particles, and the nature of quantum chromodynamics (QCD). The LHC is a top quark factory: the production rate of processes containing top quarks is larger than in any other particle accelerator. In pp collisions at the LHC centre-of-mass energies ($\sqrt{s}$), top quarks are mainly produced in pairs ($t\bar{t}$) through the gluon-gluon fusion process. In Chapter 5, a measurement of the $t\bar{t}$ production cross section is presented. A precise measurement of the $t\bar{t}$ cross section was performed using the datasets taken during 2011 and 2012 at 7 and 8 TeV, using an event-couting approach. The first pp collisions at $\sqrt{s} = 13$ TeV were produced in 2015 and a first $t\bar{t}$ cross section measurement was performed at this previously unexplored centre-of-mass energy using a small amount of data. Afterwards, this measurement was improved using the full 2015 dataset. With the 2016 dataset, an order of magnitude larger than the previous one, the $t\bar{t}$ inclusive cross section was measured again. Furthermore, the $t\bar{t}$ cross section was measured at $\sqrt{s} = 5.02$ TeV for the first time, using a small dataset collected during 2015. These measurements are documented in references [3–6].

A third topic of this thesis is the search for supersymmetric particles. All the $t\bar{t}$ cross section measurements previously mentioned are in agreement with the SM predictions and after the discovery of the Higgs boson in 2012 [7, 8], the particle puzzle of the SM seemed to be complete. However, there are several challenges in nature that may not fit into the SM picture of the particle physics world, such as the asymmetry between matter and antimatter in the universe or the existence of dark matter and dark energy. Some of these questions are covered by one of the most popular theories of particle physics beyond the SM: supersymmetry (SUSY) [9–15]. This theory predicts the existence of a new particle for each of the known SM particles, introducing a new symmetry between fermions and bosons. In this thesis, a search for the SUSY partner of the top quark is presented in Chapter 6. In this search, the existence of a scalar particle with a mass close to the top quark mass is probed, whose production is degenerate with the SM $\mathrm{t\bar{t}}$ process. A SUSY particle with these characteristics is favoured by naturalness in many SUSY scenarios and previous searches have a limited sensitivity to the production of such particles. This search is based on the precise measurement of the $\mathrm{t\bar{t}}$ production cross section, described in this thesis, and tries to detect the presence of the signal as an excess above the SM expectation. The sensitivity of the analysis is increased by considering the distribution of a discriminant observable. This search is documented in reference [16].

Finally, the conclusions about this work are presented in Chapter 7.

Chapter 2

Theoretical framework

2.1 The SM of particle physics

Particle physics is the science that studies the smallest constituents of matter and radiation. Its goal is to understand the nature of the elementary parts that conform our universe and the forces that govern their interactions: electromagnetic force, weak force, strong force and gravity.

According to our current understanding, the elementary particles are explained as excitations of quantum fields that live as a part of the structure of the universe. The mathematical framework that supports the description of these fields is called quantum field theory (QFT). This framework includes the postulates of quantum mechanics but also includes the ones from special relativity.

In QFT, the particle models are described in terms of a Lagrangian that involves the particle content of the model and the interactions between them. Any QFT model that intends to become a candidate theory to explains the nature of our universe must be capable of making quantitative predictions about the real world. In order to satisfy this condition, quantum theories must be renormalizable [17]. The particle interactions in QFT are described using Feynman diagrams. For a theory with a small coupling constant, the interaction probabilities can be calculated using perturbation theory up to an arbitrary order. A deeper introduction to QFT can be found in reference [18].

The SM of particle physics is a QFT that has been shown to accurately describe most of the particle physics phenomena ever observed. The SM describes three of the four fundamental forces of nature (electromagnetic, weak and strong, excluding gravity) and classifies all the elementary particles, conforming a complete scheme with all the known particles.

The constituents of matter have a spin of 1/2 and are called fermions. They are subdivided into quarks and leptons, forming 3 families. The quarks are colour-charged and are combined together to form hadrons. They can have an electric charge of +2/3, quarks up, charm and top (u, c, t) or -1/3, quarks down, strange and bottom (d, s, b). There are three charged leptons, electron, muon and tau (e, μ, τ) and three neutral leptons, called neutrinos (ν_e, ν_μ, ν_τ). Each of the SM particles has a corresponding antiparticle: a clone particle with the same mass but opposite charges.

On the other hand, the particles that are responsible of the interactions have an integer value of the spin (0, 1) and are called bosons. The gauge bosons (or vector bosons) have a spin 1. The photon (γ) is responsible of the electromagnetic force. It is a massless particle, giving rise to the infinite range of the electromagnetic force. Three massive vector bosons, $W^{\pm}$ and Z, are the carriers of the weak force. Finally, eight double-coloured massless gluons (g) are responsible of the strong force. The Higgs boson is the only scalar boson of the theory (spin = 0) and explains how the SM particles acquire mass. A schematic overview of the SM particles is shown in figure 2.1.

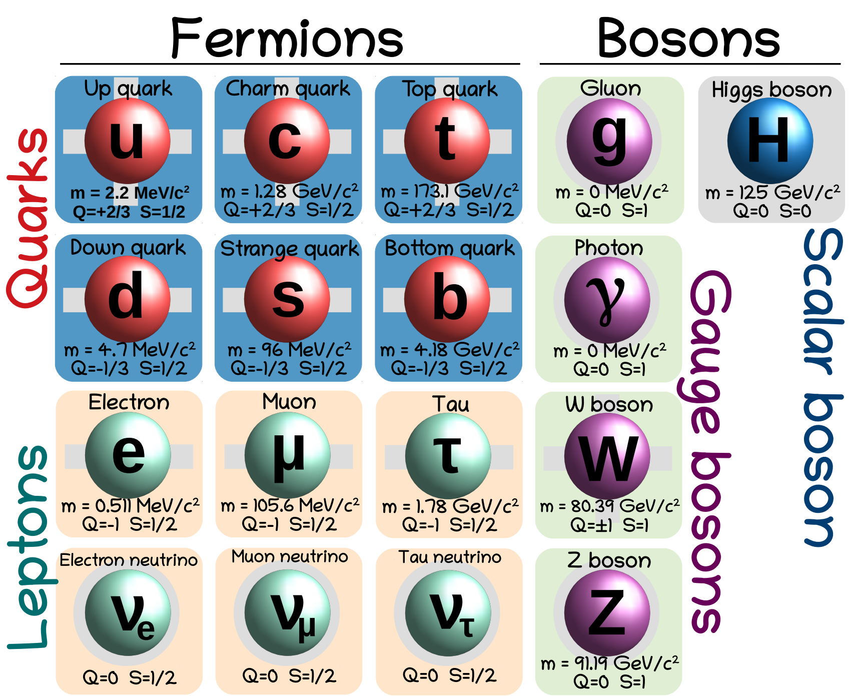

FIGURE 2.1: Schematic table of the SM particles.

The SM has been tested in many different experiments for more than 50 years, showing an excellent agreement with all the observations. In the following subsections, an overview of the theoretical features of the SM is presented. Several observables can be derived using this theoretical formulation, such as decay widths (Γ) and cross sections (σ). These quantities are usually obtained using the Feynman rules to obtain probability amplitudes ($\mathcal{M}$) and Fermi's Golden Rule. More details on how these observables are calculated can be found in reference [19].

The study of the SM is divided into two sectors: the electroweak theory, that is in charge of studying the electroweak interactions, produced by the W and Z bosons, and photons, and QCD, the theory that explains the strong interactions. The most important aspects of the electroweak theory, including the electroweak symmetry breaking, are summarised in section 2.1.1. A summary of the most important aspects of QCD is presented in section 2.1.2.

The Higgs mechanism is crucial to understand why the SM particles get a mass. Moreover, a particle compatible with the SM Higgs boson, a scalar particle predicted by the Higgs mechanism that explains the electroweak symmetry breaking, was recently discovered by the CMS and ATLAS collaborations [7, 8]. An overview of this mechanism is shown in section 2.1.3.

Finally, an introduction to the most fundamental aspects of scattering theory in hadron colliders is given in section 2.2.

2.1.1 Electroweak sector

The SM electroweak sector, explained by the model of Glashow, Salam and Weinberg [20], unifies the electromagnetic and weak interactions under the gauge group $SU(2)_L \times U(1)_Y$, where L corresponds to the weak isospin and Y is the weak hypercharge.

To study the weak interactions, matter fields are decomposed into left- and right-handed fermions:

$$\psi = \psi_L + \psi_R. \tag{2.1}$$

Massless fermions are described by the Dirac lagrangian, $\mathcal{L}_{\text{Dirac}}$, which can be decomposed into left and right terms:

$$\mathcal{L}_{\text{Dirac}} = \bar{\psi}\gamma^\mu\partial_\mu\psi = \bar{\psi}_L\gamma^\mu\partial_\mu\psi_L + \bar{\psi}_R\gamma^\mu\partial_\mu\psi_R. \tag{2.2}$$

The chiral structure of weak interactions is reproduced by left-handed fermions in weak-isospin doublets and right-handed fermions in weak-isospin singlets:

$$Q_i = \begin{pmatrix} q_i^u \\ q_i^d \end{pmatrix}_{\mathrm{L}}, \qquad u_{\mathrm{R}}^i, \qquad \mathrm{d}_{\mathrm{R}}^i, \qquad L_i = \begin{pmatrix} \nu_{\ell_i} \\ \ell_i \end{pmatrix}_{\mathrm{L}}, \qquad \ell_{\mathrm{R}}^i, \tag{2.3}$$

where i goes through the number of generations, from 1 to 3, so $q^u = (\mathrm{u}, \mathrm{c}, \mathrm{t})$, $q^d = (\mathrm{d}, \mathrm{s}, \mathrm{b})$ for the left-handed weak-isospin doublets of quarks, $u_{\mathrm{R}} = (\mathrm{u_R}, \mathrm{c_R}, \mathrm{t_R})$ and $d_{\mathrm{R}} = (\mathrm{d_R}, \mathrm{s_R}, \mathrm{b_R})$ for the right-handed weak-isospin singlets of quarks, $\ell = (e, \mu, \tau)$ for the left-handed weak-isospin doublets containing a neutrino and a charged lepton, and $\ell_{\mathrm{R}} = (e_{\mathrm{R}}, \mu_{\mathrm{R}}, \tau_{\mathrm{R}})$ for the right-handed weak-isospin singlets of charged leptons.

The value of the third component of the weak isospin, I_3, is 1/2 for the upper components of the weak-isospin doublets and -1/2 for the lower component. It is 0 for the singlets, that do not undergo weak interactions. The third component is related to the $\mathrm{U}(1)_{\mathrm{Y}}$ hypercharge, Y, and the electric charge, $\hat{\mathrm{Q}}$, as

$$\mathrm{Y} = \hat{\mathrm{Q}} - I_3. \tag{2.4}$$

The values of these hypercharges are

$$\mathrm{Y}_{L_i} = -1/2, \qquad \mathrm{Y}_{e_{\mathrm{R}}} = -1, \qquad \mathrm{Y}_{Q_i} = 1/6, \qquad \mathrm{Y}_{u_{\mathrm{R}}} = 2/3, \qquad \mathrm{Y}_{d_R} = -1/3.$$

The $\mathrm{SU}(2)_L$ symmetry gives rise to three electroweak bosons, $W_\mu^{1,2,3}$, that are spin-1 fields. The group generators are denoted as T^i ($i = 1, 2, 3$) and are defined in terms of the Pauli matrices, ς_i, as $T^i = \frac{1}{2}\varsigma_i$. The Pauli matrices are unitary and hermitian 2×2 matrices that form a basis of the vector space for $\mathrm{SU}(2)_L$, and are defined as

$$\varsigma_x = \begin{pmatrix} 0 & 1 \\ 1 & 0 \end{pmatrix}, \qquad \varsigma_y = \begin{pmatrix} 0 & -i \\ i & 0 \end{pmatrix}, \qquad \varsigma_z = \begin{pmatrix} 1 & 0 \\ 0 & -1 \end{pmatrix}.$$

The Pauli matrices satisfy the commutation relations

$$\left[\varsigma_i, \varsigma_j\right] = 2i\epsilon^{ijk}\varsigma_k, \tag{2.5}$$

where ϵ^{ijk} is the antisymmetric tensor. On the other hand, the $\mathrm{U}(1)_{\mathrm{Y}}$ symmetry gives rise to a unique boson field B_μ. The gauge invariant field strength tensors can be defined as

$$W^i_{\mu\nu} = \partial_\mu W^i_\nu + \partial_\nu W^i_\mu + g\epsilon^{ijk} W^j_\mu W^k_\nu \qquad \text{and}$$
$$B_{\mu\nu} = \partial_\mu B_\nu - \partial_\nu B_\mu, \tag{2.6}$$

where g and g' denote the $\mathrm{SU}(2)_L$ and $\mathrm{U}(1)_Y$ coupling constants, respectively. The coupling of matter fields to fermions is done by replacing the derivative ∂_μ by the electroweak covariant derivative

$$D_\mu = \partial_\mu + igT^i W^i_\mu + ig'\frac{Y}{2}B_\mu, \tag{2.7}$$

that, when applied to fermions, leads to matter-gauge couplings of the form $g\bar{\psi}W_\mu\gamma^\mu\psi$.

At this point, both fermionic and electroweak fields are massless. In fact, any mass term of the form $m\bar{\psi}\psi$ in the SM lagrangian would violate the $\mathrm{SU}(2)_L$ invariance. This problem is solved thanks to the Higgs mechanism. The Higgs boson is the only scalar boson in the electroweak theory. Its existence is derived, along with the masses of the gauge electroweak bosons, from the electroweak spontaneous symmetry breaking explained in section 2.1.3.

2.1.2 Quantum chromodynamics

In the SM, the strong sector is studied by QCD. In QCD, quark fields are charged under $\mathrm{SU}(3)_C$, i.e. each quark appears as a triplet of 3 colours, whereas the leptons are singlets. There are eight strong gauge fields, corresponding to gluons named G^A_μ, where the index A goes from 1 to 8, and can be expressed in terms of the 3×3 Gell-Mann matrices, T^A_s, that satisfy the relations

$$[T^A_s, T^B_s] = if^{ABC}T^C_s, \tag{2.8}$$

where f^{ABS} are the $\mathrm{SU}(3)_C$ structure constants. The QCD gauge invariant field strength tensors can be defined as

$$G^A_{\mu\nu} = \partial_\mu G^A_\nu + \partial_\nu G^A_\mu + g_s f^{ABC} G^B_\mu G^C_\nu, \tag{2.9}$$

where g_s is the $\mathrm{SU}(3)_C$ coupling constant. A term of the form $ig_s T^A G^A_\mu$ is added to the definition of the covariant derivative is defined in equation (2.7) to include the QCD sector.

The main particularity of QCD with respect to the electroweak sector of the SM is the value of $g_s \sim 1$ and its running with the centre-of-mass energy in QCD interactions.

This has some physical implications on the QCD phenomenology. First, the order-by-order calculation using perturbation theory is not possible at low energies, where the coupling constant is close to 1 and thus higher orders are not negligible in the calculation, which occurs up to a energy scale called Λ_{QCD}. Perturbative QCD (pQCD) is the regime of energies where perturbative calculations can be used to predict QCD observables, corresponding to $Q^2 > \Lambda^2_{\text{QCD}}$, where Q^2 is the squared transferred energy in a QCD interaction. The strong coupling constant $\alpha_S = \frac{g_s^2}{4\pi}$ is more often used in this thesis than g_s^2. Its value runs with Q^2 as

$$\alpha_S(Q^2) \sim \frac{1}{\ln(Q^2/\Lambda^2_{\text{QCD}})}. \tag{2.10}$$

In the framework of pQCD, predictions are expressed in terms of the strong coupling constant, $\alpha_S(\mu_{\text{R}})$, where μ_{R} is the renormalisation scale.

The so-called asymptotic freedom of quarks and gluons is directly derived from equation (2.10). This property refers to the trend of quarks and gluons to behave as free particles at high energies. Furthermore, quarks and gluons are confined, which means that they cannot be observed in freedom, but they bound together to form colour-neutral particles called hadrons. This can be understood from the fact that α_S increases with the distance, so it would always be energetically preferable to create new colour charges from the vacuum to obtain colour-neutral states. These states are mainly observed in groups of three quarks (baryons) or as quark-antiquark pairs (mesons).

As a consequence of these properties, quarks and gluons produced in high-energy collisions create colourless states in a timescale of $\sim 1/\Lambda_{\text{QCD}}$ in a process called hadronization. The result is a collection of hadrons called jet which can be experimentally observed. A more complete description of this process and the most relevant aspects of its modelling are shown in section 2.2.2.

2.1.3 The Higgs mechanism

The Higgs mechanism is applied to the SM to break the $\text{SU}(2)_L \times \text{U}(1)_\text{Y}$ symmetry into $\text{U}(1)_\text{Y}$ with a massless vector boson (the photon) and $\text{SU}(2)_L$ with the W and Z bosons. As an example of how this mechanism works, let us take a scalar field ϕ and consider the next lagrangian

$$\mathcal{L} = \frac{1}{2}\partial_\mu\phi\partial^\mu\phi - V(\phi) \text{ where } V(\phi) = \frac{1}{2}\xi^2\phi^2 + \frac{1}{4}\lambda\phi^4. \tag{2.11}$$

This lagrangian is symmetric under reflections $\phi \to -\phi$. The minimum of the potential for the field ϕ, corresponding to the vacuum expectation value $\langle 0|\phi|0\rangle$ is 0 if $\xi^2 > 0$ (λ must be positive so the potential has a finite minimum value), and the lagrangian represents a scalar particle with mass ξ. But in the case of $\xi^2 < 0$, the potential has the form shown in figure 2.2 and has two minima, given by the following expresion

$$\langle 0|\phi|0\rangle = \phi_0 = \pm v = \pm\sqrt{-\frac{\xi^2}{\lambda}}. \tag{2.12}$$

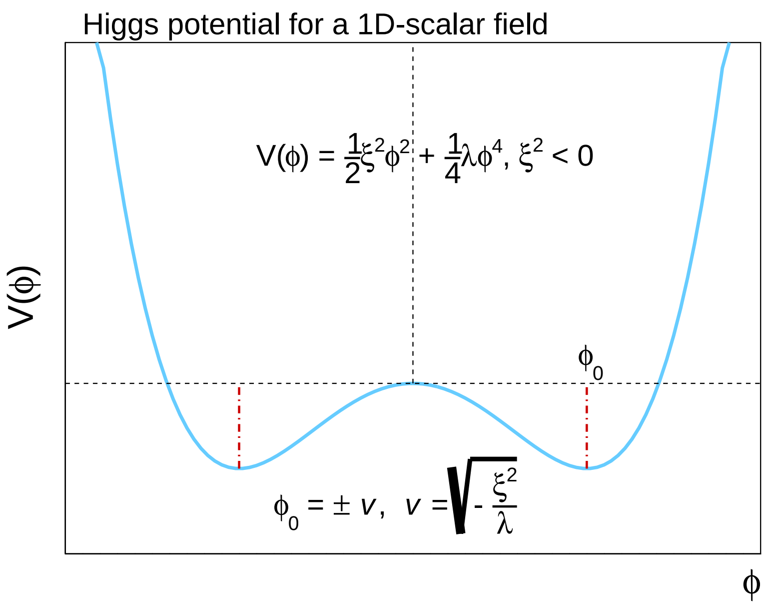

FIGURE 2.2: Higgs potential for a 1D scalar boson

To extract the interactions of the theory, we can expand the lagrangian around the minimum v, defining $\phi = v + \epsilon$, where ϵ is an infinitesimal, as

$$\mathcal{L} = \frac{1}{2}\partial_\mu\epsilon\partial^\mu\epsilon + \xi^2\sigma^2 - \sqrt{-\xi^2\lambda}\epsilon^3 - \frac{1}{4}\lambda^4. \tag{2.13}$$

This lagrangian now contains a term with ϵ^3 which is not anymore symmetric under reflections. We say that the symmetry was spontaneously broken.

In the SM, we consider a $\mathrm{SU}(2)_L$ doublet of scalar fields

$$\phi = \begin{pmatrix} \phi^+ \\ \phi^0 \end{pmatrix}, \tag{2.14}$$

where ϕ^+ is a positively-charged scalar field and ϕ^0 is a neutral scalar field. We consider a lagrangian

$$\mathcal{L} = (D_\mu \phi)^\dagger (D^\mu \phi) - V(\phi) \text{ where } V(\phi) = \xi^2 \phi^\dagger \phi + \lambda (\phi^\dagger \phi)^2. \tag{2.15}$$

Substituting the covariant derivatives with the definition in equation (2.7), we would obtain

$$(D_\mu \phi)^\dagger (D^\mu \phi) = \left| \partial_\mu + ig\frac{T^i}{2} W^i_\mu + ig'\frac{Y}{2} B_\mu \right|^2. \tag{2.16}$$

Now, for a gauge field, the lagrangian must be invariant under a transformation $\phi(x) \to e^{-i\theta(x)/v}\phi(x)$. Following the same procedure as for the 1D-scalar case, we can obtaining also a minima for the potential, at v, and we can expand around the minima using a field ϕ as

$$\phi = \frac{1}{\sqrt{2}} e^{i\theta^i(x)T^i/v} \begin{pmatrix} 0 \\ v+h \end{pmatrix}. \tag{2.17}$$

Substituting in equation (2.16), we obtain

$$(D_\mu \phi)^\dagger (D^\mu \phi) = \left| \begin{pmatrix} \partial_\mu + \frac{i}{2}\left(gW^3_\mu + g'\frac{Y}{2}B_\mu\right) & i\frac{g}{2}\left(W^1_\mu - iW^2_\mu\right) \\ i\frac{g}{2}\left(W^1_\mu + iW^2_\mu\right) & \partial_\mu - \frac{i}{2}\left(gW^3_\mu - g'\frac{Y}{2}B_\mu\right) \end{pmatrix} \begin{pmatrix} 0 \\ v+h \end{pmatrix} \right|^2. \tag{2.18}$$

If we expand, we find

$$(D_\mu \phi)^\dagger (D^\mu \phi) \ni \frac{1}{2}(\partial_\mu h)^2 + \frac{1}{8}(v+h)^2 |W^1_\mu + iW^2_\mu|^2 + \frac{1}{8}(v+h)^2 |gW^3_\mu - g' B_\mu|^2. \tag{2.19}$$

The full calculation includes all the interaction terms. We find terms mixing the fields corresponding to the electroweak bosons. We can apply a rotation of the form

$$\begin{pmatrix} Z_\mu \\ A_\mu \end{pmatrix} = \begin{pmatrix} \cos\theta_W & -\sin\theta_W \\ \sin\theta_W & \cos\theta_W \end{pmatrix} \begin{pmatrix} W^3_\mu \\ B_\mu \end{pmatrix}, \tag{2.20}$$

where θ_W is the Weinberg angle. With $W^\pm = (W^1 \mp W^2)/\sqrt{2}$ and $\tan\theta_W = g'/g$, we obtain

$$\mathcal{L} \ni \frac{1}{2}(\partial_\mu h)^2 + \frac{g^2 v^2}{4} W^+_\mu W^{-\mu} + \frac{g^2 v^2}{8\cos^2\theta_W} Z_\mu Z^\mu + A_\mu A^\mu. \tag{2.21}$$

Now, the W^+_μ, W^-_μ and Z_μ fields have acquired mass and correspond to the $W^\pm$ and Z electroweak bosons, while the field A_μ, corresponding to the $U(1)_Y$ boson, the photon, is massless. The masses of the bosons are

$$m_W = \frac{1}{2} g v \quad \text{and} \quad m_Z = \frac{1}{2} \frac{g v}{\cos \theta_W}. \tag{2.22}$$

The Fermi constant G_F can be defined from g and m_W as

$$G_F = \frac{\sqrt{2} g^2}{8 m_W^2}. \tag{2.23}$$

Up to now, we have expanded the term with the covariant derivatives, $(D_\mu \phi)^\dagger (D^\mu \phi)$, around the vacuum state. If we expand the other term in (2.15), the Higgs potential $V(\phi)$, we get a scalar particle with a mass

$$m_H = \sqrt{2} \mu = \sqrt{2 \lambda} v, \tag{2.24}$$

corresponding to the Higgs boson mass.

2.1.4 Yukawa interactions

The Higgs mechanism can also explain the masses of the fermions in the SM. In this case, we have to relate the masses of the left-handed weak-isospin doublets with the right-handed singlets. As an example, let us see the term corresponding to a lepton ℓ, where ψ_L is a weak-isospin doublet for ℓ and ℓ_R corresponds to the right-handed singlet. Then, the Yukawa interaction is of the form

$$\mathcal{L}_{\text{Yukawa}} \ni -y_\ell \psi_L \phi \ell_R + h.c., \tag{2.25}$$

where ϕ is the scalar field (the Higgs boson field) and y_ℓ is the Yukawa coupling of the lepton ℓ. The term $+h.c.$ indicates that the hermitic conjugate term must be added.

We can expand again around the Higgs vacuum state defined in (2.17). A term mass term for the fermions of the form

$$-\frac{y_\ell v}{\sqrt{2}} \bar{\ell} \ell \text{ (+ interaction terms)}$$

is obtained. The mass of the fermions are now given in terms of the Yukawa coupling and the value of the Higgs vacuum state.

2.1.5 The Cabibbo-Kobayashi-Maskawa matrix

In the previous sections, we have assumed that no mixing terms between generations exist. However, this does not occur for quarks. In this case, the Yukawa couplings must be 3×3 matrices that can contain non-diagonal terms. The mass eigenstates are now rotated with respect to the weak (or flavour) eigenstates. The unitary matrix that parametrises this rotation is the Cabibbo-Kobayashi-Maskawa (CKM) matrix, V_{CKM}. For the down-type quarks, let us define the mass eigenstates as $\begin{pmatrix} \mathrm{d}' & \mathrm{s}' & \mathrm{b}' \end{pmatrix}$ and the flavour eigenstates as $\begin{pmatrix} \mathrm{d} & \mathrm{s} & \mathrm{b} \end{pmatrix}$, related as

$$\begin{pmatrix} \mathrm{d}' & \mathrm{s}' & \mathrm{b}' \end{pmatrix} = V_{\mathrm{CKM}} \begin{pmatrix} \mathrm{d} & \mathrm{s} & \mathrm{b} \end{pmatrix}, \text{where } V_{\mathrm{CKM}} = \begin{pmatrix} V_{\mathrm{ud}} & V_{\mathrm{cd}} & V_{\mathrm{td}} \\ V_{\mathrm{us}} & V_{\mathrm{cs}} & V_{\mathrm{ts}} \\ V_{\mathrm{ub}} & V_{\mathrm{cb}} & V_{\mathrm{tb}} \end{pmatrix}. \tag{2.26}$$

The off-diagonal terms allow weak-interaction transitions between different quark generations. A standard parametrization of the CKM matrix uses three mixing angles, θ_{12}, θ_{23} and θ_{13} and a charge-parity (CP) violating phase δ_{13}, so that the matrix is written as

$$V_{\mathrm{CKM}} = \begin{pmatrix} \cos\theta_{12}\cos\theta_{13} & \sin\theta_{12}\cos\theta_{13} & \sin\theta_{13}e^{-i\delta_{13}} \\ -\sin\theta_{12}\cos\theta_{23} - \cos\theta_{12}\sin\theta_{23}\sin\theta_{13}e^{i\delta_{13}} & \cos\theta_{12}\cos\theta_{23} - \sin\theta_{12}\sin\theta_{23}\sin\theta_{13}e^{i\delta_{13}} & \sin\theta_{23}\cos\theta_{13} \\ \sin\theta_{12}\sin\theta_{23} - \cos\theta_{12}\cos\theta_{23}\sin\theta_{13}e^{i\delta_{13}} & -\cos\theta_{12}\sin\theta_{23} - \sin\theta_{12}\cos\theta_{23}\sin\theta_{13}e^{i\delta_{13}} & \cos\theta_{23}\cos\theta_{13} \end{pmatrix} \tag{2.27}$$

The currently best known values for the mixing angles and CP-violating phase are shown in table 2.1.

2.1.6 Summary of the SM parameters

Collecting all the theory ingredients presented in this section, we can construct the different parts of the SM lagrangian. First, the kinematic terms for the gauge bosons are constructed from the electroweak and QCD strength tensors in equations (2.6) and (2.9) as

$$\mathcal{L}_{\mathrm{gauge}} = -\frac{1}{4}G^{A}_{\mu\nu}G^{A,\mu\nu} - \frac{1}{4}W^{i}_{\mu\nu}W^{i,\mu\nu} - \frac{1}{4}B_{\mu\nu}B^{\mu\nu}. \tag{2.28}$$

For describing the interaction of the gauge bosons with fermions, we can first add the strong term to the definition of the electroweak covariant derivative defined in (2.29), obtaining

$$D_{\mu} = \partial_{\mu} + ig_{s}T^{A}G^{A}_{\mu} + igT^{i}W^{i}_{\mu} + ig'\frac{Y}{2}B_{\mu}. \tag{2.29}$$

With the definition of fermions in equation (2.3), we can form the lagrangian term to describe gauge the interactions of the fermions as

$$\mathcal{L}_{\text{fermion}} = i\bar{L}_i D_\mu \gamma^\mu L_i + i\bar{\ell}_{R,i} D_\mu \gamma^\mu \ell_{R,i} + i\bar{Q}_i D_\mu \gamma^\mu Q_i + i\bar{u}_{R,i} D_\mu \gamma^\mu u_{R,i} + i\bar{d}_{R,i} D_\mu \gamma^\mu d_{R,i}. \tag{2.30}$$

By completing equation (2.25) and using the fermion definitions in (2.3), we can obtain the complete Yukawa lagrangian as

$$\mathcal{L}_{\text{Yukawa}} = -y_\ell \bar{L}_i \phi \ell_{\text{R,i}} - y_d \bar{Q}_i \phi d_{R,i} - y_u \bar{Q} \phi u_{R,i} + h.c. \tag{2.31}$$

The Higgs boson lagrangian can be obtained from equation (2.15) as

$$\mathcal{L}_{\text{Higgs}} = (D_\mu \phi)^\dagger (D^\mu \phi) - \mu^2 \phi^\dagger \phi + \lambda (\phi^\dagger \phi)^2. \tag{2.32}$$

Finally, we obtain the full lagrangian of the SM as the sum of the previous lagrangians

$$\mathcal{L}_{\text{SM}} = \mathcal{L}_{\text{gauge}} + \mathcal{L}_{\text{fermion}} + \mathcal{L}_{\text{Yukawa}} + \mathcal{L}_{\text{Higgs}}. \tag{2.33}$$

The SM has 18 free parameters (considering massless neutrinos, as they have been presented in this section): the 9 Yukawa couplings to the fermions, the 3 coupling constants, the mass of the Higgs boson and its expected vacuum value (2), and the CKM mixing angles and CP violating phase (4).

A summary of the free parameters of the SM is presented in table 2.1. In this table the masses of the fermions are given, which are related to the Yukawa couplings as $m_i = y_i v/2$. The strong coupling constant is given for $\mu_{\text{R}} = m_{\text{Z}}$. Due to the relations between several electroweak fundamental parameters, such as the Weinberg angle θ_{W}, the coupling constants g and g' or the masses of the electroweak bosons m_{W} and m_{Z}, only two of them are needed to obtain the rest. The fine-structure constant $\alpha_{\text{EM}} = g'(\mu_{\text{R}} = 0)^2/(4\pi)$ is given and the m_{W} are given.

2.2 Hadron collider physics

In pp collisions, a hard process (or hard scattering) is known as the interaction process between the constituents of the proton (generically called partons). The production cross section of SM processes in pp collisions that are produced in a hard scattering depend on the momentum distribution of the partons. The fundamental aspects of the phenomenology of the hard scattering is discussed in section 2.2.1.

Parameter	value	Parameter	value
α_{EM}	$1/137.035999074 \pm 4 \cdot 10^{-10}$	m_e	$0.510998946 \pm 3 \cdot 10^{-9}$ MeV
$\alpha_{\mathrm{S}}(\mu_{\mathrm{R}} = m_{\mathrm{Z}})$	0.1185 ± 0.0001	m_μ	$105.658375 \pm 2 \cdot 10^{-6}$ MeV
m_{W}	80.385 ± 0.0001 GeV	m_τ	1776.8 ± 0.1 MeV
m_{H}	125.74 ± 0.05 GeV	m_{d}	4.7 ± 0.05 MeV
v	246 ± 1 GeV	m_{u}	2.2 ± 0.05 MeV
θ_{12}	$13.04 \pm 0.05^\circ$	m_{s}	96 ± 6 MeV
θ_{23}	$2.38 \pm 0.06^\circ$	m_{c}	1.27 ± 0.03 GeV
θ_{13}	$0.201 \pm 0.011^\circ$	m_{b}	4.18 ± 0.04 GeV
δ_{13}	1.20 ± 0.08 rad	m_{t}	173.2 ± 0.9 GeV

TABLE 2.1: Summary of the free parameters of the SM.

Besides, the pp collisions are dominated by strong production of quarks and gluons that hadronize resulting in final states with jets. Other processes, such as the $\mathrm{t\bar{t}}$ production, contain jets in the final state. The modelling of the hadronization process, which is crucial to make the precise measurements presented in this thesis, is summarised in section 2.2.2.

2.2.1 Parton distribution functions

The distribution probability of the momentum of each parton inside the proton in a hard interaction with an energy transfer Q^2 is given by the parton distribution functions (PDF). The cross section of a given process in pp collisions, that gives the probability that such process is produced, can be calculated by factorising the effects of the soft interaction, which is absorbed by the PDF, and the partonic cross section $\hat{\sigma}$ as

$$\sigma = \sum_{j,k}^{partons} \int dx_j dx_k f_j(x_j, \mu_{\mathrm{F}}^2) f_k(x_k, \mu_{\mathrm{F}}^2) \hat{\sigma}(\hat{s}, \mu_{\mathrm{R}}, \mu_{\mathrm{F}}) \tag{2.34}$$

where $f_j(x_j, \mu_{\mathrm{F}}^2)$ and $f_k(x_k, \mu_{\mathrm{F}}^2)$ are the proton PDF of each parton and x_j, x_k are the momentum fraction of the parton ($x_j = p_j/p_p$, where p_j and p_p are the momentum of the parton j and the proton respectively). A new scale μ_{F}, called factorisation scale, is introduced, which can be interpreted as the energy scale at which the soft and hard effects are separated. The partonic cross section $\hat{\sigma}(\hat{s}, \mu_{\mathrm{R}}, \mu_{\mathrm{F}})$ depends on squared partonic centre-of-mass energy $\hat{s} = x_j x_k s$, being s the squared pp centre-of-mass energy.

The proton PDF have been accurately measured in electron-proton deep inelastic scattering (DIS) at HERA [21]. In this thesis, the NNPDF3.0 set of proton PDF [22] is used as nominal PDF set for theoretical calculations. The calculation of the PDF in this set and their uncertainties includes new data, with respect to the data used in the previous set of PDF for the LHC (NNPDF2.3) [23], from HERA DIS experiments [24–26] and several measurements from ATLAS and CMS collaborations such as jet production [27–29], vector boson rapidity and transverse momentum distributions [30–33], top quark pair production cross section [34–36] and $W + c$ data from CMS [37]. The dependence of the PDF with μ_R is derived using the DGLAP equations [38, 39]. The evolution of the initial-state radiation mainly depends on these equations. In figure 2.3 the PDF distributions from the NNPDF3.0 PDF set for different partons evaluated at $\mu = \mu_R = \mu_F = 10\,\text{GeV}^2$ and $10^4\,\text{GeV}^2$ are shown.

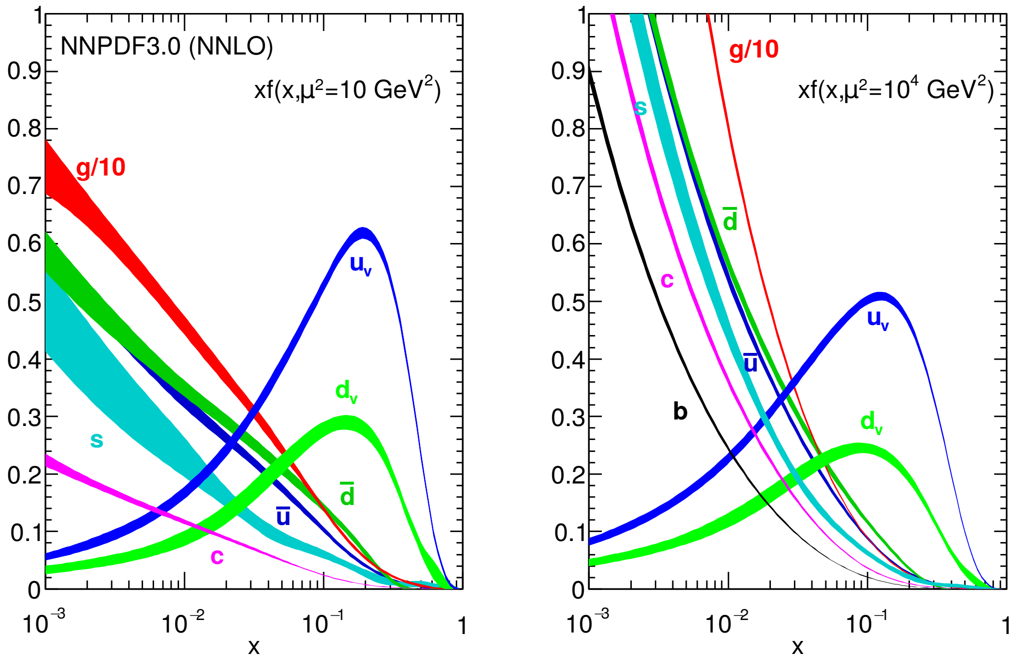

FIGURE 2.3: Proton PDF using the NNPDF3.0 PDF set, evaluated at $\mu^2 = 10\,\text{GeV}^2$ (left) and $\mu^2 = 10^4\,\text{GeV}^2$ (right) [22].

2.2.2 Modelling of the hadronization

When a parton is created in a hard process, first it showers into other partons in a process called fragmentation. The QCD perturbative calculations can only reproduce a limited part of these dynamics. After the fragmentation, all the partons undergo a transition to hadrons in a process called hadronization, that occurs at the non-perturbative QCD regime. The two parts are factorised into a perturbative and a non-perturbative contributions by using fragmentation functions. The perturbative calculation of the fragmentation also undergoes a DGLAP evolution. The modelling of the final-state radiation of the process mainly depends on this part of the parton-hadron transition.

The modelling of the fragmentation and hadronization processes is usually done using monte carlo (MC) event generators like PYTHIA [40] or HERWIG [41]. The MC modelling starts with the parton-level state of a given hard-scattering process. The matrix-element calculation of the hard scattering of complex processes is usually derived using external programs such as aMC@NLO [42] or POWHEG [43–46].

The parton fragmentation is generated up to some energy scale. After that, the kinematics of all the particles at parton-level are randomly generated. This is followed by the simulation of the parton shower, mainly based on the successive random generation of gluon emission ($q \to qg$) and gluon splitting ($g \to q\bar{q}$), which is repeated up to a partonic energy of about 1 GeV.

At this point, a hadronization model is used to convert all the partons into hadrons. Some colour reconnection models are available to achieve the formation of hadrons [47, 48].

On the other hand, in pp collisions the interaction between the remnant partons in the proton (that do not participate in the hard collision) has to be modelled. These partons generate what is called the underlying event (UE). Its modelling involves an additional parton-parton scattering that eventually produces a parton shower and hadronization process.

Finally, the final-state hadrons appear predominantly in collimated bunches of particles called jets. The jets are the final result from the showering and hadronization of a parton and are the only hadronic observables of the event, which are then detected and reconstructed in pp colliding experiments.

2.3 Limitations of the SM

The SM has obtained in multiple experiments for over 40 years a vast list of verified predictions, becoming the best particle physics model up to now. However, there are a few aspects that would let the physicists think of a more complete theory that could deal with some more fundamental questions.

To begin with, the SM as it has been presented in this chapter is missing the masses of the neutrinos. Several experiments in different contexts have shown that neutrinos experiment flavour oscilations. This fact requires a modification in the SM to introduce neutrino masses. There is not a general consensus on the exact mechanism that gives masses to the neutrinos (Higgs mechanism, seesaw...). The seesaw mechanism [49] predicts the existence of massive neutrinos, which have not been observed in nature by any experiment so far. On the other hand, several models assume that neutrinos are Majorana particles, but in the SM (as presented in this chapter) they are assumed to be Dirac fermions. There are no evidences to strongly support any of these hypothesis.

Apart from the SM extension on the neutrino sector, the SM hierarchy problem requires an incredible fine tuning of the parameters to explain the observed mass of the Higgs boson, as explained in section 2.3.1. This lack of naturalness is usually the strongest argument to search for new physics, beyond the SM (BSM), that could shed light on the hierarchy problem. On the other hand, there are some more open questions that might have to be handled by particle physics and would require the existence of BSM physics. Some of these questions are sumarized in section 2.3.2.

Several solutions are proposed to solve the hierarchy problem and other open questions, offering more fundamental theories. Probably the most popular is SUSY, which has been searched for experimental physicists during the last 30 years, especially in the last years at the CERN LHC. In this thesis a search for supersymmetric particles is presented in chapter 6. A summary of the main features of SUSY is presented in section 6.2.

2.3.1 The hierarchy problem

The value of the mass of the Higgs boson, m_{H}, is much smaller than the value that one could expect for a scalar boson in the theory. In fact, we would expect that the SM is a valid theory up to a scale of $\Lambda^2 \approx M_p^2$, where M_p is the Planck mass ($\sim 10^{19}$ GeV), and this scale corresponds to the energy at which gravity effects would become important. The large mass hierarchy given by $m_{\mathrm{H}}^2 \ll \Lambda^2$ is contrary to the fact that one would expect huge quantum corrections to m_{H}^2 that would approximate its value to M_p (or a mass of a new boson in the context of a more general theory).

Furthermore, the calculation in the SM of the radiative corrections to the bare Higgs boson mass (m_{H}^0) contains quadratic divergences as

$$\Delta m_{\mathrm{H}} = m_{\mathrm{H}} - m_{\mathrm{H}}^0 \sim \Lambda^2. \tag{2.35}$$

This is not a fundamental problem of the SM because in the context of the renormalization one can fix the value of the bare mass so it can cancel out the large term that is multiplied by Λ^2, of the order of $10^{38}\,\mathrm{GeV}^2$, resulting in the observed value of $\sim 10^4\,\mathrm{GeV}^2$. However, this magical cancelation implies an unnatural fine tuning of the parameters that suggest that some BSM physics should solve the problem. The most popular solution to the fine-tuning SM problem is presented in section 6.2.

2.3.2 Other open questions

Although the SM perfectly describes all the known particle physics phenomena, there are some physics problems that are not explained by the SM but could probably be solved with a deeper theory.

One of these problems comes from the astronomical observation of galaxies and galaxy clusters. The amount of matter in a galaxy or a galaxy cluster can be estimated by counting the number of stars (estimated, for example, by measuring the luminosity in the visible band) taking into account the mass contribution from interestelar gas and dust and small contributions from other astronomic objets. On the other hand, some observations as the rotation of stars around the centre of the galaxy or the distribution of the matter in interacting systems are highly dependent on the gravitational effect of the massive objects in their local surroundings.

Most astronomical observations show a large discrepancy between the observed matter and the gravitational effect of the mass in these objects [50, 51], suggesting that a large fraction of the mass of these astrophysical systems comes from invisible matter, called dark matter (DM). Similar effects have been also observed in gravitational lens effects of galaxy clusters [52].

The DM in the galaxies cannot be formed of any of the particles in the SM. New particles that may be described by some BSM theory can be considered DM candidates, being the most popular ones the so-called weakly interacting massive particles (WIMPs).

Other fundamental aspect of reality that is not described by the SM but could have an explanation in a BSM theory is the fact that our universe is mainly formed by matter and not antimatter. In the SM, the asymmetry between matter and antimatter can be derived from a violation of the CP symmetry. This symmetry is known to be violated in some SM processes, such as the decay of kaons and B mesons, but the amount of matter-antimatter asymmetry in these decays is not enough to explain the large asymmetry observed in the universe. Some piece of BSM physics could introduce CP-violating processes that could explain a large matter-antimatter asymmetry produced in the early universe.

Finally, an ultimate argument to search for new physics comes from the idea of unification of forces. This idea succeded already multiple times in history: Newton unified the classical and celestial mechanics, Maxwell unified electric forces and magnetism, quantum mechanics unified chemistry and electromagnetism... And, in particle physics, a new theory could unify the three SM forces and, eventually, include the gravitational force. Furthermore, the masses of the SM particles are free parameters of the theory, but a fundamental theory of the nature could possibly explain the masses of all the particles from more fundamental parameters.

From the multiple models that propose solutions to some (or all) of these questions, SUSY is one of the most popular. The basic principles of SUSY will be presented in section 6.2 and a search for new particles in this framework will be presented in this thesis.

Chapter 3

Experimental setup

3.1 The Large Hadron Collider

The LHC is the largest particle accelerator in the world. Located near Geneva, the LHC is a superconducting synchrotron built by CERN and it is hosted in a circular tunnel with a perimeter of 27 km, about 100 m underground. The LHC is designed to accelerate and collide different hadrons, including protons, lead nuclei and other heavy ions. The LHC is the last accelerator of the CERN accelerator complex, of which an schematic view is shown in figure 3.1. At the beginning of the accelerator chain, the protons are obtained from Duoplasmatron source, containing a bottle of hydrogen gas. The protons are first accelerated up to 50 GeV at the linear accelerator LINAC 2 (heavy ions are first accelerated at the Low Energy Ion Ring, LEIR). The next system is the Proton Synchrotron Booster, that accelerates the protons up to 1.4 GeV. After, they are accelerated by the Proton Synchrotron and Super Proton Synchrotron up to energies of 26 GeV and 450 GeV respectively. Finally, the protons are transferred to the LHC ring, where they travel in both directions of the circumference and are accelerated up to energies of 6.5 TeV. The LHC uses more than 1200 superconducting magnets to turn the particles, producing magnetic fields of up to 8.3 T.

In a collider experiment, the number of expected events N_{p} of a given process p is given by

$$N_{\mathrm{p}} = \sigma_{\mathrm{p}} \int \mathcal{L} dt \tag{3.1}$$

where σ_{p} is the total cross section of the process p and $\mathcal{L}$ is the instantaneous luminosity. This machine-dependent quantity can be expressed in terms of a set of parameters related to the beam properties, according to the following expression

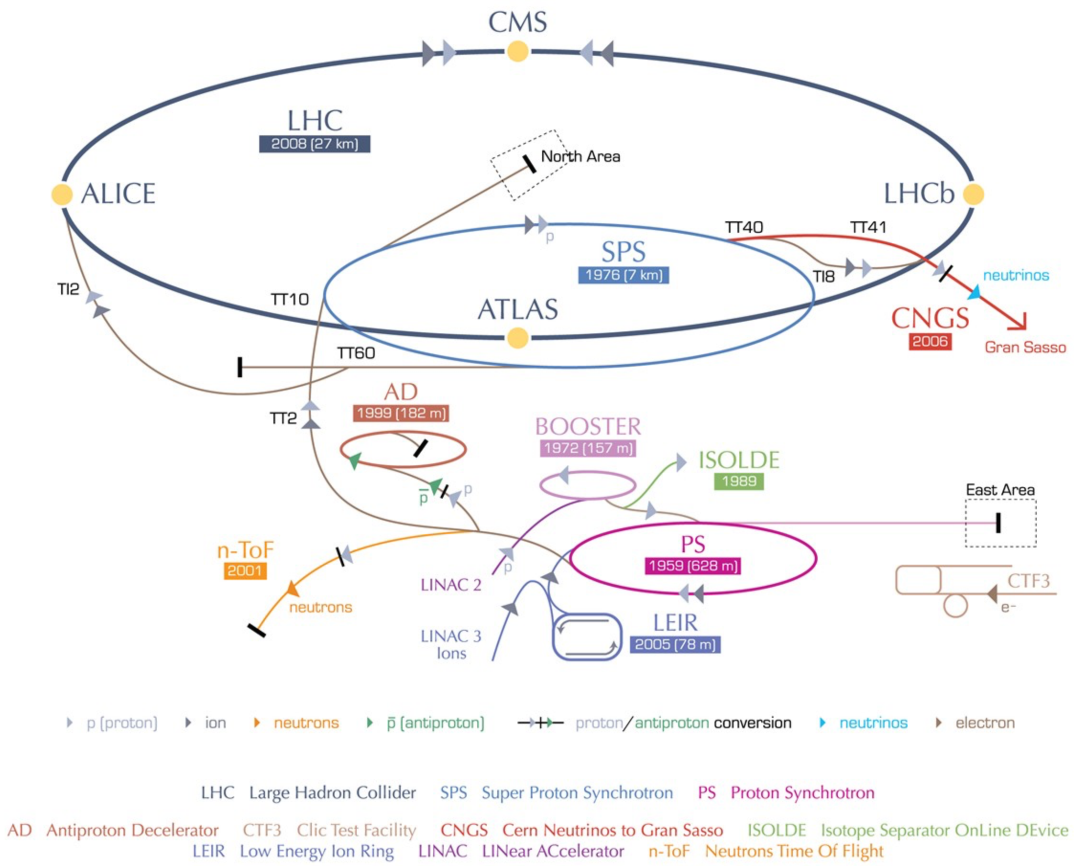

FIGURE 3.1: Representation of the CERN accelerator chain.

$$\mathcal{L} = \frac{n_b N_b^2 \cdot f}{4\pi \cdot \beta^* \cdot \varepsilon_n} \cdot R \tag{3.2}$$

where n_b is the number of bunches per beam, N_b is the number of protons per proton bunch, f is the beam revolution frequency in the LHC ring, β^* is the insertion region focusing parameter, ε_n is the normalised emitance and R is the interaction region geometric factor. The maximum design instantaneous luminosity of the LHC is $\mathcal{L} = 10^{34}\,\mathrm{cm}^{-2}\mathrm{s}^{-1}$, and the maximum design centre-of-mass energy in pp collisions is 14 TeV. At the end of the RUN 2, the instantaneous luminosity peak reached about twice the design value, while the maximum centre-of-mass energy in pp collisions was 13 TeV.

Taking into account the high luminosity working conditions of the LHC, more than one interaction between the protons are produced in each bunch crossing, although we are usually interested in one of the pp collisions in the event (the main collision). We call pileup (PU) to all the particles that are produced in all the other interactions in an event (within the same bunch crossing). These particles are detected and stored in the same event as the collision of interest and are separated from the particles coming from the main interaction. Their effect on the measurements are taken into account. The mean number of vertices ($\hat{\mu}$) during the 2015, 2016, 2017 and 2018 data-taking periods is 12, 23, 33, and 33, respectively, assuming an inelastic pp cross section of $\sigma_{\text{pp}} = 69.2\,\text{mb}$. A histogram showing the number of pp interactions per bunch crossing is shown in figure 3.2.

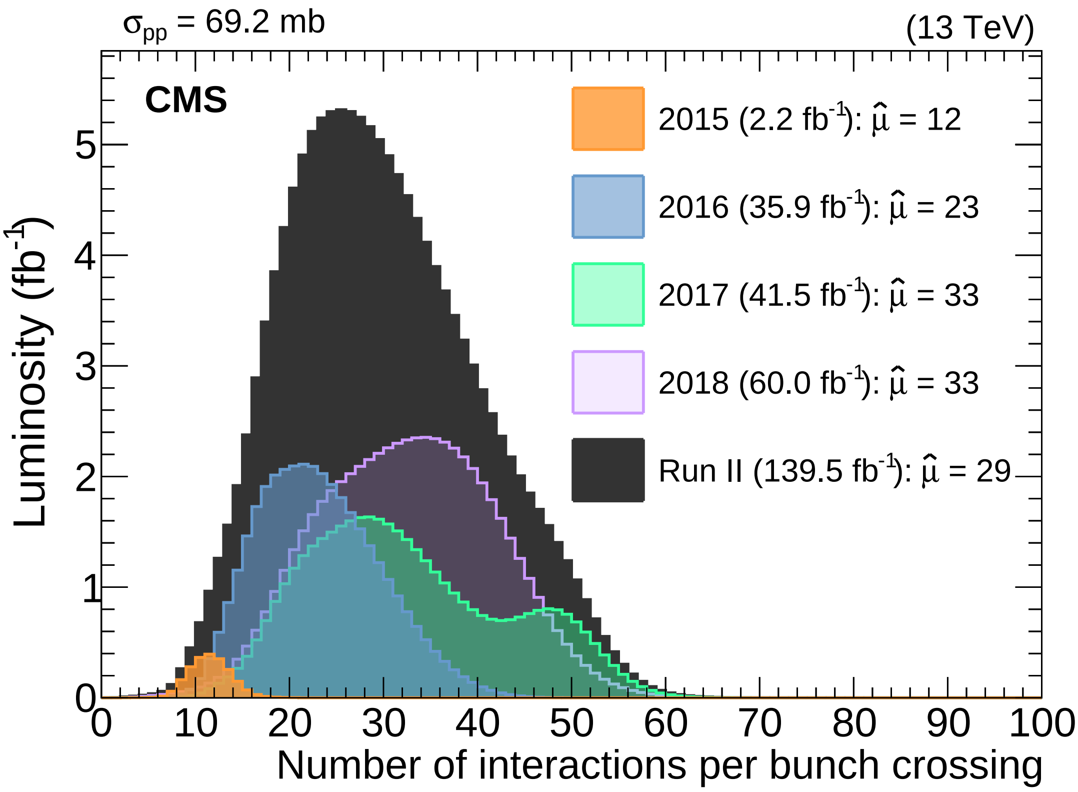

FIGURE 3.2: Distribution of the average number of interactions per crossing (pileup) for pp collisions in the different data-taking periods at $\sqrt{s} = 13\,\text{TeV}$. These plots use only data that passed the *golden* certification (i.e., all CMS sub-detectors were flagged to be OK for any kind of usage in physics analysis), and a value for the minimum bias cross sections of $\sigma_{\text{pp}} = 69.2\,\text{mb}$.

Since the starting of the LHC in 2009, a total integrated luminosity of almost $200\,\text{fb}^{-1}$ (inverse femtobarn, $1\,\text{b} = 10^{-28}\,\text{m}^2$) has been delivered, at different centre-of-mass energies, in pp collisions. A summary of the integrated luminosity as a function of the time, for different run periods, is shown in figure 3.3.

In May 2015, the LHC RUN 2 started. During the 2015 data-taking period, a total luminosity of $163.2\,\text{fb}^{-1}$ of data was delivered in pp collisions at $\sqrt{s} = 13\,\text{TeV}$. Two short runs of pp collisions at $\sqrt{s} = 5.02\,\text{TeV}$ delivered in 2015 and 2017 an amount of 28.8 and $334.3\,\text{pb}^{-1}$, respectively. The RUN 2 data taking ended on December 2018, followed by a two-years-long shutdown, until 2021.

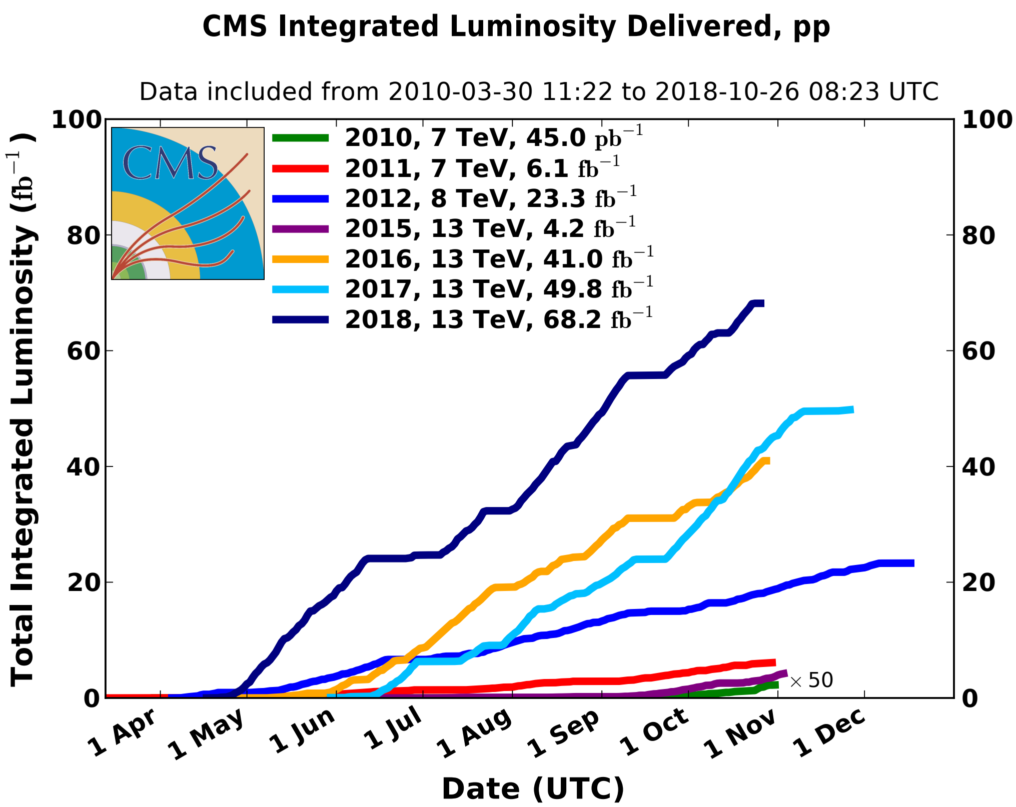

FIGURE 3.3: Delivered luminosity by the LHC for different data-taking periods and centre-of-mass energies. [53]

The collisions are produced in the centre of 4 large detectors: ALICE, LHCb, CMS and ATLAS. The last two are general-purpose detectors, optimised to measure precisely the energy of electrons and muons in a wide range of transverse momentum. Both detectors have reached their main goal in 2012: the discovery of the Higgs boson [7, 8]. In this thesis the measurements are done using data collected by the CMS detector, described in detail in section 3.2.

The next collisions are planned to be produced during the LHC RUN 3 scheduled to start in 2021. The LHC is expected to deliver an amount of at least 300 fb^{-1} during this period, at $\sqrt{s} = 13$ TeV and, probably, $\sqrt{s} = 14$ TeV. In the long term, the High Luminosity LHC (HL-LHC) is a major upgrade that will multiply the instantaneous luminosity by a factor 5. It is planned to start around 2036 and collect an integrated luminosity of about 3000 fb^{-1}. The experiments will be upgraded to deal with the extreme radiation conditions expected during the HL-LHC runs. A more detailed summary of these conditions will be presented in chapter 4.

3.2 The Compact Muon Solenoid

The CMS experiment [1] is one of the two general-purpose detectors of the LHC. It is designed to reconstruct all types of detectable particles produced at the collisions, providing the opportunity to study a wide range of particle physics phenomena.

The concept design of the CMS detector is driven by the huge superconducting solenoid, used to create a strong magnetic field in order to curve the trajectories of the charged particles. It consists of a 13 m-long coil based on a niobium-titanium material with an internal diameter of 6 m. It is situated in the central part of the CMS detector, called the barrel, centred around the interaction point. At both extremes of the barrel, along the beam pipe, several pieces of detector are situated, to reach a larger geometrical coverage. These regions are called the endcaps. The solenoid creates a magnetic field with a value of up to 3.8 T inside the magnet and of about 2 T outside (about 5×10^5 the intensity of the magnetic field of the Earth). The magnet return yoke in the barrel region is subdivided in 5 rings along the direction of the beam, each of about 2.5 m long, and are made up of 3 iron layers along the perpendicular direction. In the forward region, the return yoke is divided in 3 different iron disks in each of the endcaps.

The CMS detector is divided in several subdetectors. The tracker system is the innermost detector, starting at a few millimetres of the interaction point. Outside the tracker system, but still inside the magnet, two different calorimeters are situated: the electromagnetic calorimeter and the hadronic calorimeter. Outside the magnet coil, between the iron layers of the return yoke, the muon detectors are situated. A more detailed description of the CMS detector can be found in [1].

The CMS detector is being upgraded to deal with the changing conditions of the LHC runs. The most important upgrade during the Run 2 was the introduction of an extra layer of pixels in the innermost CMS subdetector. A major upgrade of the CMS detector is expected to happen before $\sim$ 2036 to cope with the HL-LHC conditions. In this thesis, longevity studies of the CMS drift tube chambers are presented in chapter 4. These studies aim to characterise the effects of the irradiation on this subdetector during the HL-LHC and propose strategies to optimise its performance.

Coordinate system and kinematic quantities. The CMS coordinate system has the origin centred at the nominal collision point. The z-axis goes along the direction of the beam and pointing towards the anticlockwise direction. The y-axis points vertically upward and the x-axis points radially towards the centre of the LHC ring. The azimuthal angle ϕ is measured in the x-y plane (transverse plane), from the x-axis.

The radial coordinate in this plane is r. The polar angle θ is measured from the z-axis. The momentum of the particles in the transverse plane (p_{T}) is usually measured with higher precision that the z component. The pseudorapidity is defined as $\eta = -\log[\tan(\theta/2)]$. It is 0 for particles travelling in the transverse plane and goes up to $\pm$ infinity for particles going along the beam pipe. This quantity is useful in particle physics as it is Lorentz-invariant for massless particles.

The momentum of the colliding particles in the transverse plane is very small in comparison with the momentum along the z-axis. The sum of the momentum of the outcoming particles in the transverse plane must be approximately equal to 0, by the law of the momentum conservation. The momentum imbalance is defined as

$$\vec{p}_{\mathrm{T}}^{\,\mathrm{miss}} = -\sum_i \vec{p}_{\mathrm{T}}^{\,i} \tag{3.3}$$

where $\vec{p}_{\mathrm{T}}$ is the transverse momentum vector and the index i goes through all the detected particles in the event.

The angular separation between two particles is usually measured in the η-ϕ plane, using the angular distance ΔR defined as $\Delta R = \sqrt{(\Delta\eta)^2 + (\Delta\phi)^2}$. This distance is also Lorentz-invariant for massless particles.

Figure 3.4 shows a schematic view of the CMS detector. In the following sections, the different CMS subdetectors are described.

3.2.1 The tracker system

The innermost CMS subdetector consists of a tracker system based on silicon semiconductor technology [54]. This subdetector is aimed to precisely identify vertices, electrons, muons and charged hadrons over a large energy range, by measuring their trajectories and extracting their curvature (driven by the magnetic field created by the solenoid). Its high granularity allows not only to precisely reconstruct tracks of the charged particles but also secondary vertices originating from the decay of particles containing b or c quarks or from the decay of a τ lepton.

The CMS silicon tracker is divided in two subsystems, pixels and silicon strip detector. A schematic view of the tracker detector is found in figure 3.5. The tracker system comprises 66 million pixels and 9.6 million silicon strips.

The pixel detector is situated very close to the interaction point. With a resolution of 10-15 μm, the pixel detector provides an excellent reconstruction of both primary

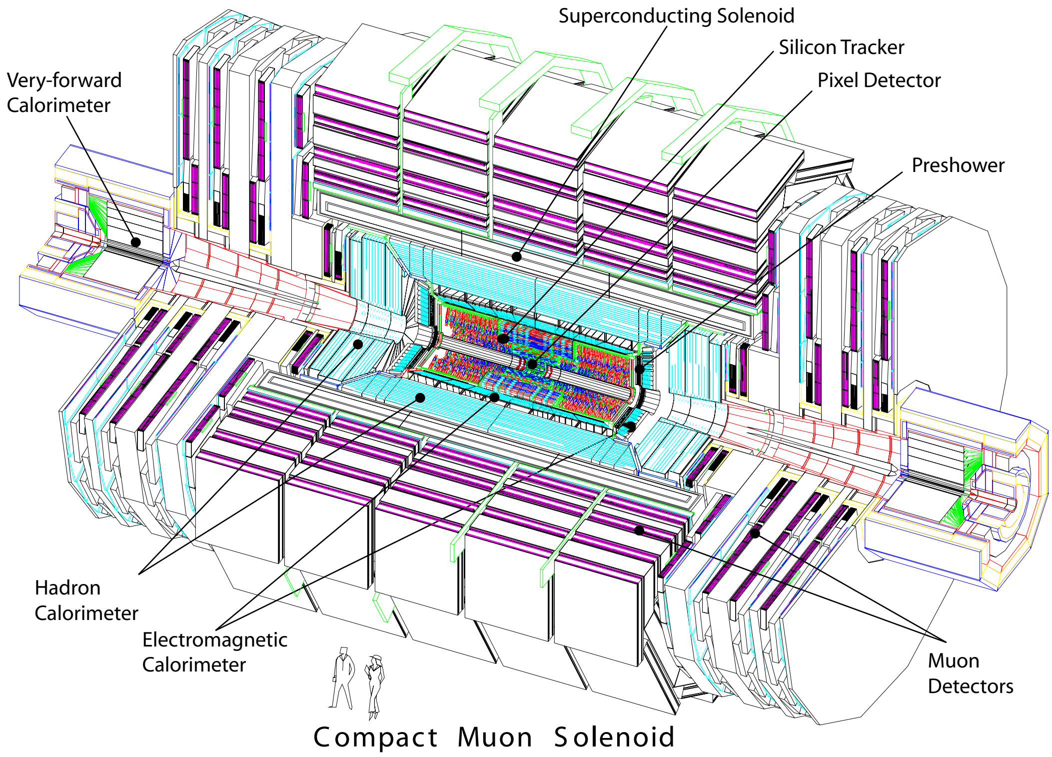

FIGURE 3.4: A schematic view of the CMS detector.

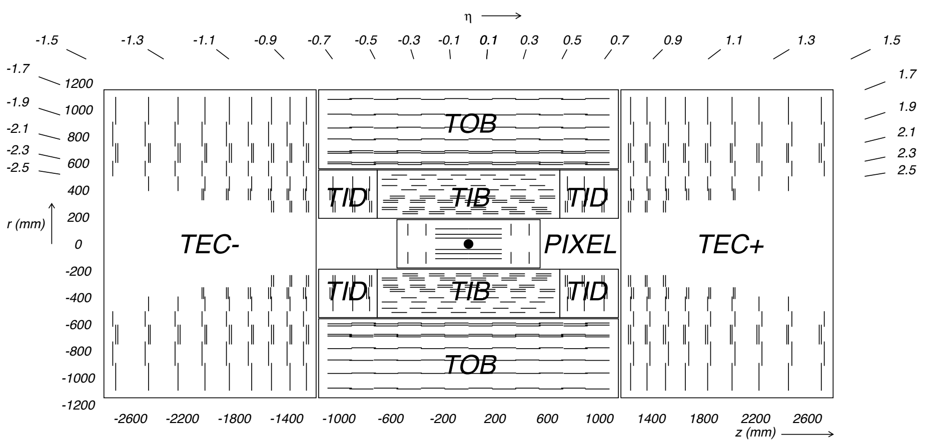

FIGURE 3.5: Schematic vision of the CMS tracker. Single lines represent detector modules and double lines indicate back-to-back modules.

(from the pp collision) and secondary vertices. The pixels are distributed in 4 layers (from 2017, 3 layers in 2016) in the barrel and 2 disks in the endcap.

The silicon strip system is located in 20 cm $< \mathrm{r} <$ 110 cm, arranged in 10 layers in the barrel and 12 disks in the endcaps. In the barrel, the strips are parallel to the z axis, while in the endcaps they are along the radial coordinate. In order to measure the z component with better precision that the strip length (about 10 cm) some tracker layers contain additional set of sensors inclined about 100 mrad with respect to the z axis. A precision of about 20-50 μm is reached in the $\mathrm{r} - \phi$ coordinate, while the resolution in the z direction is of 200-500 μm. The momentum resolution of the tracker system is

$$\frac{\sigma(p_{\mathrm{T}})}{p_{\mathrm{T}}} = \frac{0.015\%\ p_{\mathrm{T}}}{\mathrm{GeV}} \oplus 0.5\% \tag{3.4}$$

for $|\eta| < 1.6$. The relative error increases in the forward region up to $|\eta| < 2.5$ as

$$\frac{\sigma(p_{\mathrm{T}})}{p_{\mathrm{T}}} = \frac{0.060\%\ p_{\mathrm{T}}}{\mathrm{GeV}} \oplus 0.5\%. \tag{3.5}$$

The first term accounts for the measurement of the curvature of the particles, that becomes less precise for particles with higher momenta that are slightly bent by the magnetic field. The second term comes from the interactions with the tracker materials, such as multiple scattering.

3.2.2 The electromagnetic calorimeter

The electromagnetic calorimeter (ECAL) [55] is designed to precisely determine the energy of electrons and photons and measure the energy of the jets resulting in electromagnetic showers. It is an hermetic and homogeneous set of 61200 lead tungstate ($PbWO_4$) scintillating crystals mounted in the barrel, and 7324 crystals in each of the endcaps, providing a pseudorapidity coverage up to $|\eta| < 3.0$. Such a high dense material (8.28 g/cm^3) with a radiation length of 0.89 cm and a Molière radius of 2.2 cm, allows a very compact calorimeter system. An schematic view of the system is shown in figure 3.6.

The crystals in both barrel and endcap regions are oriented pointing to the nominal vertex position. They have a transverse section of $22 \times 22\,\mathrm{mm}^2$ and a length of 230 mm in the barrel and, a transverse section of $26.8 \times 26.8\,\mathrm{mm}^2$ and a length of 220 mm in the endcap. The crystals emit blue scintillating light, peaking in 425 nm, that is

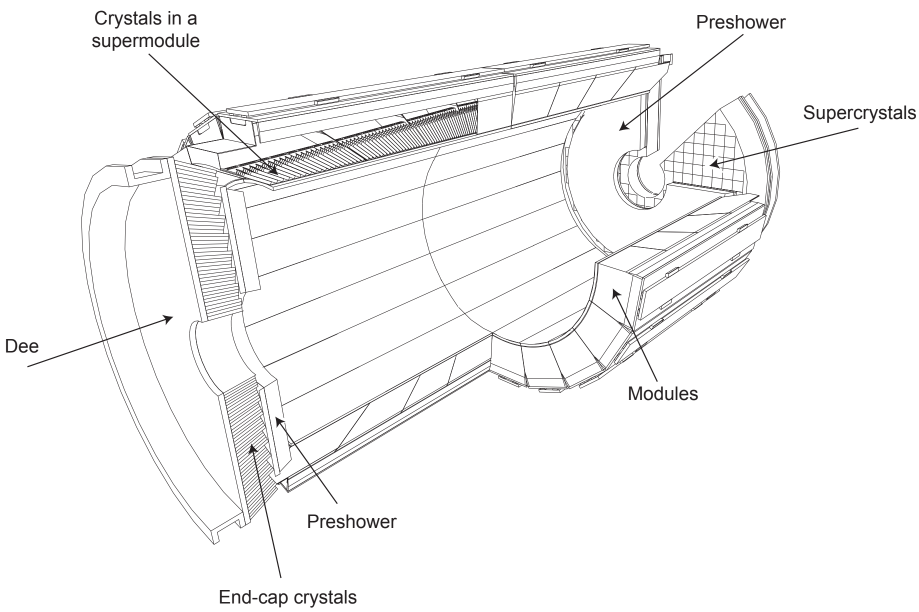

FIGURE 3.6: Layout of the electromagnetic calorimeter, showing several parts.

collected by silicon avalanche photodiodes in the barrel and vacuum phototriodes in the endcap.

The energy resolution of the ECAL is given by

$$\frac{\sigma(E)}{E} = \frac{2.8\%}{\sqrt{E/\mathrm{GeV}}} \oplus \frac{12\%}{E/\mathrm{GeV}} \oplus 0.3\% \tag{3.6}$$

being the first term the stochastic term, the second one is due to the electronic noise and the last one accounts for the non-uniformity of the detector and calibration uncertainties.

3.2.3 The hadronic calorimeter

The hadronic calorimeter (HCAL) [56] surrounds the ECAL and complements the measurement of the energy of the particles, providing hermeticity for a precise measurement of $\vec{p}_{\mathrm{T}}^{\mathrm{miss}}$. Its design is strongly influenced by the choice of the magnet parameters, as most of the detector lies inside the magnet coil. It is formed by 4 different subdetectors, covering a pseudorapidity range up to $|\eta| < 5$. An additional layer (HO) is mounted outside the magnet coil, providing some extra absorption. A schematic picture of one quadrant of the detector is shown in figure 3.7.

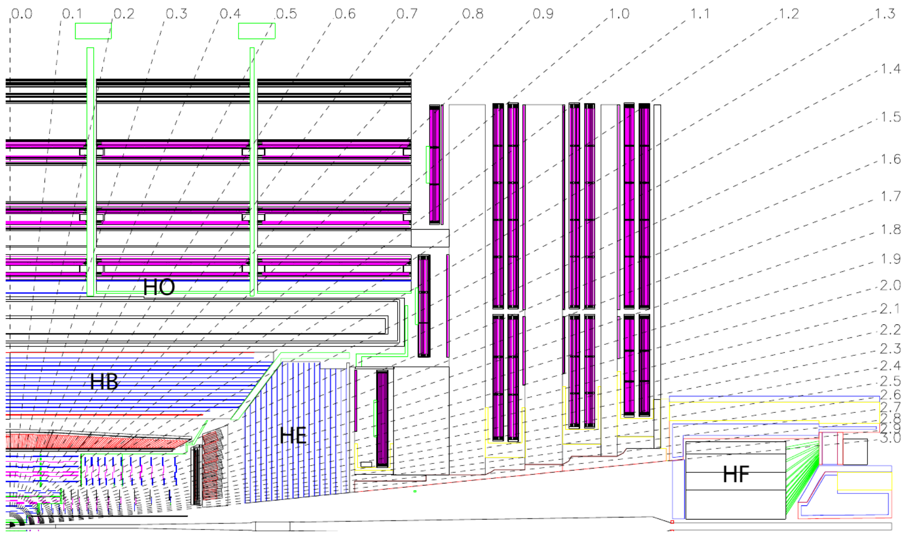

FIGURE 3.7: Layout of the hadronic calorimeter

The HCAL is composed by alternating layers of plastic scintillators and non-magnetic brass used as absorbing material, with an hadronic interaction length of 16.4 cm. The barrel hadronic calorimeter (HB) covers a region up to $|\eta| < 1.3$ and the endcap hadronic calorimeter (HE) covers a pseudorapidity of $1.3 < |\eta| < 3.0$. The very forward region, $3.0 < |\eta| < 5.0$, is covered by the forward calorimeter (HF), located at a distance of $|z| = 11.2$ m from the centre of the detector. In this subdetector, due to the higher levels of radiation, steel is used as absorber material and quartz fibbers are used as active medium.

The energy resolution of the HCAL is found to be

$$\frac{\sigma(E)}{E} = \frac{85\%}{\sqrt{E/\mathrm{GeV}}} \oplus 7.4\% \tag{3.7}$$

where the first uncertainty corresponds to the stochastic term and the second accounts for calibration uncertainties.

3.2.4 The muon system

The CMS muon system [57] is, in size, the largest CMS subdetector. It is situated outside of the magnet coil and extends up to r = 8 m in the radial direction. Its main purpose is to identify muons and accurately measure their momenta. Muons are the only detected particles that leave the detector before stopping and being absorbed or decaying, so they leave a unique trace in the muon detector.

The muon system is situated between the different layers of the iron return yoke, which provides some extra attenuation for the radiation background of particles (mainly neutrons) that are not stopped by the HCAL. The strong magnetic field of about 2 T inside the iron yoke makes the muons to bend, providing an extra curvature of the trace outside the magnet coil that helps determining the momentum of the muons.

A layout of the muon system is shown in figure 3.8. The system is formed by 3 subsystems of gas detectors based on different technologies: the drift tubes (DT) in the barrel, the resistive plate chambers (RPC) in both barrel and endcap and the cathode strip chambers (CSC) in the barrel.

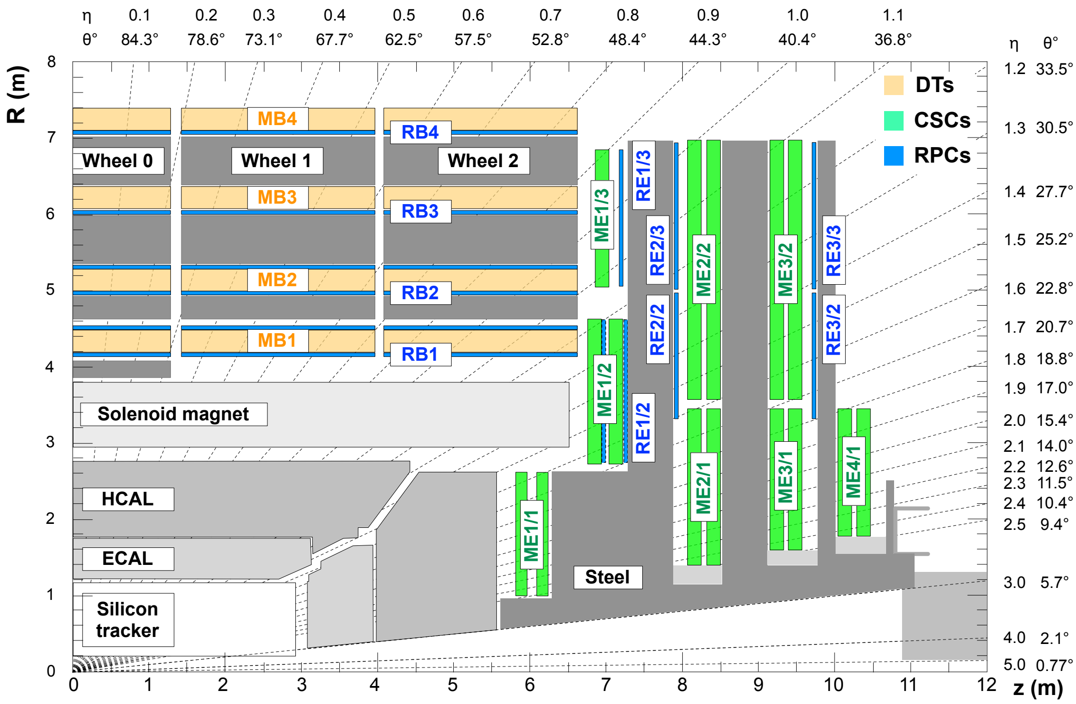

FIGURE 3.8: Layout of a quadrant of the CMS muon system. The chambers are named MB for muon barrel, corresponding to DT chambers, and ME for muon endcap, corresponding to CSC chambers. The RPC chambers are named RB and RE for barrel and endcaps, respectively.

3.2.4.1 Drift tube chambers

The drift tube chambers consist of individual 2.1 m-long drift tube cells containing an anode wire of 50 μm of diameter and two electrode plates. The 4.2 cm-wide cells are grouped in layers of about 50 to 100 cells. The DT chambers are formed by three (or two) superlayers, formed each with four layers and staggered by half a cell. The DT chambers are filled with a mixture of Ar (85%) and CO_2 (15%). A high voltage of about 1800 V is kept between the anode wire and the cathode strip, producing a gain of about 100 with a drift time of up to 380 ns.

The DT system is divided in five wheels, displaced along the z axis and centred on the nominal vertex position. Each wheel is divided in 12 sectors that cover different ϕ ranges. Each sector contains a stack of 4 DT chambers. The outer superlayers of each DT chamber contain wires parallel to the beam line and provides a measurement of the position in the transverse plane of the muons, while inner superlayers have cells oriented perpendicular to the beam line, so a measurement of the muon position on the z direction can be obtained.

The DT chambers provide a very precise measurement of the momentum of the muons, covering pseudorapidities up to $|\eta| < 2.1$. A more complete description of the DT chambers can be found in Section 4.3.

3.2.4.2 Cathode strip chambers

The CSC chambers cover the endcap region, $0.9 < |\eta| < 2.4$, where the magnetic field is not uniform and the neutron background is higher. The design of the CSC chamber is driven by the high granularity, fast response and high tolerant to radiation. The CSCs are multiwire proportional chambers consisting of anode wires interleaved among seven cathode planes. The CSC chambers are mounted in four disks perpendicular to the beam line. The innermost disks contain three concentric rings while the other ones contain two concentric disks. Each disc contains several trapezoidal chambers.

3.2.4.3 Resistive plate chambers

The RPC chambers are gaseous parallel-plate detectors that combine moderate spatial resolution with very precise time measurement. They are mounted on top of the DT and CSC chambers in the region of $|\eta| < 1.6$.

The CMS RPC chamber consists of two gaps operated in avalanche mode with readout strips in between. The total induced signal is the sum of the induced signal in both gaps. Compared to the DT and CSC detectors, the spatial resolution of the RPC chambers is lower but the time resolution is much better, of around 1 ns, complementing the measurements done by the other muon chambers.

3.2.5 The trigger system

The LHC produces collisions at a rate of 40 MHz but the current technology allows to store only about 1 kHz of bunch crossings. The CMS trigger system was designed to achieve this rate of data taking, selecting collisions that contain certain signatures, mostly related to the presence of muons or high energy depositions on the calorimeters. The CMS trigger is divided in two stages: the Level-1 trigger (L1), based on hardware, with an output rate up to 100 kHz, and the High-Level trigger (HLT), based on software.

The L1 trigger uses only low-resolution information from the muon chambers and the trigger, leaving out the information from the tracker in this first stage. The entire event read-out is stored in dedicated buffers for a maximum of 4 μs before being either discarded or sent to the HLT stage. The L1 is organised in local, regional and global trigger. The L1 is first driven by object seed identified locally by the subdetectors. The information from the reconstruction of several subdetectors are combined into the regional trigger to create L1 objects, e.g. muons, electrons, jets with a estimate of their transverse momentum and other properties. The L1 objects are further combined into the global trigger (GT) which finally selects or rejects events based on programmable trigger requirements.

The calorimeter triggers obtain seeds from signal in calorimetric towers. These towers contain information about transverse energy and the associated bunch crossing. The muon triggers process information from the three subdetectors of the muon system. The seeds are created on individual chambers and the information of the reconstructed tracks is combined between chambers and passed to the GT.

The HLT trigger can access to information from the whole detector and produces similar reconstruction as for the offline analysis, but it is optimised to reduce the computing time for each event and use only the needed information from the detector. In a first stage of the HLT reconstruction (L2), the information from calorimeters and the muon system given by the GT is used to reconstruct the particles with higher precision compared to the L1 reconstruction. The selected events are passed to the so-called L3 stage, that combine the L2 particles with information from the tracking detector and perform a full reconstruction of tracks and vertices. The typical HLT processing time for event is around 100 ms.

The L3 trigger applies a tighter selection requirements. The selected events are classified into different HLT paths. These paths are designed to select events with some specific physical properties. All the events that can be classified in at least one trigger path are stored permanently. These events are grouped in non-exclusive datasets, containing events with some similar physical properties, such as the presence of one muon or one electron-muon pair.

3.3 Event reconstruction at CMS

This section describes the basic methods used for the object reconstruction in the CMS experiment.

3.3.1 The Particle Flow algorithm

The Particle Flow (PF) algorithm [58] is used in CMS to reconstruct individual particles using information from all the CMS subsystems. The particles are identified as electrons, photons, muons, charged hadrons and neutral hadrons and their energy and momentum is determined using information in the whole detector. The output list of particles is used to clusterize hadronic jets, formed by the production of quarks or gluons whose momentum and direction is determined, and to compute the $\vec{p}_{\mathrm{T}}^{\mathrm{miss}}$ in the event.

The information from PF candidates is also used to identify hadronically decaying τ leptons and b jets or other types of jets using techniques of secondary vertex reconstruction and other methods.

3.3.1.1 PF isolation and PU corrections

Isolation of some particles, especially electrons and muons, is computed using PF candidates. The relative isolation of a lepton ℓ is defined as

$$I_{\mathrm{PF}}^{\ell}(\Delta R) = \frac{\sum p_{\mathrm{T}}^{\mathrm{ch}} + \sum E_{\mathrm{T}}^{\mathrm{neu}} + \sum E_{\mathrm{T}}^{\gamma} - p_{\mathrm{T}}^{\mathrm{PU}})}{p_{\mathrm{T}}^{\ell}} \tag{3.8}$$

where $p_{\mathrm{T}}^{\mathrm{ch}}$ is the transverse momentum of the charged PF candidates, $E_{\mathrm{T}}^{\mathrm{neu}}$ is the transverse energy of neutral hadrons, E_{T}^{γ} is the transverse energy of photons and the sums run over the charged PF candidates, neutral hadrons and photons, respectively, within a cone of ΔR around the lepton direction. The charged candidates are required to originate from the same primary vertex as the lepton. The $p_{\mathrm{T}}^{\mathrm{PU}}$ term corresponds to a correction related to particles coming from the pileup of the event. The pileup has a crucial effect on the computation of the isolation and the contribution from pileup particles must be removed from the isolation cone.

For electrons, the contribution from pileup particles in the isolation cone is computed using the average energy density per unit of area, ρ, assuming $p_{\mathrm{T}}^{\mathrm{PU}} = \rho \cdot\ A_{eff}$, where A_{eff} is called a effective area. The dependence of ρ with the number of reconstructed primary vertices is measured for the different PF components contribution to the numerator in (3.8). The dependency is almost constant for charged hadrons, as their traces are required to come from the same primary vertex as the lepton, and ρ and the isolation components for neutral hadrons and photons increases lineally with the number of vertices. The effective area is the defined as

$$A_{eff} = \Delta R^2 \cdot m \tag{3.9}$$

where m is the ratio between the slopes of the linear relation of ρ and a given isolation component with the pileup.

For muons, another alternative strategy to remove the PU from the computation of the isolation is used. A correction factor β is applied to the numerator in the computation of the isolation. The factor calculated from the estimation of the neutral part of the PU contribution to the isolation. This neutral component is estimated to be a third of the total PU contribution, so it can be estimated by measuring the momenta of all the charged particles not associated to the primary vertex and applying a factor of one half.

3.3.2 Reconstruction of tracks and vertices

The CMS inner tracker is used to measure the trace of charged particles that go through the detector. The curvature produced by the magnetic field is measured, from which the p_{T} of each particle is obtained. The reconstruction of muons combine the information from the detected traces in the tracker and the traces in the muon system. The electrons are reconstructed from traces in the tracker detector that are matched with electromagnetic deposits in the ECAL.

All the trajectories of the charged hadrons are also measured in the tracker. The trace of all the reconstructed particles is extrapolated to the position of each particle in the beam line to measure their impact parameters and reconstruct the primary vertices, from which the pp interactions occur, and secondary vertices, which are fundamental to identify heavy flavour decays.

The track reconstruction in CMS consists in three different steps: seeding, pattern recognition and final fit. A recursive algorithm is used, starting from a set of input hits, reconstructing tracks that must pass through a list of quality filter. If a good track is reconstructed, their hits are removed from the input set for the next iteration.

The seeds are generated by searching for pairs of triplets of hits compatibles with a hypothetical track coming from the interaction region. For events with high pileup, the combinatorics of the seed generation can be very high. To reduce the possible cases, hits whose charge distribution is not compatible with the incidence angle are ignored.

The pattern recognition is based on a combinatorial Kalman filter method [59]. The filter starts from the seed layer and a coarse estimation of the track parameters. The algorithm proceeds iteratively, including the information of the successive detection layers one by one. The track parameters are known with a improved precision with every added layer.

The trace is extrapolated to the new explored layers using the equations of motion for a charged particle in a constant magnetic field, accounting for multiple scattering and energy loss in the material. Several hits may be compatible with the extrapolated trace, so more that one candidate is created. The possible trajectories with no associated hits in a given layer are also considered in the next iteration, to account for the possibility that the track did not leave any hit on that particular layer, (what is called an *invalid hit*).

All the trace candidates are reconstructed in parallel and the process is repeated until all the layers are explored or a stopping condition is satisfied.

3.3.3 Electron reconstruction

Electrons are reconstructed by matching charged tracks in the inner tracker with energy deposits in the ECAL [60]. The energy deposits in the ECAL are clustered together, starting from a seed (the crystal with a larger energy deposit) and adding the energy deposits in adjacent crystals, forming ECAL superclusters (SC). For electron reconstruction, these superclusters typically include smaller clusters produced by the interaction of the electron and the photons that are irradiated by the electron and deposit their energy with a spread in ϕ.

The reconstruction of electrons can use either ECAL or tracker seeds. For electron reconstruction seeded by the ECAL, the ECAL SC are matched to electron tracks. When the seed is a charged particle reconstructed in the tracker, the traces are extrapolated to the ECAL and matched with SCs, taking into account the possible bremsstrahlung radiation emitted by the interaction of electrons with the material.

The electron trajectories are reconstructed using a dedicated model of electron energy loss in the tracker and are fitted using a gaussian sum filter. The reconstruction of the track is finally combined with the ECAL deposits associated to measure the momentum and the energy of the electron.

Several quality cuts are applied on different electron variables to select well reconstructed electrons and reject possible fakes from misreconstructed jets. The signal electrons, coming from the decay of an electroweak boson or a τ lepton (called *prompt* electrons) are detected as isolated tracks, while electrons coming from the decay of b or c quarks or charged hadrons misidentified as electrons (*nonprompt*) have larger deposits of energy around. Moreover, isolation requirements are also set to selected electrons, in order to reject nonprompt electrons.

The angular distances in pseudorapidity and polar coordinate, $\Delta\phi_{In}$ and $\Delta\eta_{In}$, between the extrapolated track position in the innermost layer and the closest position of the matched ECAL supercluster, increase with the amount of bremsstrahlung and are used to reduce the misidentification probability.

The width of the reconstructed ECAL shower in the direction of η is expressed in terms of $\sigma_{i\eta i\eta}$, defines as:

$$\sigma^2_{i\eta i\eta} = \frac{\sum(\eta_i - \eta)^2}{\sum \omega_i} \tag{3.10}$$

where the sum runs over the 5×5 matrix of crystals around the highest-E_{T} crystal of the supercluster, and the ω_i weights depend logarithmically on the contained energy. The discrimination power of this variable to reject nonprompt electrons is greater than the analogous variable in ϕ because the bremsstrahlung tends to change the pattern of the energy depositions along the ϕ direction.

Another quantity that discriminate between prompt and nonprompt elections is $1/\mathrm{E} - 1/\mathrm{p}$, where E is electron energy from the SC and p is the momentum of the electron track. Signal electrons tend to have a value of $(1/\mathrm{E} - 1/\mathrm{p})$ close to 0, while nonprompt electrons have negative values.

The isolation of an electron is measured using PF candidates within a cone of $\Delta R = 0.3$ around the electron candidate, as defined in equation (3.8).

The performance of the electron reconstruction in CMS can be found in [61].

3.3.4 Muon reconstruction

The muon reconstruction in CMS relays on both tracker detector and muon chambers. In the gas detectors, muon segments are first reconstructed in each station by fitting the detected hits in each of the layers. After, the segments between stations are matched together to produce a standalone muon track. Muon tracks are finally matched to tracks in the inner tracker to fully reconstruct the muons. This reconstruction can be done either inside-out or outside-in.

The tracker muons are reconstructed inside-in. All the reconstructed traces in the tracker with momentum $p^{\mu} > 2.5\,\text{GeV}$ are considered muon candidates and extrapolated to the muon chambers. In the extrapolation, the magnetic field, expected energy loss and multiple scattering effects are taken into account. The extrapolated track is considered a tracker muon if it matches a segment in at least one muon station.

On the other hand, global muons can also be reconstructed outside-in. Standalone muon tracks, reconstructed with one or multiple muon chambers, are back extrapolated to match a trace in the tracker. The global muon track is fitted combining hits from the tracker and the muon chambers, using the Kalman filter method [59].

About 99% of the muons produced in pp collisions in the CMS acceptance are correctly reconstructed by one of the two methods, and most of the times, by both methods. The reconstruction of global muons has better momentum resolution that the tracker muon reconstruction for high-p_{T} muons ($p_{\mathrm{T}} > 200\,\text{GeV}$), while tracker muon reconstruction is more efficient at low momentum ($p^{\mu} < 5\,\text{GeV}$) as these muons may not go through the whole CMS muon detector, but the reconstruction requires only one matched station.

Several additional criteria can be added to the muon identification to obtain a sample of robustly reconstructed prompt muons and reject muons produced in heavy-flavour decays or wrongly identified tracks, as hadron punch-through. The set of applied identification criteria is usually based on a balance between efficiency and purity. Furthermore, signal muons are usually isolated, while background muons tend to be rounded by other particles (as particles from hadronic jets), so further isolation cuts are applied.

Matching with PF muon candidates may reduce the amount of background muons. The χ^2/dof of the fit to the global track of the muon is a good discriminant to suppress the selection of muons from in-flight decays. Also, requirements on the impact parameter of the muon are useful to separate muon coming from the primary vertices from muons coming from heavy-flavour decays.

The PF isolation, as defined in equation (3.8) is used to require isolated muons. The radius of the cone used is $\Delta R = 0.4$.

3.3.5 Jet reconstruction and b tagging

The reconstruction of jets at CMS uses PF candidates to determine the momentum and direction of the jet, reaching a much better resolution in both quantities than using calorimetric jets. PF candidates are clustered into jets using the anti-k_T algorithm [62]. The clustering produces cone-shaped jets with a given angular width ΔR. The jets used in this thesis are reconstructed using the described method with $\Delta R = 0.4$.

The measured energy of the jets needs to be corrected to account for the PU contribution, particles from the underlying event, non-uniformity of the detector, calibrations, etc. A set of different corrections (JEC) is derived and applied to the jet energy sequentially.

First, an offset correction, estimated from MC, is applied to the jets to account for PU and UE particles. The factor is estimated by computing the per-event median energy density by using jet areas [63]. After, a calibration based on MC is applied to remove most of the effects of the detector response due to non-uniformity in η and the non-linearity in p_T. Finally, the residual corrections are applied to account for small differences between data and simulation. These corrections include specific studies on correcting the energy for subsets of jets with different flavour (b jets, c jets, jets from gluons, etc.). A scheme of the JEC applied to data and MC can be found in figure 3.9.

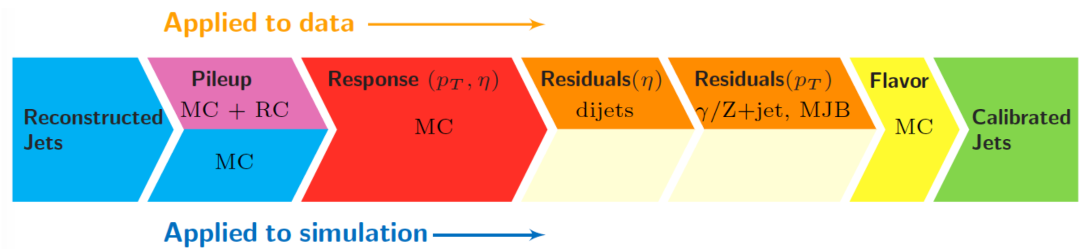

FIGURE 3.9: A schematic summary of the jet energy corrections applied to both data and simulation reconstruction.

From the jet identification, the H_T variable is defined as the scalar sum of the jet p_T of all the reconstructed jets in the event

$$H_T = \sum_i p_T^{\text{jet}}[i]. \tag{3.11}$$

This variable characterises the hadronic activity in the event.

3.3.5.1 Identification of jets originating from b quarks

The identification of jets originating from the hadronization of a b quark (b tagging) is a very powerful tool to discriminate events from processes containing b quarks, such as $t\bar{t}$ events. The b-tagging algorithms exploit the kinematics induced by the relatively long lifetime of B hadrons, such as a long impact parameter of the reconstructed jet with respect to the primary vertex.

In the analysis presented in this thesis the Combined Secondary Vertex (CSVv2) algorithm [64] is used to tag b jets. This algorithm uses multiple information from the tracks of each jet, mostly related to the primary vertex and the presence of a secondary vertex, and computes a discriminant variable assigned to each jet, with a value from 0 to 1, that indicates for a given jet how likely is to have been originated from a b quark.

A jet is considered as b tagged if its CSVv2 discriminant value is larger than a previously chosen value called working point. The b-tagging efficiency of the algorithm and the mistag rate are measured in data for each value of the working point. The value of the working point used in a given analysis usually depends on the mistag rate tolerated by the analysis (typically, 10%, 1% or 0.1%).

3.3.6 Missing transverse momentum

The missing transverse momentum vector is calculated in CMS using PF candidates, following the expression in (3.3), using both clustered and unclustered PF candidates. The $\vec{p}_{\mathrm{T}}^{\,\mathrm{miss}}$ can be corrected applying to the PF candidates that are clustered in jets similar JEC as for the jets. In this case, the corrections are applied only to jets with $p_{\mathrm{T}}^{jet} > 10\,\mathrm{GeV}$, so the corrections can be measured with sufficient accuracy.

This quantity indicates the presence of undetected particles in the event. Even if there are no invisible particles in the event, the $p_{\mathrm{T}}^{\mathrm{miss}}$ differs from zero because of several effects: related to the detector (energy resolution, detector noise, misreconstructed particles, uncertainty on JECs...) or due to the pileup and the underlying event. The impact of this effect can be measured in pp collisions using $\mathrm{Z} \to \mathrm{e}^+\mathrm{e}^-$ and $\mathrm{Z} \to \mu^+\mu^-$ events, where no invisible particles are expected.

Chapter 4

Upgrade of the CMS Drift Tubes

4.1 Introduction

The $t\bar{t}$ cross section precision measurements and the search for SUSY particles presented in this thesis have been possible thanks to the fantastic performance of the CMS detector during the full Run 1 and Run 2 periods. During the data taking, the CMS operation is constantly supervised by a team of experts for each CMS subdetector. In particular, I took part in the operations of the DT system for several weeks during the Run 2.

Moreover, the performance of each subdetector is monitored and improved during the data taking, continuously adapting the working conditions to the LHC run conditions to optimise the performance of the detector, trigger system and reconstruction algorithms. A major upgrade of the LHC accelerator, that requires an upgrade of the CMS detector, is expected to be developed during the next decade. With this upgrade, the CMS DT system will have to deal with extreme radiation conditions and some improvements must be developed to keep the performance of the trigger system and muon reconstruction.

In this context, from January 2016 I was responsible for the data quality certification at CMS from the point of view of the DT system, as a part of the service work tasks. To check the quality of the muons measured by the DT subdetector, the Data Quality Monitoring tools from CMS were used. These tools produce hundreds of plots for each CMS run of cosmics or pp collisions where several aspects of the data taking and muon reconstruction are monitored, including the status of the read-out, correlations between triggers, occupancy of each cell, efficiency computation, residuals and others.

With this task I was introduced to the technical details of the operations of the detector and the DT standalone muon reconstruction.

In this chapter, longevity studies of the DT system are presented. These studies have been conducted during 2017, 2018, and 2019 at the CERN Gamma Irradiation Facility (GIF++).

4.2 The High Luminosity LHC

During the Run 2 the CMS experiment has recorded an integrated luminosity of more than 165 fb^{-1}, including collisions at several centre-of-mass energies and different collision systems. This enormous amount of data has allowed the CMS collaboration to explore a wide range of particle physics phenomena including the discovery of the Higgs boson in 2012. The CMS results also include multiple SM measurements and searches for new physics, as the ones presented in this thesis.

An upgrade of the LHC is planed to extend the sensitivity of BSM searches. The upgraded accelerator is called the High Luminosity Large Hadron Collider (HL-LHC) and is planned to produce pp collisions at $\sqrt{s} = 14\,\mathrm{TeV}$ with very high luminosity conditions. The current phase-1 is expected to end in 2023 after having delivered about 300 fb^{-1} of data at $\sqrt{s} = 13\,\mathrm{TeV}$. A three-years-long shutdown is expected after the end of the phase-1 in order to upgrade the accelerator and the detectors. The HL-LHC is expected to produce the first collisions in 2026, starting the phase-2.

The HL-LHC will provide pp collisions at an instantaneous luminosity about a factor 5 larger than the current LHC luminosity. It has a design value of $5 \times 10^{34}\,\mathrm{cm}^{-2}\,\mathrm{s}^{-1}$ and an ultimate value, expected to be reached in the last years of the phase-2, of about $7.5 \times 10^{34}\,\mathrm{cm}^{-2}\,\mathrm{s}^{-1}$. The HL-LHC run is planned to run for a decade collecting about 3000 fb^{-1} of pp collisions.

One of the main goals of the CMS upgrade is improving the detector performance to allow a precise reconstruction of all the particles in the high-pileup conditions of the HL-LHC with about 200 interactions per bunch crossing. Also, the electronics will be updated to be able to improve the data taking and the acceptance of the detector, that will be extended from $|\eta| < 2.4$ to $|\eta| < 4.0$. Furthermore, this increase in the collision rate entails an increase in the exposure to high levels of radiation of the CMS subdetectors.

This continuous exposure to radiation for more than a decade will affect the performance of the muon detectors, that will have to deal with an ageing effect produced by the damage to the detector and electronics produced by the radiation. In particular, the drift tubes detector, that provide a precise measurement of muons in the barrel region, will be upgraded to cope with the HL-LHC conditions and still provide a $\approx 99\%$ reconstruction efficiency for barrel muons during the whole period. In this chapter, the ageing studies of the CMS drift tube chambers are presented.

4.3 The CMS Drift Tubes

A basic description of the CMS muon detector can be found in section 3.2.4. In this section, a more detailed description of the CMS drift tubes detector is presented. The CMS DT system is the largest CMS subdetector. It is the main responsible of correctly identifying muons in the CMS barrel region, at $|\eta| < 1.2$. It consists of 250 stations divided in five wheels (Wh-2, Wh-1, Wh0, Wh+1, Wh+2) extended around the pipeline, in the transverse plane, where the number of the wheel indicates its z position: Wh0 is around the CMS nominal centre, Wh-1 and Wh-2 are situated towards negative values of z, Wh+1 and Wh+2 are located towards positive values of z.

Each wheel is subdivided in 12 sectors. Each of them covers a different φ region. Each sector is composed by four DT stations (except for horizontal sectors, 4 and 10, that contain 5 stations). A layout of a wheel is shown in figure 4.1.

The innermost stations of each sector are called MB1 stations (or chambers). Next in the radial direction, the stations are called MB2, MB3 and MB4, respectively. The longitudinal size (in the φ direction with respect to the CMS coordinates) of outer stations is larger, so they can cover the full circumference. In sectors 4 and 10, as shown in figure 4.1, the MB4 stations are divided into two smaller chambers in order to keep a maximum length of about 4 meters. The size in the direction along the Z axis is the same for all the stations, 2.536 m, and the thickness of the stations as well, of 29 cm.

Each station contains 12 (or 8 for the MB4 stations) layers of DT cells. The cells are about 4.2 cm thick and are orientated either in the Z direction or perpendicular, along the φ direction. The layers are grouped in packs of 4 called superlayers (SL), each of them named L1, L2, L3 and L4 along the R direction. Depending on the orientation of the cells, the SL are called Θ if the cells are orientated in Z direction and Φ if the cells are along the φ direction. Consecutive layers in a SL are staggered by half a cell to improve the precision in the measurement of the position of the muon hits. A schematic picture of a standard DT station is shown in figure 4.2.

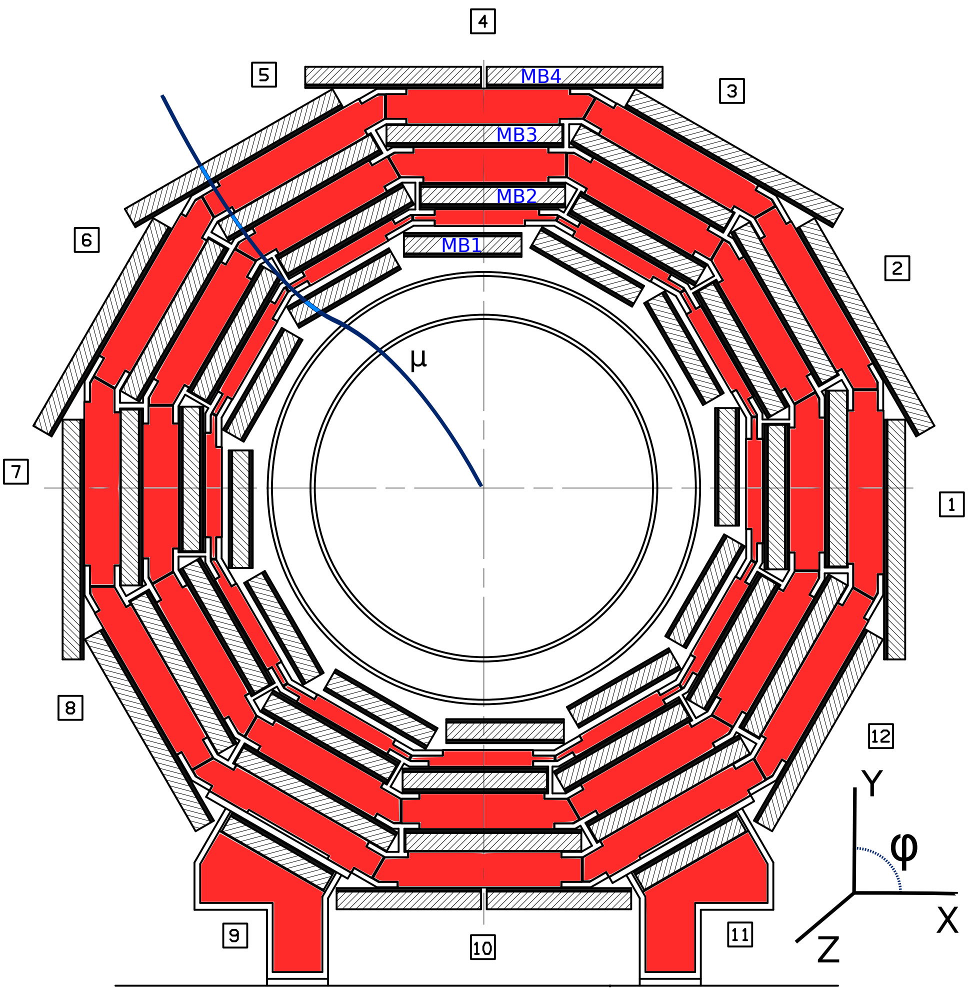

FIGURE 4.1: Transverse view of a CMS wheel of the DT system.

Each cell consists of a central anode wire of 50 μm in diameter with two cathode strips at each side of the cell and a pair of positively-charged strips situated in the upper and lower parts of the cells, as shown in figure 4.3, to modify the shape of the drift lines and improve the linearity of the space-time relationship and the resolution of the cell. The cells are filled with a gas mixture with a composition of 85% Ar and 15% CO_2. The voltages of the anode, cathode and strips, often called high voltage (HV), were kept during most of the RUN 2 in their nominal values, corresponding to V_{wire} = +3600 V, V_{strip} = +1800 V and $V_{cathode}$ = -1800 V. However, from 2017 the standard value for V_{wire} was reduced in several DT chambers in order to decrease the ageing effects, mainly to V_{wire} = +3550 V, as explained in the following sections, while keeping the reconstruction efficiency close to 100%.

The passage of muons through the DT cells causes ionisation in the atoms of the gas. The ionised electrons move through the cell following the drift lines and causing further ionisation, resulting in an avalanche of electrons travelling towards the anode

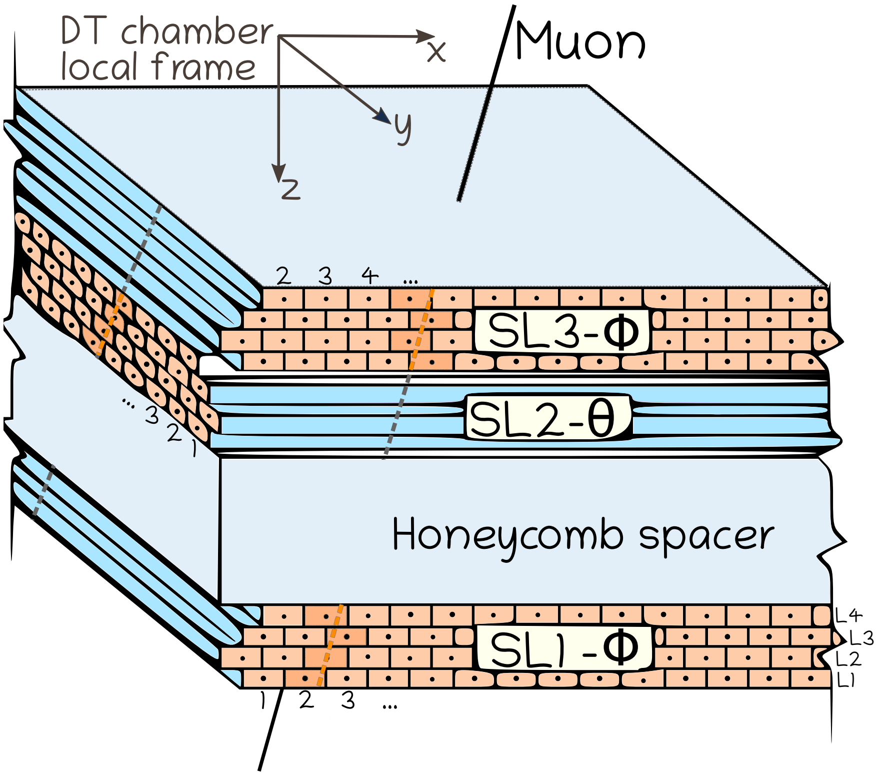

FIGURE 4.2: Layout of a CMS DT station.

wire. At the DT standard working conditions, a gas gain of about 10^5 is reached. The charge is collected in the wire producing a pulse that is read by the front-end (FE) electronics. The signal is amplified at the FE board and compared with a threshold (FEth), with a nominal value of 30 mV. This value was lowered to 20 mV during the 2017 data taking, which increased the efficiency compensating the lowering of the anode HV.

The time that takes the initial pulse to reach the anode is called drift time (t_{drift}). It has a maximum value of about 380 ns (when the pulse is produced close to the cathode plates) and it is related to the position of the muon through the drift velocity (v_{drift}), which has a known and calibrated value for each SL. The mean value of the drift velocity is $v_{\text{drift}} = 55.5\,\mu\text{m} \cdot \text{ns}^{-1}$.

4.4 Longevity studies for the HL-LHC

One of the main challenges of the DT system for the HL-LHC is the ageing of the detector. Under this name, several effects related to the longevity of the electronics and the active components of the detector are included. In this work, I will refer to the longevity effects on the detector due to the continuous operation under an

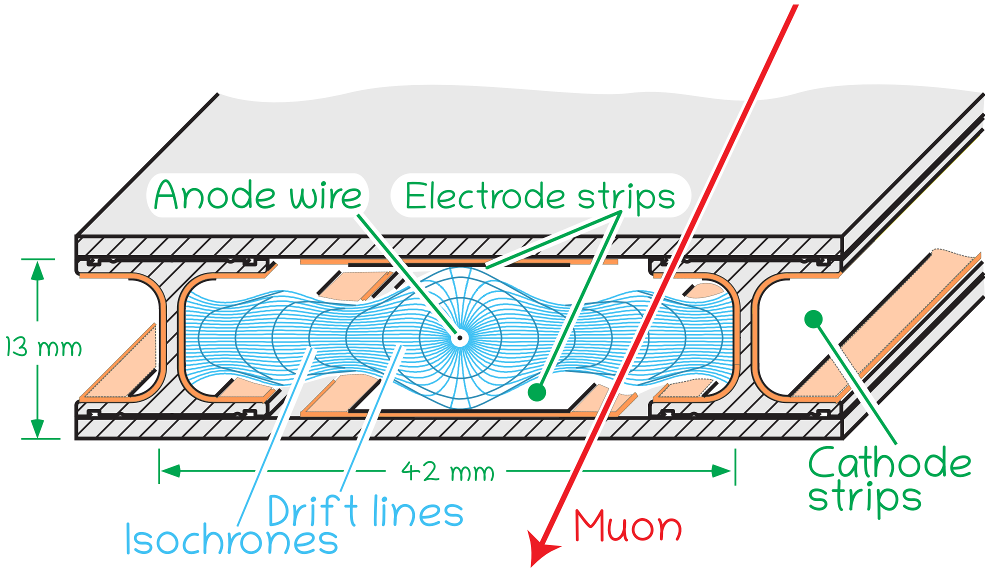

FIGURE 4.3: Layout of a CMS DT cell.

environment with high levels of radiation. This ageing is mainly caused by depositions of outgassing material on the surface of the anode wires of the detector.

Some ageing studies for the phase-2 upgrade were already reported [2], showing a large drop of gain due to the ageing affecting the most irradiated stations and, as a consequence, a decrease of the hit efficiency. However, thanks to the large redundancy of the CMS muon system the performance of the muon reconstruction would remain very high ($\approx$ 98%). Nevertheless, the loss of hit efficiency might compromise the performance of the standalone trigger of the muon system, where the redundancy of the detector is not so high and a decrease of the number of detected hits could affect the trigger efficiency. Further studies, presented in this chapter, were carried out to characterise the ageing of the DT system and find solutions to reduce or mitigate its effects.

4.4.1 The CERN Gamma Irradiation Facility

The CERN Gamma Irradiation Facility (GIF++) [65] is located at the CERN site of Prévessin. An intense source of ^{137}Cs that emits photons of 662 keV is situated inside a bunker with several gaseous detectors in order to test them under different radiation conditions. The source can be attenuated with a set of filters that reduces the photon rate that is received by the detectors. The wide field of the source, as shown in figure 4.4, allows to irradiate a large area at different rates that depend on the distance to the source and the attenuation filters between the source and the detectors. The bunker is divided into two regions, upstream and downstream, each of them with an independent set of attenuation filters. As of March 2016, the source intensity was about 13.5 TBq and was approximately constant during the longevity studies between 2017 and 2019, as the half-life of ^{137}Cs is 30.1 years.

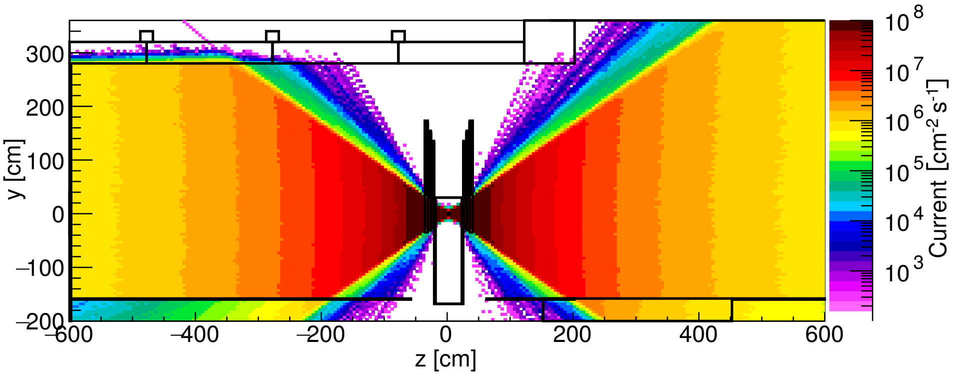

FIGURE 4.4: Distribution of the photon rate at GIF++ at the floor height as a function of the coordinates perpendicular to the vertical axis.

The bunker is constructed around the H4 secondary beam line of the SPS. The SPS provides protons of up to 450 GeV. After colliding with a fixed target, plenty of hadrons are produced. A muon beam, created mostly from pion decays, with an energy of up to 100 GeV, reach the subdetectors at GIF++ and can be used to test their performance. Due to the limited amount of time and resources, the SPS muon beam is available for the subdetectors at GIF++ during a couple of test beam periods of one or two weeks per year.

Radiation tests on a MB1 spare chamber were conducted during 2015 and 2016. The results are published in the phase-2 upgrade muon Technical Design Report [2], showing a large ageing effect on the gain, yielding to a decrease of the hit efficiency of up to 60% for the most irradiated chambers. However, the reported effect would have a limitted effect on the CMS muon reconstruction efficiency, according to the simulations, thanks to the large redundancy of the muon system. These results were obtained after a two-week irradiation period at a high accelerating factor ($\sim$ 100) with respect to the expected dose rate at the HL-LHC.

A new spare MB2 chamber was introduced in the GIF++ bunker in September 2017. This chamber has been irradiated at a low accelerating factor ($\sim$ 10) that was kept approximately constant during the whole irradiation. A huge amount of data were collected during the irradiation, including a constant monitoring of all the parameters, weekly measurements with cosmic muons, and measurements with beam muons among others. The MB2 chamber was situated at about 4 m from the source, in the downstream part of the GIF++ bunker, close to the wall. The chamber was standing in vertical position, with the SL1 facing the source.

In this experiment the SL1 is used to test the ageing effects, while SL2 and SL3 are used to trigger the events and reconstruct the muon segments. The irradiation of the chamber is performed with a high voltage value for the anode (HV) of the wires in SL2 and SL3 in standby (1900 V), so the gas gain is ~ 0. In the SL1, the layers 2 and 3 are also kept in standby while irradiating the chamber and are used as reference layers. The layers 1 and 4 in SL1 are set to HV = 3550 V and are used as test layers.

The data taking is divided into two periods: the first, called era A, started in October 2017 and ended in April 2018, after submitting the chamber to an amount of radiation equivalent to that expected for the full HL-LHC run. After that period, the DT chamber was open and a few wires were extracted for inspection. The era B started at the end of October 2018 and continued until February 2019. During the data taking, several measurements were done along the irradiation of the chamber in order to characterise the ageing as a function of different parameters. Table 4.1 shows the main parameters that were explored, their nominal values and their range of variation. In the next sections, the data taking conditions and the results will be presented.

Parameter	Nominal value	Range of variation
Anode voltage	3600 V, 3550 V (test layers, irradiation)	3200 – 3700 V
Attenuation filter	15 (irradiation) / off (data taking)	15 to infinity (off)
FEth	20 mV, 30 mV	20 to 150 mV
Cathode voltage	1200 V	1100 V to 1300 V
Strip voltage	1800 V	1600 V to 1850 V

TABLE 4.1: Summary of the most important working parameters with their nominal values and range of variation.

4.4.2 Dose measurement and conversion factors

The ^{137}Cs source mimics the background rate in the DT system during the CMS data taking. At CMS, the background radiation is mainly composed by low energy neutrons. This background produces, in the long term, the ageing of the detector, that can be quantified by measuring the amount of integrated charge absorbed by the detector along a period of time. At GIF++ the amount of charge absorbed by the detector is proportional to the radiation dose caused by photons from the source recieved by the chamber. This effect can be quantified with dosimetric measurements. At CMS, the integrated dose received by any of the DT stations is proportional to the integrated luminosity along the time. A conversion factor between these two quantities is derived to extrapolate from the integrated dose at GIF++ to the expected integrated luminosity at CMS.

Furthermore, the effect of the background rate also affects the performance of the detector. The muon hit efficiency is degraded by the presence of a background of particles that can affect the signal collected by the anode wires or introduce background noise to the measurements. The effect of the background rate at GIF++ is proportional to the photon dose rate from the source, that can be measured with a dosimeter. For the CMS DT system, the amount of background rate for each DT station depends on the instantaneous luminosity given by the LHC. Another conversion factor to relate these two quantities at GIF++ and CMS DT system is derived.

At GIF++, the dose rate is continuously measured by a REMUS dosimeter (a CERN dosimeter for radiation and environment monitoring unified supervision) situated in the internal wall of the bunker, next to the MB2 station. The photon dose rate of the ^{137}Cs source collected by the dosimeter depends on the attenuation filters that are set at any moment and on the amount of material (e.g. detectors or cranes) situated between the source and the dosimeter. The dose rate measurement given by the REMUS is extrapolated to the dose rate at the surface of the MB2 station using a portable dosimeter: several measurements are taken with the portable dosimeter at 9 different positions in the surface of the MB2 chamber and at the REMUS position. The dose rate given by the REMUS is extrapolated to match the average of the measurements with the portable dosimeter on the MB2 chamber surface. The extrapolating factor is re-calculated by performing the nine measurements again each time that a significant change of materials between the source and the MB2 chamber is done inside the bunker.

For all the results presented in this thesis, the dose rate measurements correspond to the REMUS measurement corrected by the extrapolating factor obtained with the exposed method. The integrated dose is calculated by integrating this corrected dose rate for a period of time. The background rate at GIF++ is compared with the one at CMS, taking as a reference the MB1 stations in wheels ± 2, that are the DT chambers with the highest background rate.

The presence of such a radiation background produces a current in the DT cells that is collected by the anode wire and measured by the electronics of each DT station. The currents are measured in the CMS DT chambers as a function of the LHC instantaneous luminosity, showing a lineal behaviour. The currents are also measured at GIF++ for different source attenuation filters (i.e. different dose rates) and a lineal relation for low dose rates ($< 0.1\,\mathrm{mGy\,h^{-1}}$) is also observed. The conversion factor between instantaneous luminosity and dose rate is taken as the ratio between the slopes of the linear fits of the measured curves:

- Currents vs LHC instantaneous luminosity at CMS for the MB1 chambers in wheels ±2.
- Currents vs dose rate at GIF++

A conversion factor of $10^{34}\,\mathrm{cm^{-1}\,s^{-1}} = 0.0109\,\mathrm{mGy\,h^{-1}}$ is obtained with this method, which is valid at low dose ($< 0.1\,\mathrm{mGy\,h^{-1}}$), where a linear relation is observed.

However, the MB2 at GIF++ was aged at a high dose rate (an accelerating factor of 10 with respect to the expected ageing at the HL-LHC). The linearity of the relation between the currents and the dose rate is lost at such high values of the dose rate. The non-linear behaviour was measured and a conversion factor of $1\,\mathrm{fb^{-1}} = 0.42\,\mathrm{mGy}$ was obtained to convert the integrated luminosity of a CMS MB1 chamber in wheels ±2 to the integrated dose of the MB2 station at GIF++ that is irradiated with an accelerating factor of 10.

The integrated dose collected by the MB2 chamber at GIF++ and its equivalent HL-LHC integrated luminosity for a MB1 chamber of the CMS DT system in wheels ±2 is shown in figure 4.5.

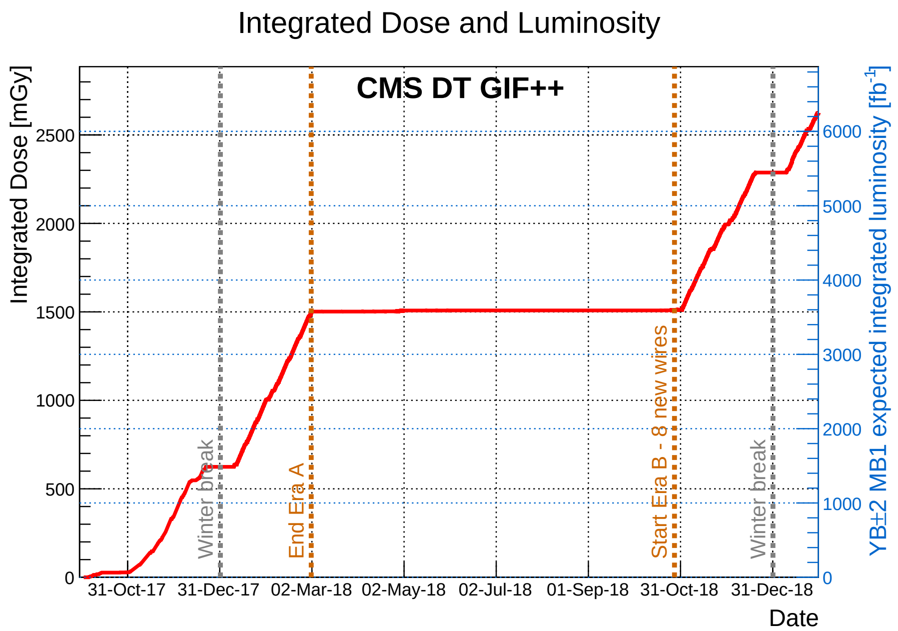

FIGURE 4.5: Integrated dose (mGy) as a function of time for the full irradiation period of the CMS MB2 spare chamber at GIF++. The vertical grey lines correspond to the 2017 and 2018 winter breaks when the chamber is kept off and the vertical orange lines mark the two irradiation and data-taking eras. The axis on the right shows the equivalent expected luminosity for MB1 chambers in the external wheels for the HL-LHC.

4.4.3 Trigger for cosmic and beam muons

During the irradiation period, most of the measurements were done using cosmic muons. For the data taking a DT internal trigger (DT autotrigger) is used. This trigger takes muon hits in both projections using SL2 and SL3 to reconstruct a muon segment. Using this trigger avoids introducing any bias on the SL1. On the other hand, muon events coming from a muon beam are triggered using external scintillators.

During the first months of the irradiation period, in order to avoid irradiation the reference layers (2 and 3 in SL1), some measurements of background rates were taken with the layers 1 and 4 in SL1 on and the rest of the chamber in standby. To trigger the data taken, random triggers were used, with a frequency of 100 Hz.

The MB2 chamber is standing vertical in the GIF++ bunker, so most of the cosmic muons, coming from the atmosphere go through the chamber with an incidence angle θ with respect to the horizontal plane far from zero, as shown in figure 4.6 (left). For a muon beam, the incidence of the muons is perpendicular to the surface of the chamber and the beam illuminates a small region in the centre of the chamber, as shown in figure 4.6 (right).

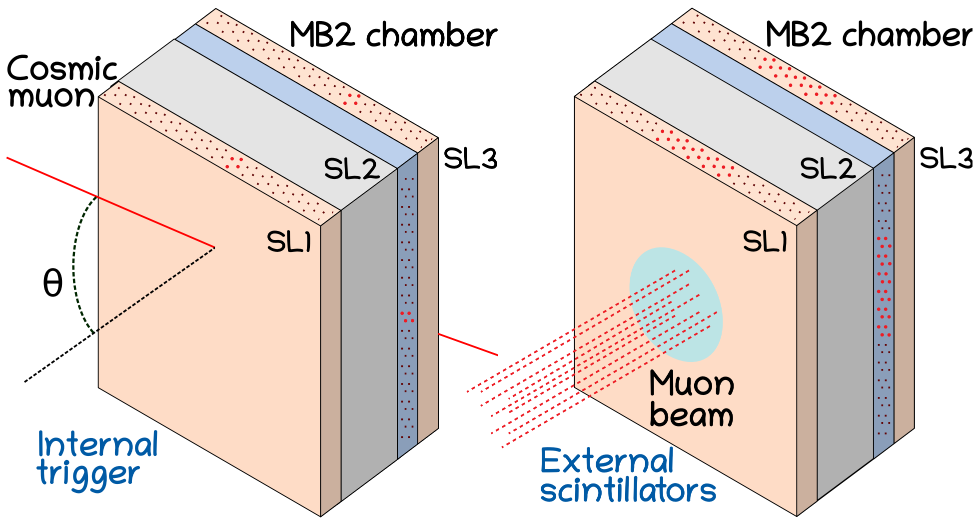

FIGURE 4.6: Schematic layout of the data taking with the spare MB2 chamber at GIF++ for cosmic muons (left) and muon beam (right).

The θ distribution for reconstructed cosmic and beam muons is shown in figure 4.7, for runs taken with nominal HV conditions and source off. These runs were taken at the beginning of the irradiation period. The incidence angle with respect to the horizontal plane also determines the path length of the muon inside a chamber in the

Φ superlayers, which increases as $1/\cos\theta$, obtaining a higher signal for larger muon path lengths.

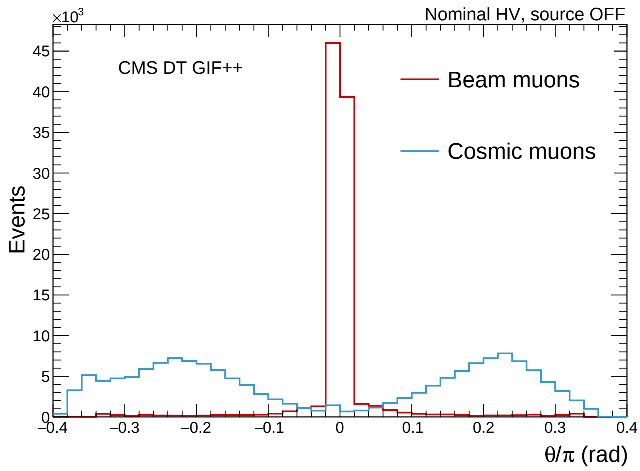

FIGURE 4.7: Distribution of the angle of incidence θ of reconstructed segments for a cosmic muon run and a beam muon run.

The reconstruction algorithm is the same for cosmic and beam muons. The segments are reconstructed with information from the 12 layers and a hit is assigned to the segment for each layer in which a compatible hit is found. The number of hits for reconstructed segments in a cosmic and a beam run is shown in figure 4.8 (left). The distribution of the hits associated to the segments in the different cells of layers 1 and 4 in SL1 are shown in figure 4.8 (right) in a cosmic and a beam run. This distribution is flat for cosmic muons, as they illuminate the whole chamber with equal probability, but it is restricted to a few cells for the beam muons. The runs were taken with nominal HV conditions, source off and during the first days of the irradiation period.

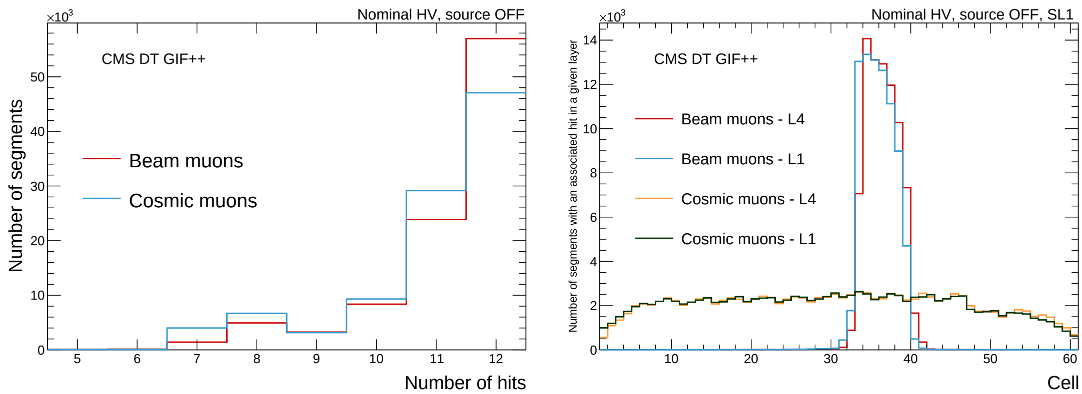

FIGURE 4.8: Distribution of the number of associated hits per reconstructed segment (left) and associated hits as a function of the cell for layers 1 and 4 in SL1. The distributions are shown for a cosmic muon run and a beam muon run.

4.4.4 Measurements of the hit efficiency

The efficiency is measured per layer, for any of the layers in SL1, using reconstructed segments with four associated hits in SL3 and at least one associated hit in SL1 in a layer different from that for which the efficiency is measured. To avoid introducing any bias in the measurement of the efficiency, the segment is extrapolated from SL3 to the test layer in SL1 and the layer is considered efficient if a hit is found in the expected cell position, taken from the extrapolation. To consider that the hit is associated to the muon, its measured position must be at a distance closer than 2 mm to the expected position. The efficiency for a given layer is computed as the ratio between the number of times that a layer is found to be efficient and the total number of reconstructed segments. A layout of the measurement of the hit efficiency is shown in figure 4.9.

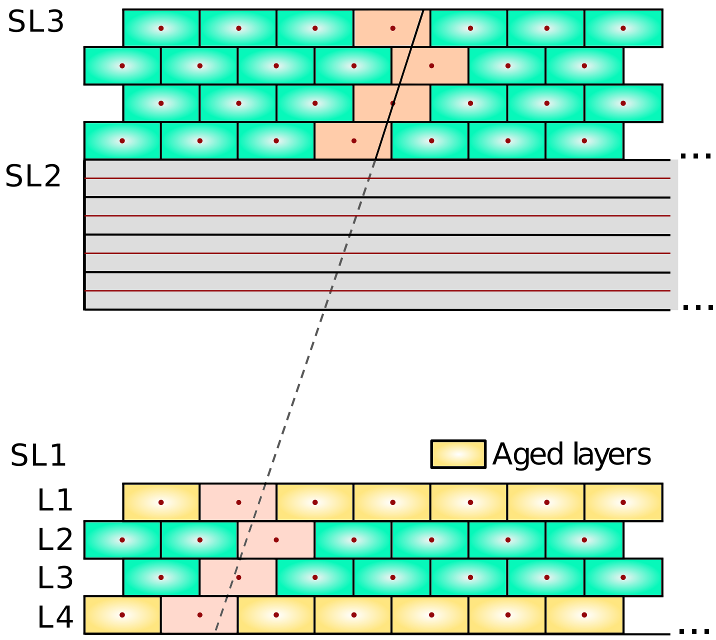

FIGURE 4.9: Layout of the measurement of the hit efficiency at GIF++ for any layer in SL1. The SL3 is used as reference and the reconstructed segment is extrapolated to the test layer in SL1.

The hit efficiency was measured periodically during the irradiation of the chamber, under different working conditions, in the aged layers, while the non-aged layers in SL1 (2 and 3) are used as reference. The segment reconstruction efficiency was also measured. To perform these measurements, the same segment selection is applied but the layers are considered efficient if a hit is found in the expected cell position and the hit is associated to the reconstructed segment.

In figure 4.10 the efficiencies as a function of the cell for layer in SL1 and the position within the cell are shown, for a cosmic run and a beam run that were taken at the beginning of the irradiation period, with source off and nominal HV settings.

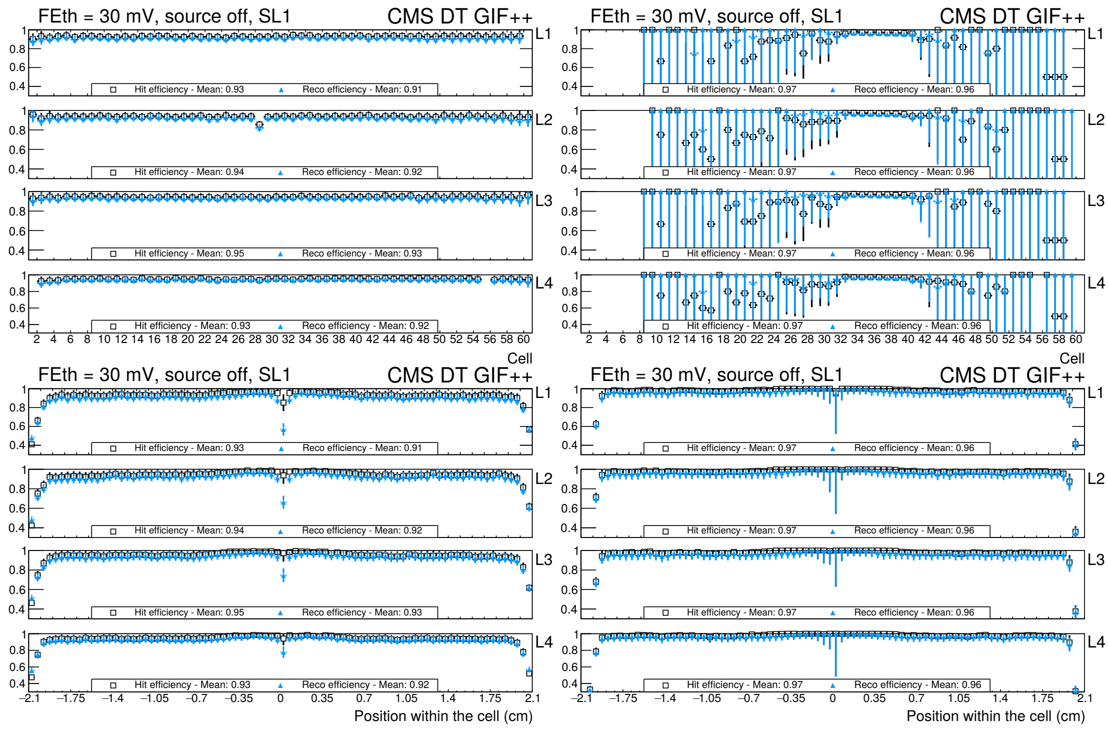

FIGURE 4.10: Efficiency distribution as a function of the cell (upper) and position within the cell (lower) for cosmic muons (left) and beam muons (right) for runs taken at the beginning of the irradiation period.

The efficiency is measured as a function of the anode HV of a test layer (HV scan). The efficiency reaches a plateau with values above 90% for a HV value of about 3550 V and goes to zero for lower HV values, down to about 3200 V. The ageing effects on the test layers are expected to modify the values of the curve, showing large efficiency drops for HV values outside the plateau region. In figure 4.11 the efficiency as a function of the anode HV for L1 and L4 layers in SL1 for a couple of scans (cosmics and beam) are shown. The scans were taken at the beginning of the irradiation period, with FEth $= 30$ mV and source off.

In figure 4.12, the hit efficiency as a function of the position within the cell are shown, for a cosmic run and a beam run that were taken at the beginning of the irradiation period, with source off and two different values of HV.

4.4.5 Measurements of the background rate

Each event recorded with the MB2 at GIF++ stores the collected signal in a time window of 2800 *ns*. When a muon triggers the data taking (either beam muons or cosmic

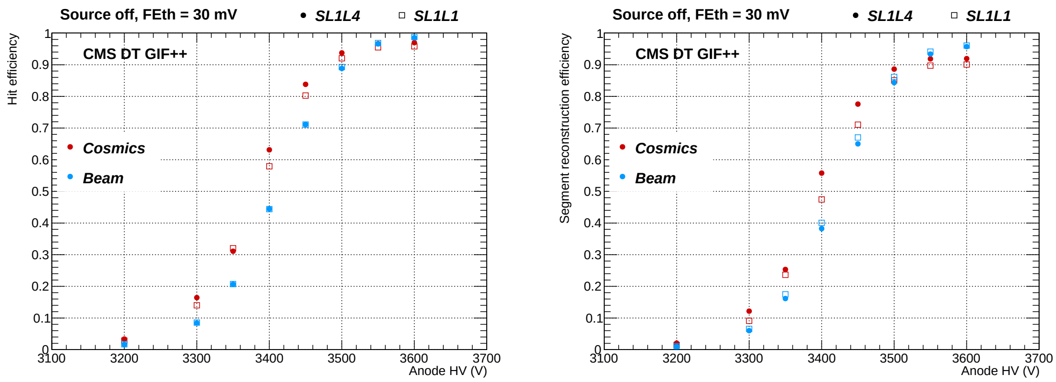

FIGURE 4.11: Hit (left) and segment reconstruction (right) efficiencies of layers 1 and 4 in SL1 as a function of the anode voltage for cosmic and beam muon runs taken at the beginning of the irradiation period.

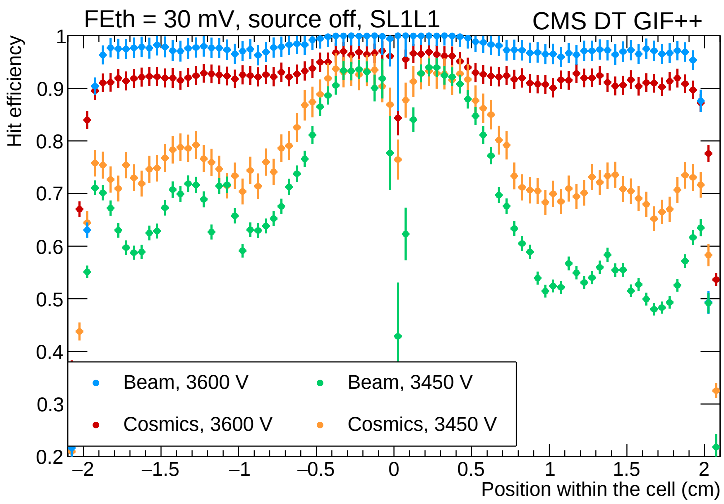

FIGURE 4.12: Hit efficiency as a function of the position within the cell for a beam run and a cosmic run taken with source off. The efficiencies have been measured in layer 1 in SL1 for two different HV values: 3600 V (nominal) and 3450 V.

muons), all the signal pulses (digis) that are produced at least 1 μs before the first-collected digi from a muon hit is measured, are collected. As a consequence, the time mismatch between the start of the data taking and the trigger time (ttrig) is always larger than 1 μs and a background region can be defined at $t < 1\,\mu$s.

On the other hand, the signal hits are distributed in a time interval of 380 ns, corresponding to the maximum drift velocity within a cell. The distribution of the number of signal hits as a function of time is called a timebox and can be seen in figure 4.13 for the different layers, using a cosmic and a beam run collected at the beginning of the irradiation period with nominal HV settings and source off.

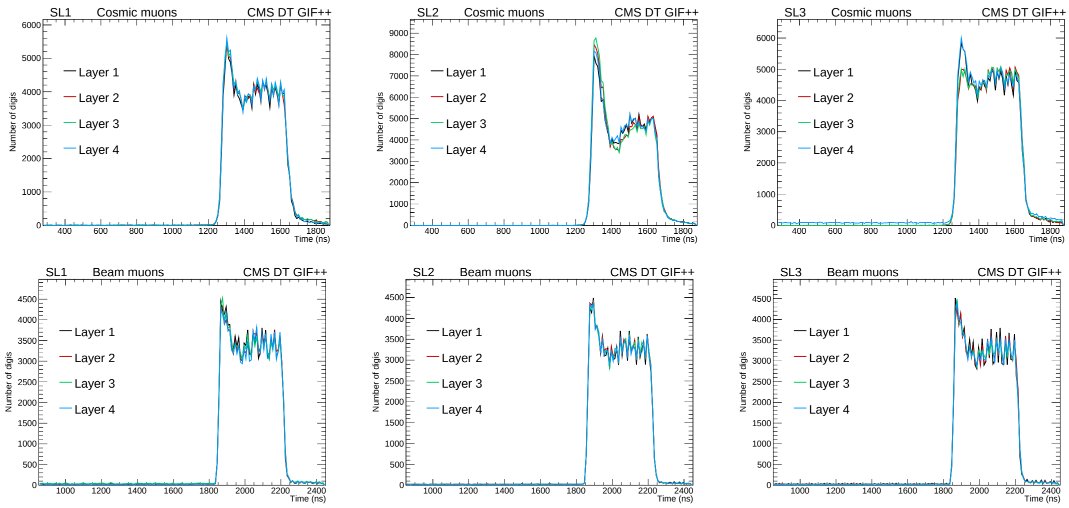

FIGURE 4.13: Time distribution of the digis in each layer for a cosmic run (upper) and beam run (lower) taken at the beginning of the irradiation period with source off. The timebox, with a width of about 380 ns, can be observed.

The number of detected digis per second in a given run is called the rate. The measured rates are small for clean runs with source off but increase with the source on. The evolution of the rates with the integrated dose in the test layers, for a given source rate, is one of the observables used to characterise the ageing. In figure 4.14 the distribution of rates as a function of the cells for a cosmic and a beam run with nominal HV conditions and source off are shown. In figure 4.15 the rates as a function of the cell are shown for background ($t < 1\,\mu$s) and background+signal for layer 1 in SL1, for two beam runs, one of them using scintillators as trigger and source off and another taken with random trigger and source on, using an attenuation filter that produces a background rate in the MB2 chamber equivalent to that expected in a MB1 chamber of wheel ± 2 during the HL-LHC. All the runs have been taken at the beginning of the irradiation period, before the chamber have received any significant radiation.

4.4.6 Operation of the spare MB2 DT chamber

The data taking was planned in a weekly basis. Each Wednesday, the source is turned off and the GIF++ bunker is open for maintenance. A HV scan was taken on layers 1 and 4 in SL1 almost every week during the irradiation period. Also, other measurements with no source were done on Wednesdays such as HV scans on non-aged layers or other scans.

Every Thursday, several measurements were taken using a random trigger to test the evolution of the rate measurements with the ageing of layers 1 and 4. Several scans

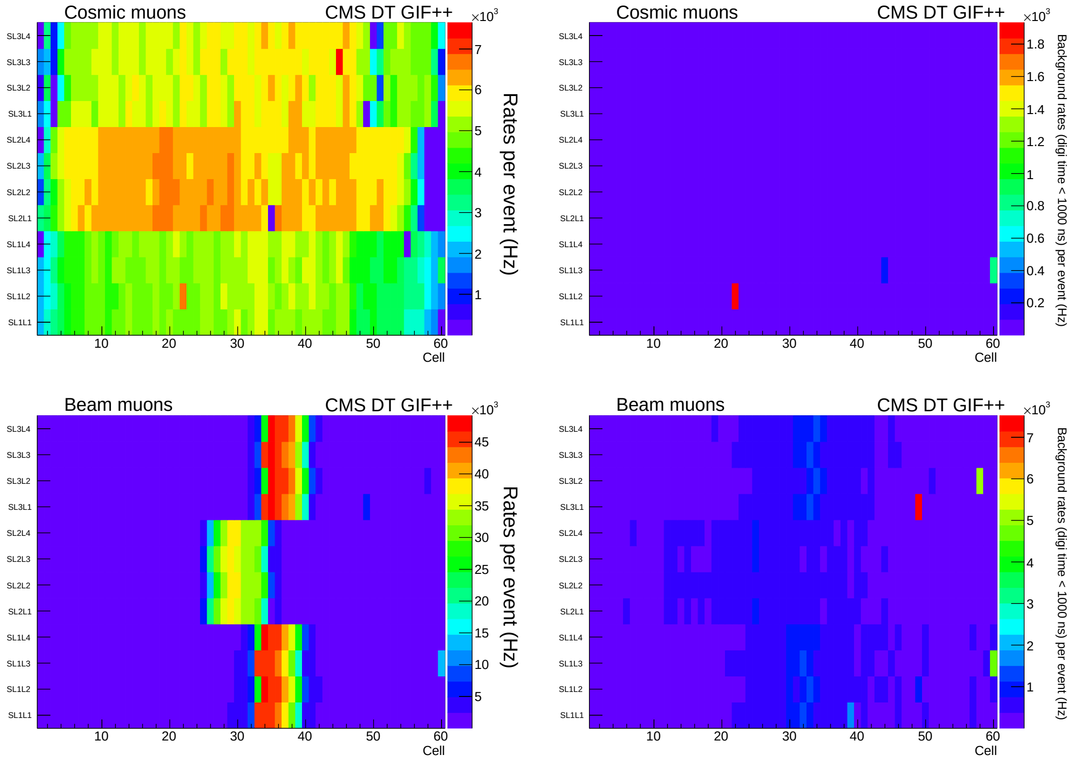

FIGURE 4.14: Rates in each cell for a cosmic (upper) and a beam (lower) run with nominal HV conditions and source off for signal (left) and background (right).

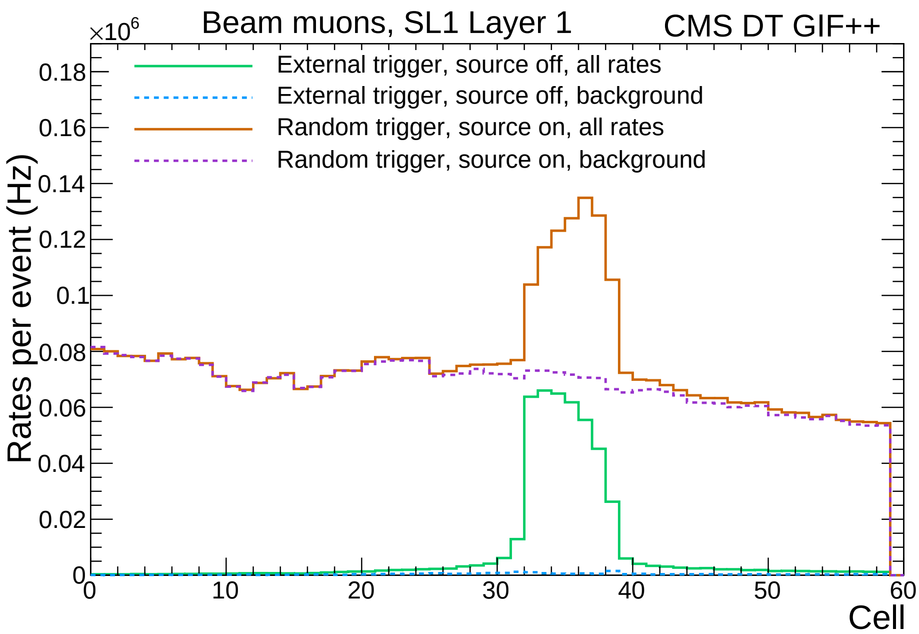

FIGURE 4.15: Rates per event as a function of the cell for two runs with beam muons: one of them taken with external trigger (scintillators) and no source and the other one taken with random trigger and source on.

were performed: FEth scans by varying the FEth value from 20 mV up to 150 mV and source scans by changing the configurations of the downstream filters of the source, decreasing the attenuation from a factor ~ 1000 down to a factor ~ 15.

During the rest of the week, the chamber was kept with the standby HV values except of the two ageing layers (1 and 4 in SL1) that were kept at a HV of 3550 V. The layers were irradiated with attenuations of 69, 46, 33, and 22 during the first weeks, and a filter 15 was kept during the rest of the irradiation period, corresponding to an accelerating factor of about 10 with respect to the expected ageing at the HL-LHC. To avoid ageing the reference layers in SL1 and the rest of the chamber, the FEth and source scans were mostly taken with the chamber in standby except for the test layers, at an anode voltage of 3550 V, using random triggers.

The atmospheric conditions inside and outside the bunker and the currents measured in each layer of the chamber were continuously monitored. The fluctuations of the atmospheric conditions produce variations of the response of the chamber and are propagated to the hit efficiency.

During the data taking several test beams were fed into the installation, providing the opportunity to measure efficiencies with different conditions using beam muons. The so-called era A of the data taking comprises about 18 weeks from October 2017 to April 2018, with a winter break when the chamber and the source were switched off. The chamber absorbed a radiation dose equivalent to about the expected accumulated radiation during the full HL-LHC for a MB1 chamber in wheel ± 2. After this period, several wires were extracted for inspection: 4 wires in the layer 4 in SL1 were removed from the chamber and 8 wires in layer 1 in SL1 were extracted, 7 of which were replaced by new wires. From the end of October 2018, a new irradiation period started, called era B, comprising 14 weeks until the end of February 2019. After this period, the chamber absorbed a total radiation dose equivalent to $2 \times$ HL-LHC.

4.4.6.1 Data taking in era A

The era A started in October 2017 with a test beam in which the chamber was characterised before being irradiated. After this test beam, the source was turned on with decreasing attenuations during the first weeks, keeping an attenuation of 15 from the fifth week, corresponding to about 10 times the expected background radiation at the HL-LHC in a MB1 chamber of CMS in the wheels ± 2. After this irradiation period, a total dose of 1.5 Gy, equivalent to about 3600 fb^{-1} at the HL-LHC for the most irradiated chambers. The evolution of the atmospheric conditions during this period is shown in figure 4.16.

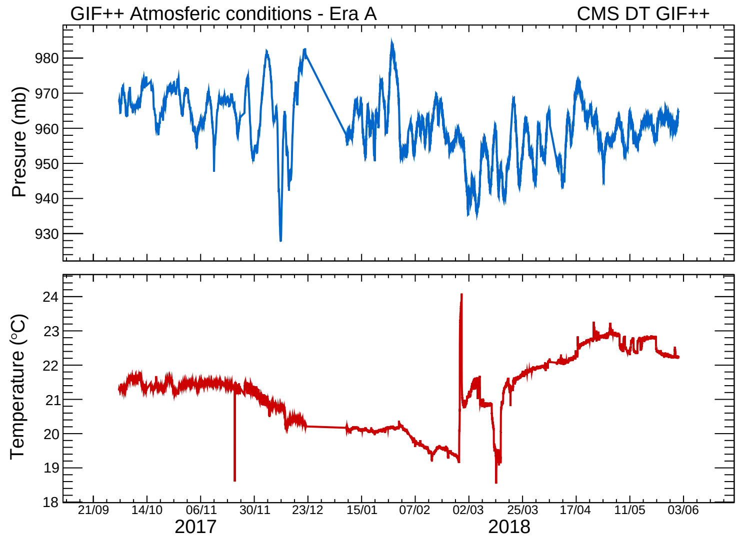

FIGURE 4.16: Evolution of the temperature and the pressure during the era A. The GIF++ monitoring were off during the winter break (from 22 December to 8 January).

On Thursdays, the source was on and the MB2 chamber was kept in standby except for the two test layers, at a HV of 3550 V. Source scans were done using a random trigger with a rate of 100 Hz. Also, keeping a source rate close to the equivalent expected background rate at the HL-LHC, FEth scans have been taken, measuring the rates in the test layers using random triggers.

In figure 4.17 some of the HV scans taken during era A are shown. The hit efficiencies of layers 1 and 4 in SL1 are shown. Each scan was taken at a different week, corresponding to a different accumulated dose. The equivalent expected integrated luminosity at the HL-LHC for each scan is shown in the legend. A drop of efficiency is observed in the HV scans with higher accumulated radiation for HV lower than 3600 V, while the efficiency remains about the same, above 90%, for HV = 3600 V. The scans were taken with a front-end threshold of 30 mV.

In figure 4.18 four FEth scans are shown for layers 1 and 4 in SL1. In these scans the measured rates are shown as a function of the FEth scan for a background rate equivalent to about $30 \times 10^{34}\,\mathrm{cm}^{-1}\,\mathrm{s}^{-1}$ for the most irradiated CMS station at the HL-LHC. The data were taken using random triggers. As expected, the rates decrease with the FEth, showing that at a higher threshold the collected signal, mainly from electrons induced by the source, is smaller. The evolution with the integrated dose reflects an ageing effect: the rates at an integrated luminosity equivalent to the expected after the HL-LHC run are about half the collected rates with the chamber with a low integrated dose (equivalent to about $180\,\mathrm{fb}^{-1}$ at the HL-LHC).

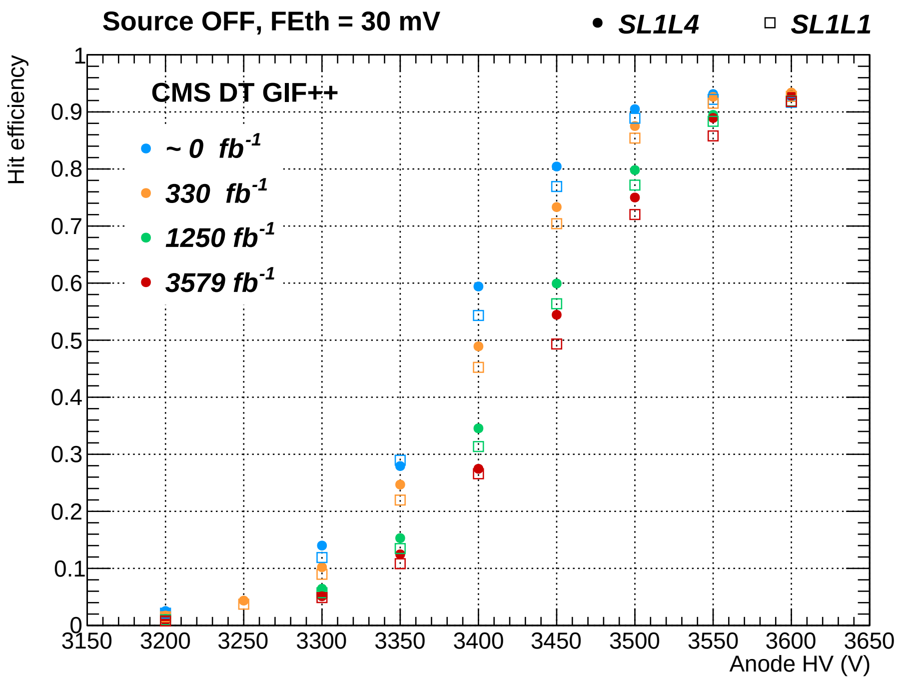

FIGURE 4.17: Hit efficiency as a function of the anode HV for layers 1 and 4 in SL1 for different absorbed radiation, corresponding to different expected integrated luminosities at the HL-LHC for the most irradiated DT stations.

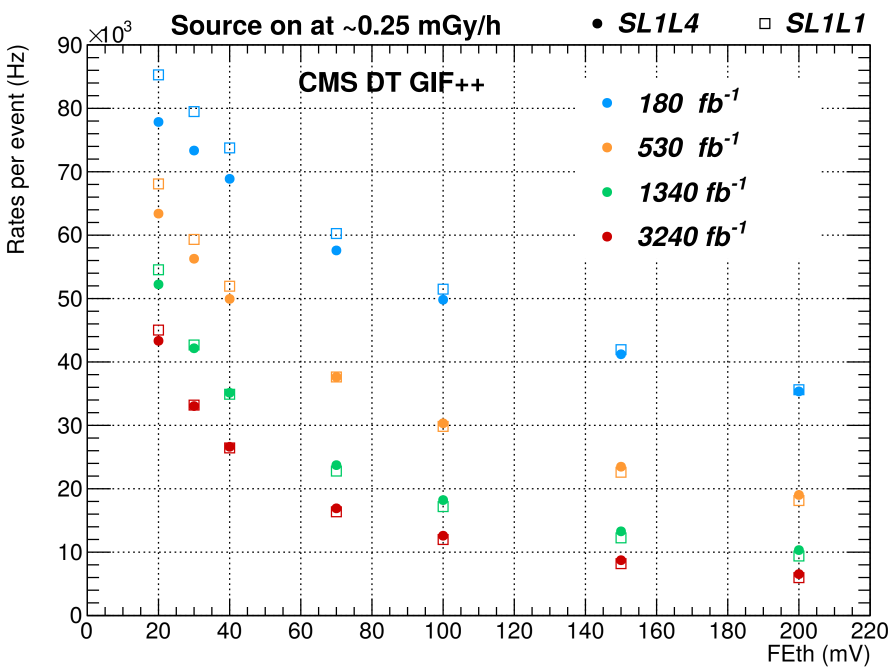

FIGURE 4.18: Rates per event as a function of the FEth for layers 1 and 4 in SL1 for different absorbed radiation, corresponding to different expected integrated luminosities at the HL-LHC for the most irradiated DT stations.

Finally, in figure 4.19 four source scans are shown for layers 1 and 4 in SL1. The rates per event are measured using random triggers for different background rates, equivalent to different instantaneous luminosities at the HL-LHC. An approximate linear relation is found up to instantaneous luminosity values of $\sim 30 \times 10^{34}\,\mathrm{cm}^{-1}\,\mathrm{s}^{-1}$. The slope decreases significantly with the absorbed dose due to ageing effects.

The currents have been also measured for the same source scans. A linear relation is also observed between the currents and the source rate, with a decreasing slope for higher accumulated radiation. The results are shown in figure 4.20.

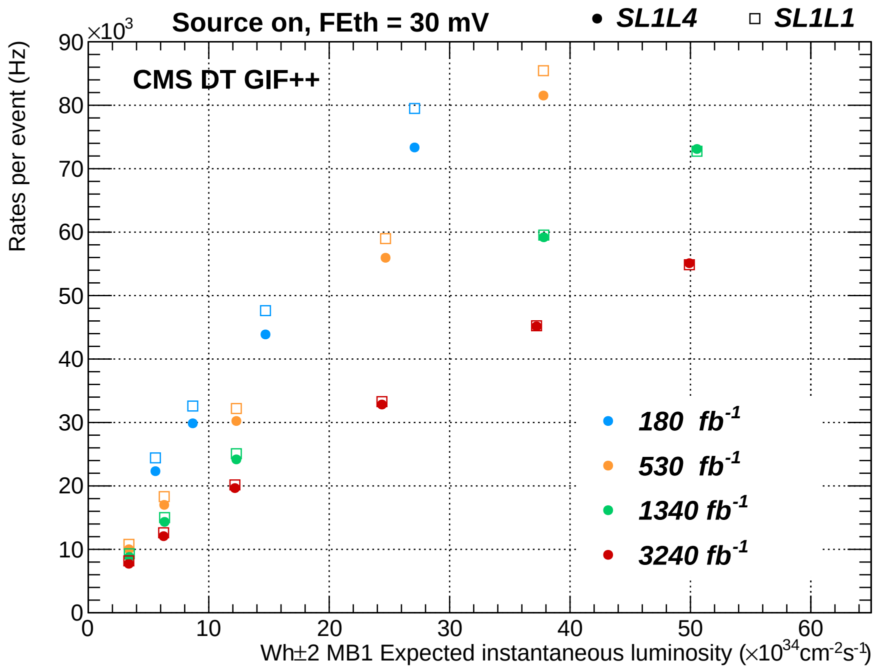

FIGURE 4.19: Rates per event as a function of the HL-LHC equivalent instantaneous luminosities for layers 1 and 4 in SL1 for different absorbed radiation, corresponding to different expected integrated luminosities at the HL-LHC for the most irradiated DT stations.

At the end of era A, a test beam has been done in which the efficiencies were measured and compared with the efficiencies at the beginning of the irradiation period. In figure 4.21 two HV scans are compared, taken at the begining of the irradiation period and after the aged layers have received an amount of radiation equivalent to about $3600\,\mathrm{fb}^{-1}$. In this figure, the loss of efficiency due to the effect of the ageing caused by the irradiation of the chamber is observed for different HV of the anode for layers 1 and 4 in SL1. The data were taken with source off and a FEth of 30 mV.

Furthermore, the efficiency has been measured as a function of the anode HV for different HV values of the cathode and the strip. The efficiencies were measured

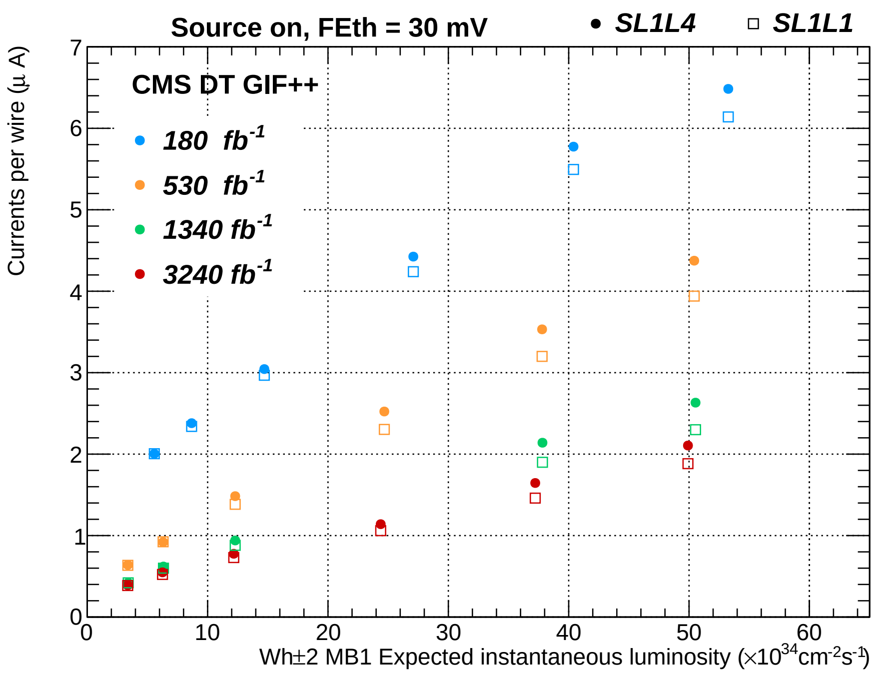

FIGURE 4.20: Currents per wire as a function of the HL-LHC equivalent instantaneous luminosities for layers 1 and 4 in SL1 for different absorbed radiation, corresponding to different expected integrated luminosities at the HL-LHC for the most irradiated DT stations.

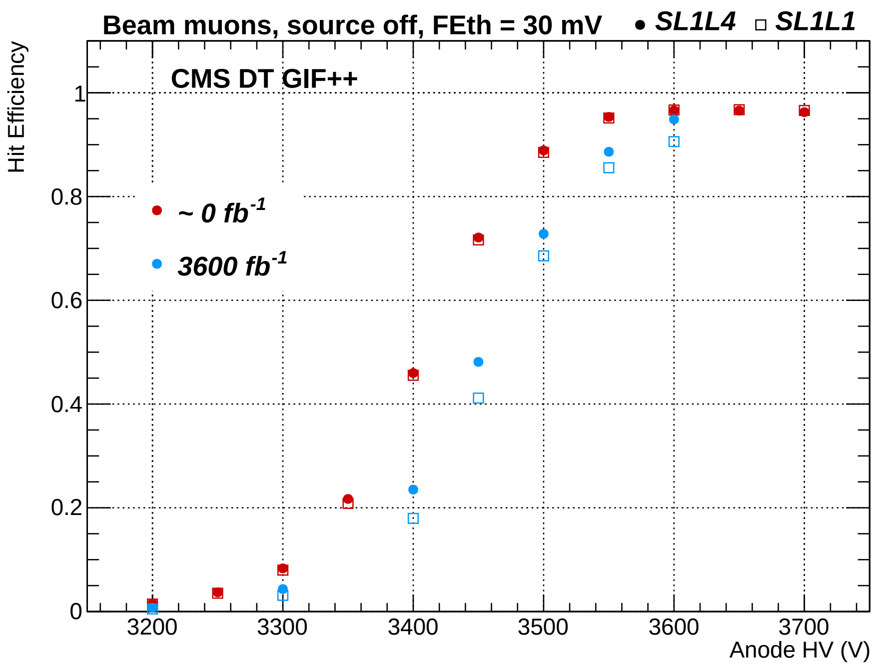

FIGURE 4.21: Hit efficiency as a function of the anode HV for test beam runs taken at the beginning and at the end of era A, for layers 1 and 4 in SL1. The runs were taken with source off and a FEth value of 30 mV.

using the muon beam with a FEth of 20 mV and source off. Efficiencies for a non-aged layer (SL1L3) and a test layer (SL1L4) are compared. The results are shown in figure 4.22. The efficiency loss on the aged layers is observed for the different cathode and strip voltages. The hit efficiency has a small dependency on the cathode voltage. On the other hand, a strong dependency of the hit efficiency is observed with the strip voltage, but the effect of the ageing in layer 4 is similar for the three strip voltages.

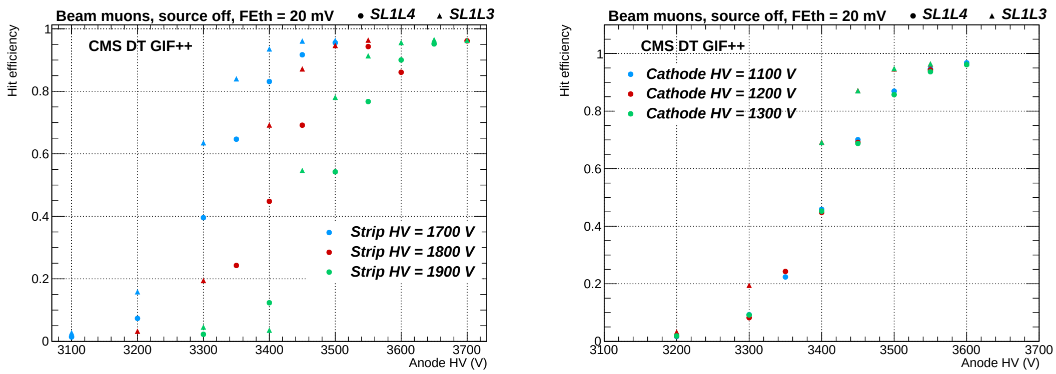

FIGURE 4.22: Hit efficiency as a function of the anode HV for different voltage values of the strips (left) and the cathode (right) for layers 3 and 4 in SL1, using beam muons and source off. The runs were taken at the end of era A, with an integrated dose equivalent to about 3600 fb^{-1} of expected luminosity at the HL-LHC.

4.4.6.2 Data taking in era B

The era B started with a short test beam at the end of October 2018. After that, the MB2 continued to be irradiated with a filter 15, the same used for most of the time during era A. The evolution of the atmospheric conditions during this period is shown in figure 4.23.

After the end of era A, the MB2 chamber was taken out off the bunker and open to extract some of the irradiated wires for further inspection. Four wires were removed from layer 4 in SL1 (wires 37, 38, 39 and 40). Eight wires were removed from layer 1 in SL1, but seven of them were replaced with new wires (33, 34, 35, 36, 37, 38, 39), leaving a hole in the place of wire 40. In figure 4.24 the efficiency as a function of the cell is shown for a run taken with cosmic muons at the beginning of era B, with the source off and a FEth values of 20 mV and 30 mV, with a HV of 3450 V in layer 1 in SL1 and 3600 V in the rest of the chamber, showing a higher efficiency for the new wires in layer 1 in SL1 and the holes where the wires were removed.

During the era B most of the measurements were taken with FEth = 20 mV, as it has been agreed that this value will be used during the HL-LHC. Moreover, several HV

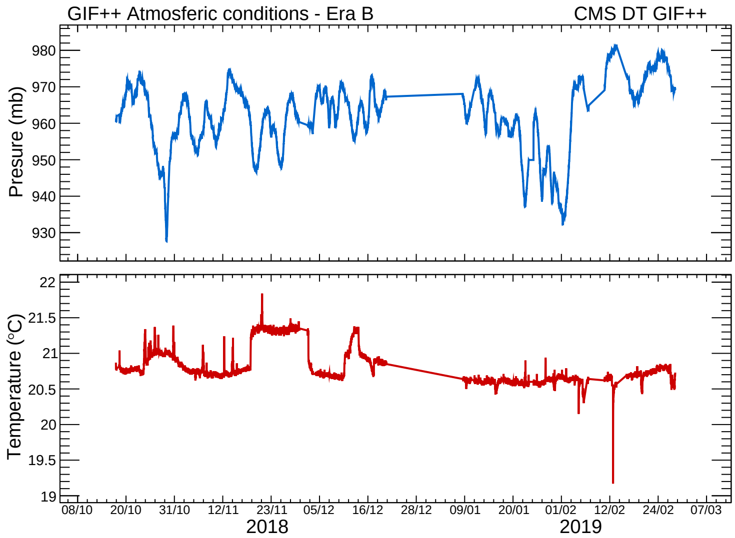

FIGURE 4.23: Evolution of the temperature and the pressure during the era B. The GIF++ monitoring were off during the winter break (from 20 December to 9 January).

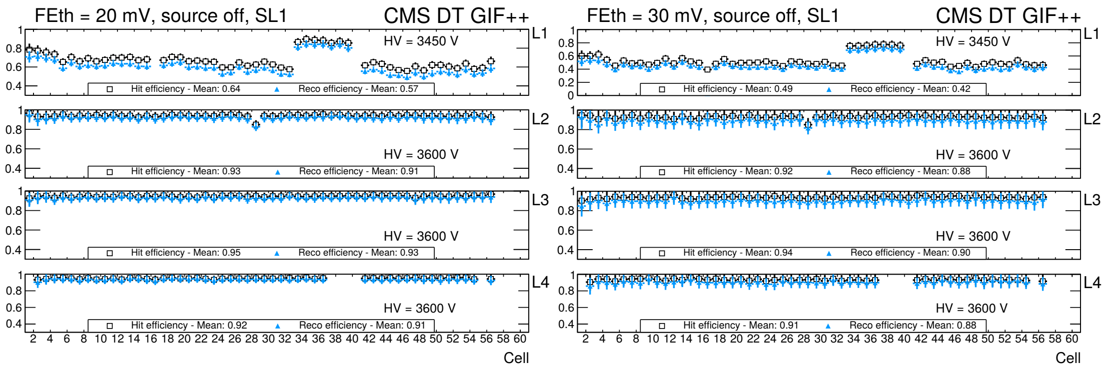

FIGURE 4.24: Efficiency distribution as a function of the cell for runs taken at the beginning of era B with a HV of 3450 V in layer 1 in SL1 and 3600 V in the rest of the chamber, with a FEth of 20 mV (left) and 30 mV (right) and source off.

scans and other measurements using cosmics or beam muons have been done with the source on, so the effect of the expected background rate at the HL-LHC could be tested. The efficiencies measured in the new wires in layer 1 in SL1 can be now used as a reference. Also, HV scans and other measurements using the non-aged layers (SL1L2, SL1L3) have been taken.

The hit efficiency for a FEth of 20 mV is higher than for 30 mV, as shown in figure 4.25. The ageing effects are also less pronounced for hit efficiencies with FEth = 20 mV.

Finally, a comparison of the hit efficiency as a function of the anode HV for different background rates, including a background rate of 0 (with the source off) and about twice the equivalent to the expected background rate at the HL-LHC is shown in figure 4.26. A strong drop of efficiency is shown with a background rate close to the

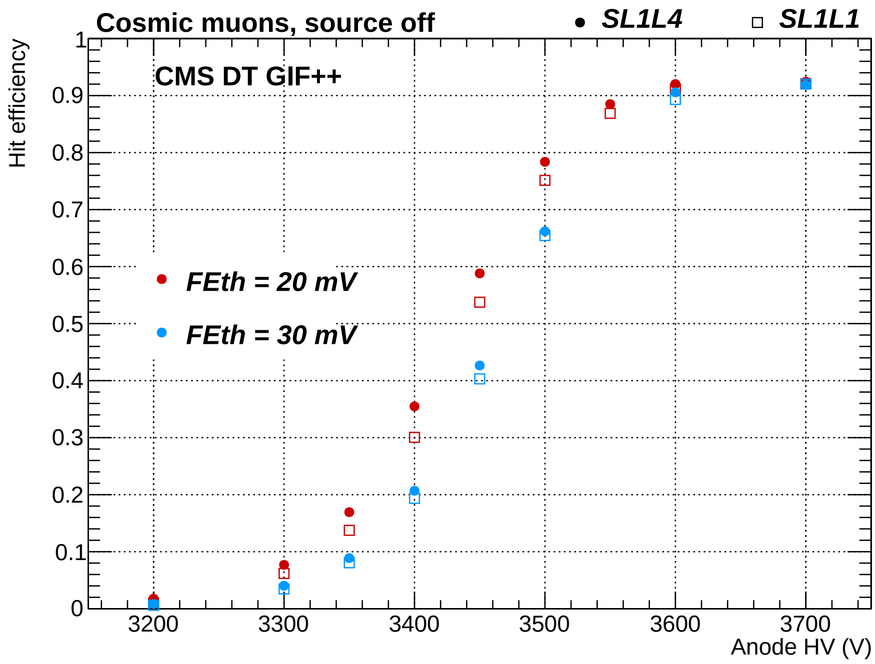

FIGURE 4.25: Hit efficiency as a function of the anode HV for two runs with cosmic muons and source off, for layers 1 and 4 in SL1, with a FEth value of 20 mV and 30 mV.

expected background at the HL-LHC for the aged wires of layer 1. The comparison also shows the efficiency for the non-aged wires of layer 1 (new wires) and layer 2.

4.5 Evolution of the hit efficiency with the ageing

After the end of the irradiation period, a total accumulated dose equivalent to about twice the expected integrated luminosity at the end of the HL-LHC for the most irradiated DT chambers has been reached. Three different HV scans for layers 1 and 4 of SL1 are shown in figure 4.27. These scans were taken at the beginning, middle and end of the irradiation period. An efficiency drop with the accumulated dose is observed as a function of the anode HV. The data were taken at a FEth value of 30 mV and source off.

The evolution of the hit efficiency with the accumulated radiation has been measured with cosmic muons at a HV value of 3550 V for the two aged layers, with source off and FEth = 30 mV, shown in figure 4.28. A moderate efficiency loss is observed in both aged layers of up to 15% for an accumulated irradiation equivalent to about twice the expected integrated luminosity at the HL-LHC.

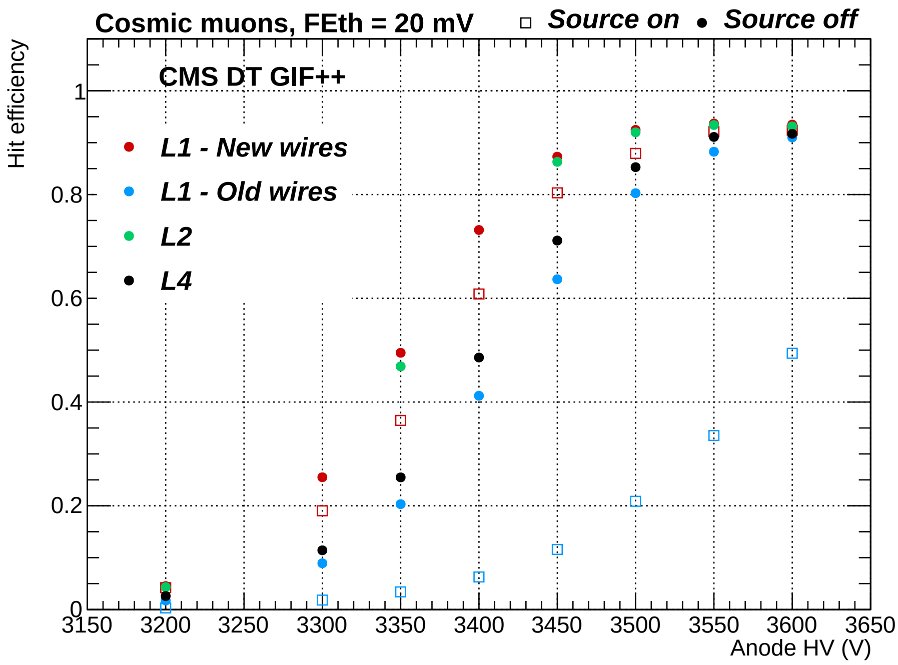

FIGURE 4.26: Hit efficiency as a function of the anode HV for runs with a background rate equivalent to about twice the expected background rate at the HL-LHC for the most exposed chambers (source on) and runs with zero background rate (source off). The hit efficiency is shown for aged wires of layers 1 and 4 and non-aged wires of layers 1 and 2.

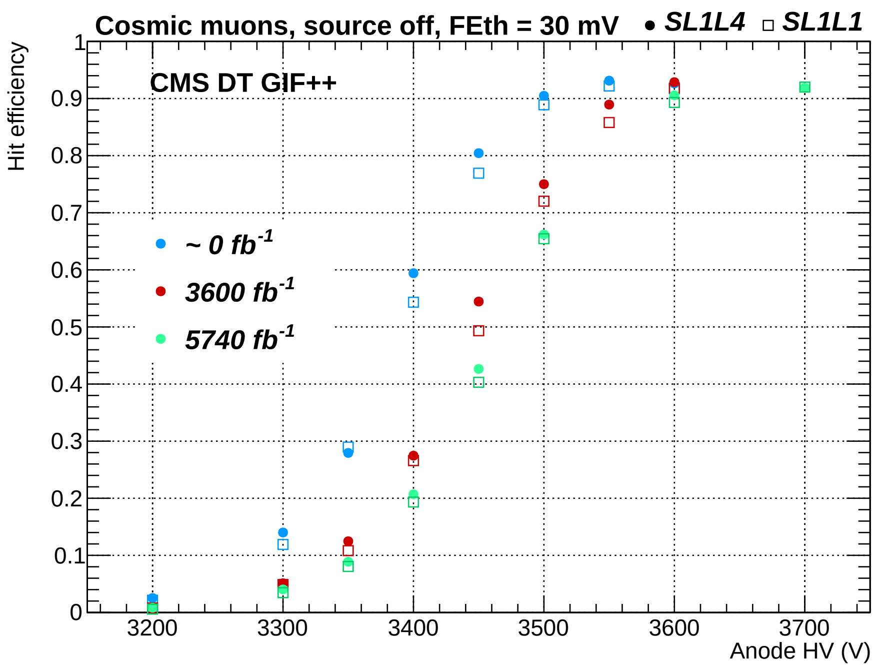

FIGURE 4.27: Hit efficiency as a function of the anode HV for three different scans on layers 1 and 4 of SL1. The scans were taken at the beginning of the irradiation period, at the end of era A and at the end of era B, using cosmic muons.

The effect of changing the FEth value between 20 and 30 mV has been also measured. Furthermore, the dependency of the hit efficiency with the background rate has been characterised for cosmic muons (figure 4.29) and beam muons (figure 4.30). A large drop of the efficiency is observed in the presence of a background rate for the aged layer, while it is not observed for the reference layer. The efficiency drop increases with the equivalent instantaneous luminosity.

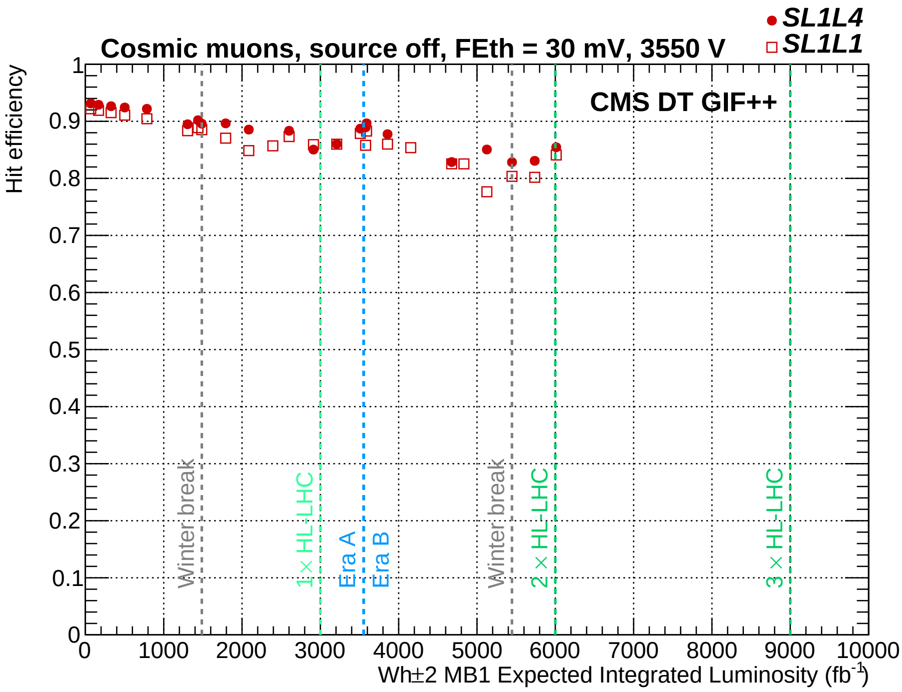

FIGURE 4.28: Evolution of the hit efficiency with the accumulated radiation for layers 1 and 4 of SL1. The data were taken almost each week during the irradiation period using cosmic muons, with a FEth of 30 mV and source off. The accumulated radiation is expressed in terms of the equivalent expected integrated luminosity for a MB1 DT chamber at CMS Wh±2 during the HL-LHC.

4.5.1 Scaling to the full detector

The measurements presented in the previous section sumarizes the characterization of the expected ageing of a DT chamber at the HL-LHC. In particular, we chose to study the effect of the ageing in terms of expected instantaneous and integrated luminosity at the HL-LHC for a MB1 chamber at wheels ±2, which will be the most irradiated DT chambers. To extrapolate the measured efficiency to the rest of the DT chambers of the CMS muon system, the expected background rate and integrated luminosity are obtained from the measurement of the integrated charge during the 2018 data taking at CMS for the 250 DT stations, correcting by the expected changes in the detector before the starting of the HL-LHC run.

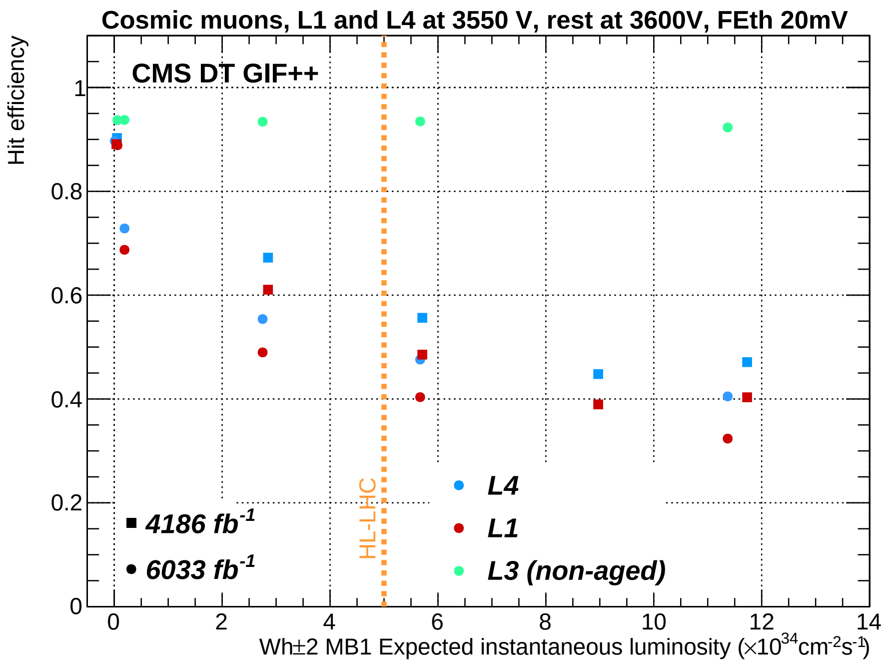

FIGURE 4.29: Hit efficiency as a function of the background rate, expressed in terms of the expected instantaneous luminosity at the HL-LHC for a MB1 DT chamber at CMS Wh±2. The measurements are done using cosmic muons with a FEth of 20 mV and at an anode HV of 3550 V for layers 1 and 4 at two different integrated luminosities and layer 3, at an anode HV of 3600 V, used as reference.

Some of the distributions shown in the previous section are fitted and used to obtain the dependency of the efficiency with respect to the background rate and the integrated luminosity. The efficiencies are calculated per DT station, assuming that it is the same for all the layers and the cells in each station. The extrapolation is done under these hypotheses:

- The efficiency as a function of the background rate is taken from the efficiency measurements with a muon beam, as the events are triggered with external scintillators, avoiding any bias on the trigger at high background rate.
- The efficiency as a function of the integrated dose at a background rate equivalent to that expected at the HL-LHC is obtained from the efficiency measurements with cosmic muons. The expected difference in this extrapolation between efficiencies with beam and cosmic muons is corrected by a factor calculated as the ratio between the drop of efficiency for beam and cosmic muons after irradiating the chamber by 3600 fb^{-1} of equivalent integrated luminosity.

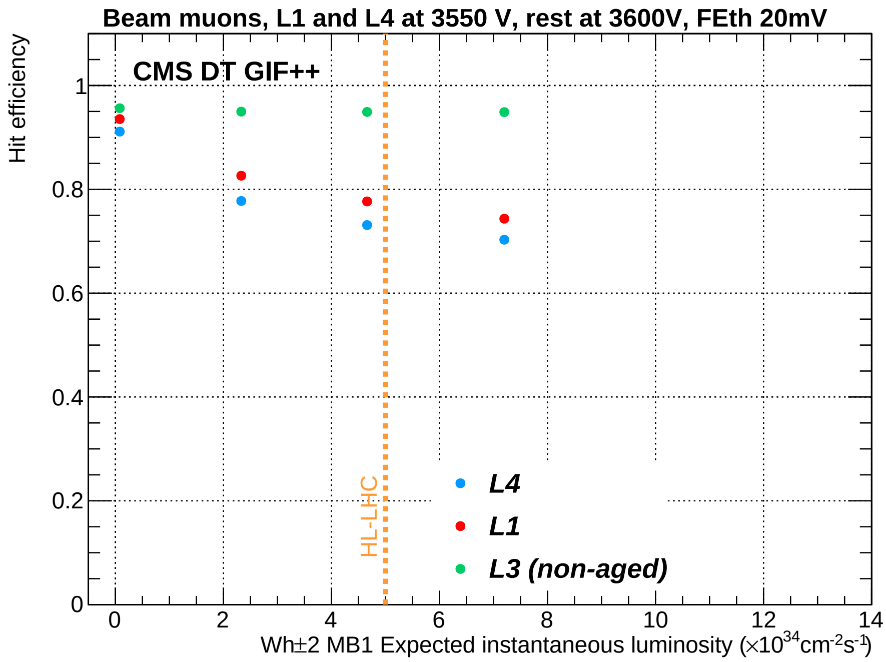

FIGURE 4.30: Hit efficiency as a function of the background rate, expressed in terms of the expected instantaneous luminosity at the HL-LHC for a MB1 DT chamber at CMS Wh±2. The measurements are done using beam muons with a FEth of 20 mV and an anode HV of 3550 V for layers 1 and 4 at two different integrated luminosities and layer 3, at an anode HV of 3600 V, used as reference.

- A safety factor of two in both the expected integrated luminosity at the end of the HL-LHC run and the background rate expected during the data taking at the HL-LHC is considered.
- The obtained efficiencies are scaled linearly to the rest of the detector according to the expected integrated charge, extrapolated from the measurements in the full CMS DT system during 2018.

The measured efficiencies as a function of the background rates for beam muons are fitted in figure 4.31. At an expected background rate of $5 \times 10^{34}\,\mathrm{cm}^{-2}\,\mathrm{s}^{-1}$, the efficiency for layer 1 is 0.77 and for layer 4 is 0.72. Considering the safety factor of 2, the hit efficiency at a background rate of $10 \times 10^{34}\,\mathrm{cm}^{-2}\,\mathrm{s}^{-1}$ is computed to be 0.73 for layer 1 and 0.69 for layer 4. An average value of 0.71 is considered.

To incorporate a safety factor of 2 also in the expected integrated luminosity, the evolution of the efficiency with the ageing in cosmic data, for a background rate equivalent to that expected at the HL-LHC, is used. The fit to the evolution of the efficiency with cosmic muons at a background rate close to the one expected at the HL-LHC as a function of the integrated luminosity is shown in figure 4.32.

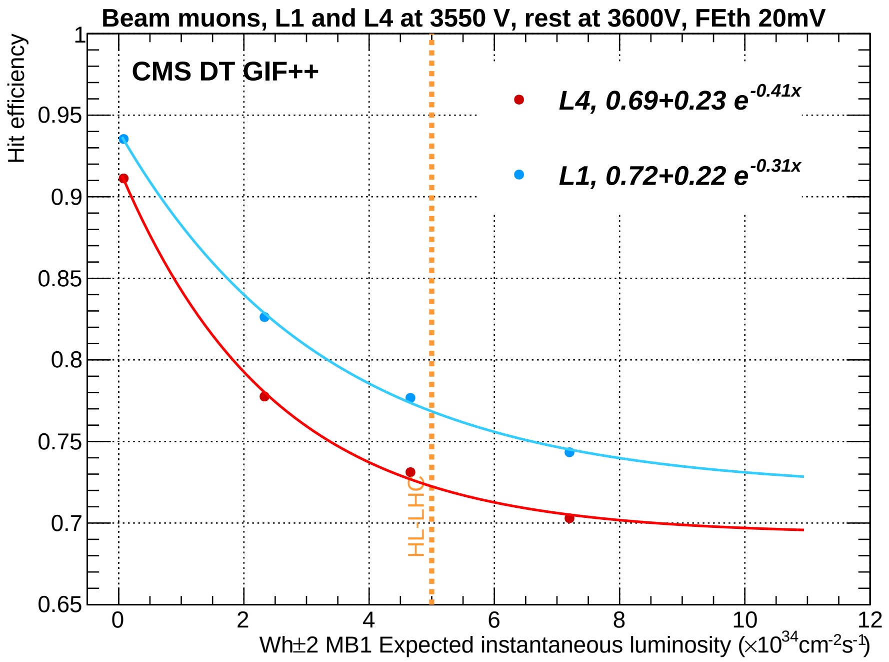

FIGURE 4.31: Exponential fit to the efficiency curve in figure 4.30.

To extrapolate this result to the hit efficiency with a muon beam, we take into account that the loss of efficiency is larger for cosmic muons than for beam muons. For an expected integrated luminosity of 3600 fb^{-1} and with a background rate equivalent to that expected at the HL-LHC, the measured efficiency drop using cosmic muons is 0.37 and using beam muons is 0.21. The extra drop of efficiency at an expected integrated luminosity of 6000 fb^{-1} was measured for cosmic muons, resulting in 0.16 (with respect to the measurement at an expected integrated luminosity of 3600 fb^{-1}). Extrapolating this result to the beam muons, the efficiency loss at $2 \times$ HL-LHC expected integrated luminosity is calculated to be 0.09. Finally, this number is substracted to the estimation at a safety factor of $2 \times$ HL-LHC in the background rate to obtain an expected efficiency of 0.62 for the MB1 chambers in wheels ± 2.

Figure 4.33 shows the expected efficiencies at the end HL-LHC for all the DT chambers of the CMS muon system under the aforementioned hypotheses.

4.6 Muon reconstruction efficiencies at CMS

To test the effect of the ageing on the CMS muon reconstruction, the reconstruction efficiency is obtained from simulation. The hit efficiency in each chamber is taken from the extrapolation shown in the previous section, using the efficiencies summarised in

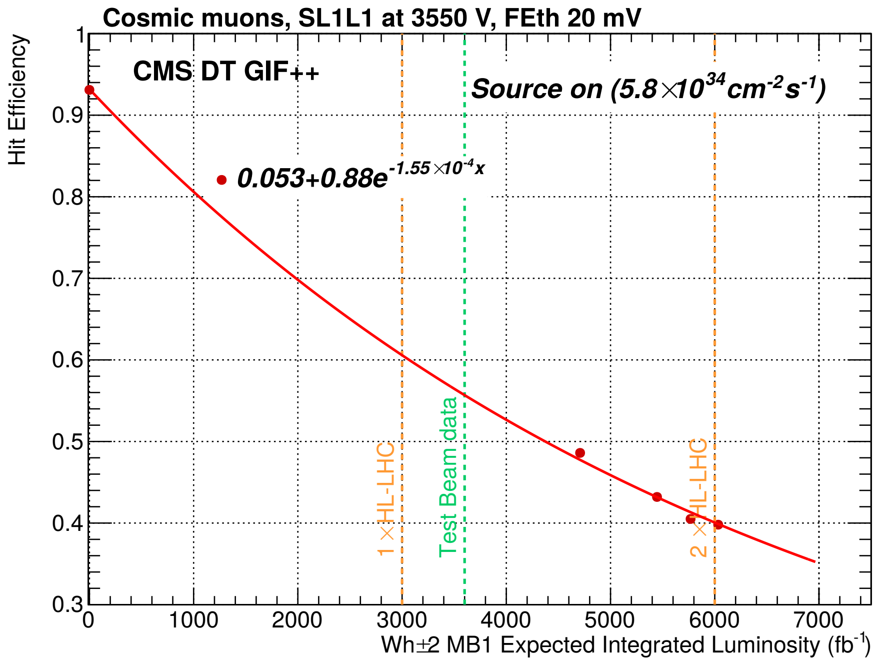

FIGURE 4.32: Hit efficiency for layer 1 in SL1 as a function of the integrated luminosity for cosmic muons taken with the source on, at a background rate slightly higher than the expected background rate at the HL-LHC, corresponding to a instantaneous luminosity of $5.8 \times 10^{34}\,\mathrm{cm^{-2}\,s^{-1}}$. The data are fitted using an exponential model.

figure 4.33. Dimuon events are generated in a range of p_{T} from 3 to 200 GeV. The events are reconstructed and tracks are selected if they are compatible with the CMS standalone muon reconstruction.

The reconstruction efficiencies are presented as a function of the pseudorapidity of the muon and the ϕ angle and compared to an ideal scenario with no ageing. The results are shown in figure 4.34.

The variation of the muon reconstruction efficiency is expected to be negligible over almost the whole eta range. A very small drop in the so called overlap region ($0.8 < \eta < 1.2$) is visible, where the reconstruction is highly dependent on the MB1 chambers and the probablility that a muon crosses more DT chambers is reduced.

4.7 Summary

In the context of the CMS phase-2 upgrade, the study of the ageing effects of the CMS DT chambers due to the radiation has been presented. This study has been performed using data taken at the GIF++ facility at CERN during 2017, 2018, and 2019. The effect

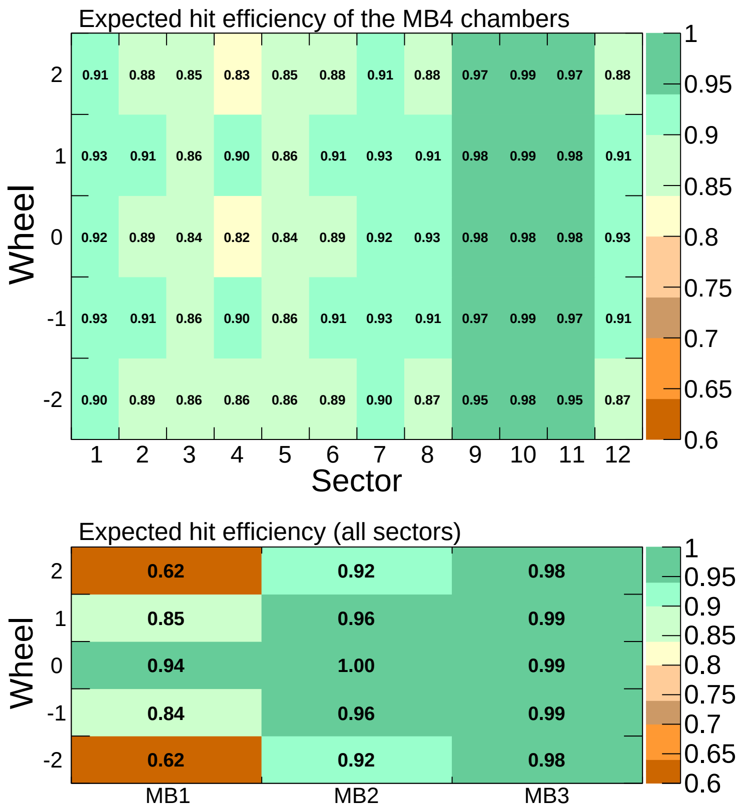

FIGURE 4.33: Expected hit efficiencies for MB4 chambers (upper) and for MB1, MB2 and MB3 (lower).

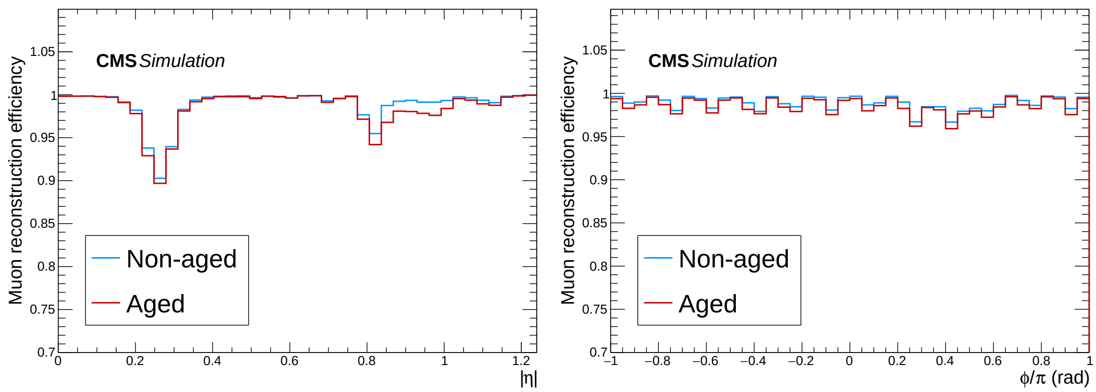

FIGURE 4.34: Muon reconstruction efficiency at CMS as a function of $|\eta|$ (left) and ϕ (right) for non-aged DT chambers and aged DT chambers with the efficiencies shown in figure 4.33. The efficiencies have been calculated using simulated dimuon events.

of the ageing has been shown and characterised in terms of the drop of rates and efficiencies. The efficiency drop for the MB1 chambers in wheels ± 2, that will be the most irradiated DT chambers at CMS, is expected to be about 38% at the end of the HL-LHC. However, the expected efficiency drop in the rest of the DT system is much smaller due to the lower background rate exposure.

The loss of hit efficiency has been computed for the full CMS DT system and the effect on the CMS muon reconstruction efficiency has been derived, showing a very small effect over the whole eta and phi ranges. To complement these results, wires that were extracted after era A irradiation period are being inspected in order to understand the origin of the observed ageing. Furthermore, the characterisation of the expected hit efficiency drop at the HL-LHC will be used to estimate the effect of the ageing on the performance of the trigger efficiency. The evaluation of this effect will be crucial to design and improve the trigger algorithms. The data collected will be also useful to design a strategy to reduce the ageing of the wires (for example by decreasing the anode HV at the beginning of the HL-LHC data taking) and increase the hit efficiency after certain accumulated radiation (for example by increasing the anode HV at the end of the HL-LHC data taking).

Chapter 5

Measurement of the top quark pair production cross section

5.1 Introduction

The $t\bar{t}$ production cross section is a key measurement for all the hadron collider experiments at high energies, as its measurement is crucial to probe QCD predictions, searches for new physics and to characterise the detector among others. The LHC can be considered a top quark factory due to the high rate of $t\bar{t}$ production in comparison with other SM processes.

When I joined the CMS collaboration, I started contributing to the CMS legacy $t\bar{t}$ measurements at 7 and 8 TeV [66]. In this paper, the cross section is measured by fitting several kinematic distributions and constraining uncertainties. I contributed to the cross check of the measurement with an event-counting approach. These measurements have smaller uncertainty than the best SM prediction.

In 2015 the LHC produced the first collisions at $\sqrt{s} = 13\,\text{TeV}$. The $t\bar{t}$ production rate increased by a factor of about 3.5 with respect to $\sqrt{s} = 8\,\text{TeV}$. A fast $t\bar{t}$ measurement was done using a very small amount of data, corresponding to $42 \pm 5\,\text{pb}^{-1}$. This is the first CMS result at $\sqrt{s} = 13\,\text{TeV}$ and was crucial to probe an excellent agreement of the SM $t\bar{t}$ predictions at this previously unexplored energy. The paper is published in [3], becoming one of the references to prove that the LHC Run 2 had successfully started and CMS was capable of testing the SM at $\sqrt{s} = 13\,\text{TeV}$.

This measurement was improved using the full 2015 dataset, corresponding to $2.2\,\text{fb}^{-1}$ (about 50 times the luminosity of the first measurement) [4]. With this amount of data the measurement is not statistics-dominated and a high precision, comparable with the one of the most precise theoretical predictions, could be reached.

At the end of 2015, the LHC produced a small amount of pp collisions at $\sqrt{s} = 5.02\,\text{TeV}$ in the context of a pp reference run for the heavy-ion collisions that took place later on at the same centre-of-mass energies (per nucleon). The amount of data corresponded to $27.4\,\text{pb}^{-1}$ and the expected $\text{t}\bar{\text{t}}$ production cross section is of about 70 pb, being about 12 times smaller than at 13 TeV and 2.5 times smaller than at 7 TeV. A great effort was done to obtain a cross section measurement at this unexplored energy, where almost no other measurements in pp collisions had been done and the detector had to be re-calibrated almost entirely [5].

Finally, the $\text{t}\bar{\text{t}}$ cross section was measured at $\sqrt{s} = 13\,\text{TeV}$ using the full 2016 dataset, corresponding to a luminosity of $35.9\,\text{fb}^{-1}$. This last measurement is performed using the same counting-experiment technique as for the previous ones and will be described in this thesis. The results are published together with a $\text{t}\bar{\text{t}}$ cross section measurement using a fit to $\text{t}\bar{\text{t}}$ kinematic variables in a paper that also includes a measurement of α_S and the top quark pole mass [6].

In this chapter, details of the $\text{t}\bar{\text{t}}$ cross section measurement are presented. An event-counting method is used for all of them but the experimental conditions are very different for each measurement: a very prompt measurement with low luminosity at a new $\sqrt{s}$, a precise measurement using the full 2015 dataset, a measurement using a huge dataset collected in 2016 and the one at $\sqrt{s} = 13\,\text{TeV}$ with an extremely low amount of data in an unexplored energy regime. The latest measurement at $\sqrt{s} = 13\,\text{TeV}$ using the full 2016 dataset is presented and used to explain the common method considered in most of the $\text{t}\bar{\text{t}}$ analyses of this thesis.

5.1.0.1 Previous measurements

The first $\text{t}\bar{\text{t}}$ inclusive cross section measurement was done just after the beginning of the Run 2 using a total luminosity of $42 \pm 5\,\text{pb}^{-1}$ [3]. The uncertainty on this measurement is highly dominated by the size of the sample. The methods used are very similar to the ones exposed in this chapter, but no b tagging is applied. After the event selection, 220 events are observed, while 29 ± 6 background events are expected. In this measurement the precision is dominated by the size of the sample. The result is:

$$\sigma_{\text{t}\bar{\text{t}}} = 746 \pm 58\,(\text{stat}) \pm 53\,(\text{syst}) \pm 36\,(\text{lum})\,\text{pb},$$

in agreement with the SM prediction. This measurement probes the SM top quark physics with pp collisions at $\sqrt{s} = 13\,\text{TeV}$ for the first time, showing that there is no physics beyond the SM visible with this level of precision. This measurement is one of the first measurements of the LHC RUN 2 and was crucial to demonstrate the complete functionality of the CMS detector.

For the measurement with the full 2015 dataset, corresponding to a luminosity of $2.2\,\text{fb}^{-1}$ [4], the same procedure as the one detailed in this chapter is followed. The measured cross section is:

$$\sigma_{\text{t}\bar{\text{t}}} = 815 \pm 9\,(\text{stat}) \pm 38\,(\text{syst}) \pm 19\,(\text{lum})\,\text{pb}.$$

With a total uncertainty of 5.3%, this result is as precise as the best theoretical predictions.

5.2 Top quark physics

In the SM, the top quark is the member with charge $+2/3$ of the weak-isospin doublet containing the bottom quark. With a measured mass of $m_\text{t} = 173.3\,\text{GeV}$ [67], its phenomenology is mostly driven by its large mass, being by far the heaviest elementary fermion in the SM.

Assuming that $|V_{\text{tb}}| = 1$, the top quark width is given at leading order (LO) by

$$\Gamma_\text{t}^{\text{LO}} = \frac{G_\text{F}}{8\pi\sqrt{2}} m_\text{t}^3 \left(1 - \frac{m_\text{W}^2}{m_\text{t}^2}\right) \left(1 + 2\frac{m_\text{W}^2}{m_\text{t}^2}\right). \tag{5.1}$$

Substituting, we obtain a value $\Gamma_\text{t}^{\text{LO}} =\sim 1.5\,\text{GeV}$. We can calculate the lifetime of the top quark as $\tau = 1/\Gamma$, obtaining a value of $\tau_\text{t} \sim 5 \times 10^{-25}\,\text{s}$. This extremely short lifetime makes the top quark a unique particle since it decays before hadronazing (hadronization time $\sim 1/\Lambda_{\text{QCD}} \approx 3 \times 10^{-24}\,\text{s}$). This property makes the top quark a unique particle that allows us to probe QCD predictions and set strong constrains on different theoretical quantities such as proton PDFs and α_S.

Furthermore, no bound states containing top quarks can exist (for example, top mesons of the type $\text{t}\bar{\text{q}}$ or a toponium bound state). Moreover, the spin polarisation and the correlation between spins in $\text{t}\bar{\text{t}}$ production are largely preserved in the decay of the top quarks, so the decay products mostly keep the top quark spin. Studying spin correlation of top quarks is then much easier than for other quarks.

Finally, the top quark Yukawa coupling is $y_{\mathrm{t}} = m_{\mathrm{t}}\sqrt{2}/v \simeq 1$, being by far the largest coupling of a fermion to the Higgs boson. The top quark plays a unique role on the stability of the Higgs potential and the renormalisation of its mass, as shown in section 2.3.1 and discussed later in section 6.2.

5.2.1 Top quark at hadron colliders

The top quark was discovered at the Tevatron collider, by the D0 and CDF collaborations [68, 69] in 1995, being the last discovery of a quark and the most massive particle known. At hadron colliders, top quarks are mostly produced in pairs. At Tevatron, proton-antiproton collisions were produced and thanks to the presence of valence antiquarks in the collisions, $\mathrm{t\bar{t}}$ pairs were mostly produced by $\mathrm{q\bar{q}}$ annihilation. On the other hand, at the LHC $\mathrm{t\bar{t}}$ production is dominated by gluon-gluon fusion ($\approx 85\%$ at $\sqrt{s} = 13\,\mathrm{TeV}$), followed by quark-antiquark annihilation ($\approx 15\%$). The Feynman diagrams of the LO contribution to $\mathrm{t\bar{t}}$ production cross section are shown in figure 5.1.

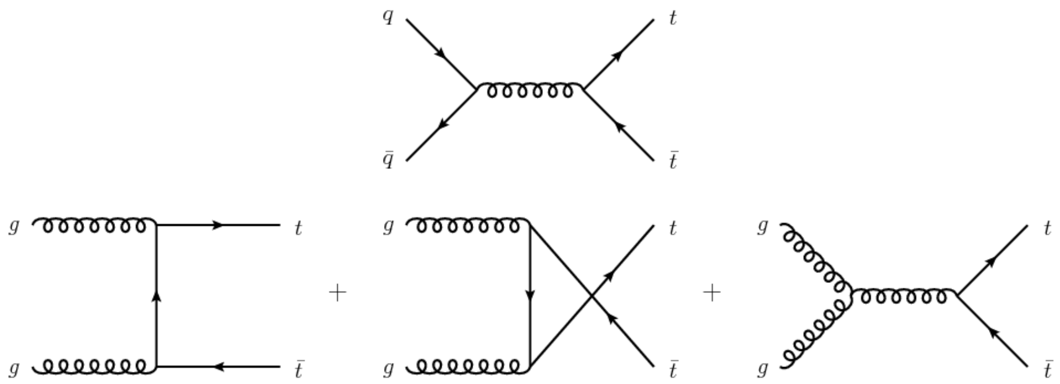

FIGURE 5.1: Leading order Feynman diagrams contributing to top quark pair production in pp collisions.

As $|V_{\mathrm{tb}}| \gg |V_{\mathrm{td}}|,|V_{\mathrm{ts}}|$, the decay of the top quark is dominated by $\mathrm{t} \rightarrow \mathrm{Wb}$. The experimental signature of the production of top quarks is characterised by the presence of high-p_{T} b jets coming from the hadronization of the b quarks. In the $\mathrm{t\bar{t}}$ production, depending on the decay of the W boson, different final states are possible. The final states are classified in three different channels, depending on the number of light leptons (electrons or muons) present: 0 - hadronic, 1 - semileptonic, 2 - dileptonic. The different classification in channels is shown in figure 5.2, along with the branching fractions for each final state.

Depending on the branching fraction of each final state and the amount of other events with similar final states (from other SM processes), which are called background events, each of the channels have different experimental properties. The hadronic

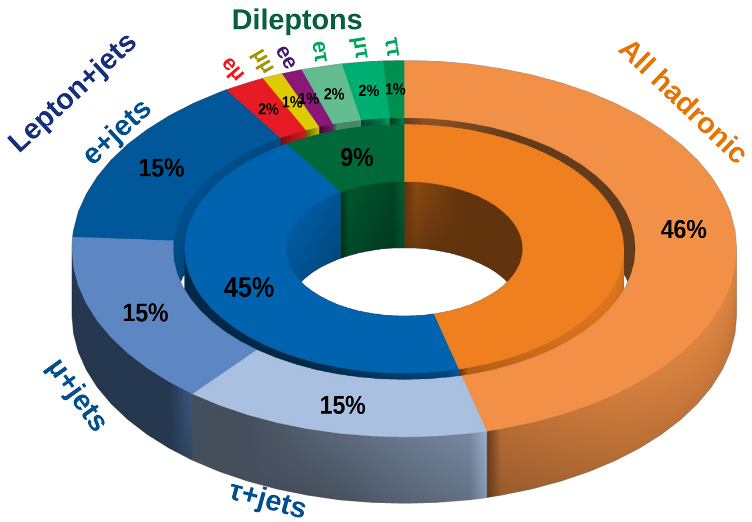

FIGURE 5.2: Chart representing the branching fractions of the different $t\bar{t}$ decay channels

channel has the largest branching ratio but most of the measurements in this channel have a limited precision (with respect to the measurements in other channels) due to the overwhelming background from QCD events. The identification of the two b jets coming from the decay of $t\bar{t}$ events, called signal, is crucial as it reduces significantly the amount of background events. The hadronically-decaying W bosons can be reconstructed from non b-tagged jets and the invariant mass of the top quarks (and $t\bar{t}$ system) can be reconstructed, obtaining some extra discrimination to background events and allowing measurements of differential cross sections.

The semileptonic channel allows to make measurements with lower uncertainties. First, the presence of the lepton allows to use leptonic triggers to record the events (which are usually much more efficient that hadronic triggers) and the lepton can be reconstructed with high accuracy. The p_{T} of the neutrino can be estimated from the $p_{\mathrm{T}}^{\mathrm{miss}}$ in the event, so this channel can be also used to fully reconstruct the top quarks and $t\bar{t}$ system. In this channel, the main background process is the production of a W boson, that has a very large cross section. The identification of b jets is crucial to discriminate between signal and background in this channel. The branching fraction to semileptonic final states is still quite high, so this channel makes the best precision for measurements with a limited amount of events.

Finally, the dilepton channel has a very small branching fraction but allows to select $t\bar{t}$ events with high precision in an almost background-free region. In this case, top quarks are not easily reconstructed due to the impossibility to detect the two neutrinos. In the e^+e^- and $\mu^+\mu^-$ channels the Drell-Yan process, consisting of the production of a Z boson or a virtual photon decaying into an opposite-charged lepton pair (DY,

$Z/\gamma^* \to \ell^+\ell^-$), is an important background process but can be strongly reduced by selecting events whose leptons do not reconstruct an invariant mass close to the one of the Z boson and requiring a large amount of p_T^{miss} in the event (which is very small for DY events, as there are no neutrinos). Nevertheless, the DY contamination in the $e^\pm\mu^\mp$ channel is very small, so this is the most precise final state to measure $t\bar{t}$ events. The b tagging of the jets is not crucial in dileptonic events, but the purity of the sample can be increased up to $> 90\%$ when at least one b-tagged jet is required.

5.3 Measurement at $\sqrt{s} = 13$ TeV

In this chapter, the top quark-antiquark production cross section measurement at $\sqrt{s} = 13$ TeV using 35.9 fb^{-1} of data is presented [6], using dilepton events.

The theoretical cross section is calculated at next-to-next-to-leading order (NNLO) plus next-to-next-to-leading-logarithmic accuracy [70], performed with the Top++ 2.0 program [71]. The calculation is:

$$\sigma_{t\bar{t}}^{13\,\text{TeV}} = 832^{+20}_{-29}\,(\text{scale}) \pm 35\,(\text{PDF}+\alpha_S)\,\text{pb}. \tag{5.2}$$

The presented measurement uses single and double lepton datasets corresponding to a total luminosity of 35.9 fb^{-1}, recorded by CMS during 2016. The data taking is subdivided in eras, named A to H. The good-quality data used in this analysis correspond to eras B to H. The luminosity conditions changed during eras G and H, which were collected with increased pileup.

5.3.1 Event simulation

Many MC samples are produced to estimate the background contribution, signal acceptance, and signal modelling uncertainties. In this analysis, the amount of signal events is huge and the background is very small. In order to perform a very precise cross section measurement, both the background estimation and the modelling of the signal must be very precise.

The POWHEG v2 [43–45] generator is used to simulate $t\bar{t}$ events at the next-to-leading order (NLO) in QCD, assuming a top quark mass of 172.5 GeV. The $t\bar{t}$ MC sample is generated using the CUETP8M2 tune [72], that was derived using an independent dataset of pp collisions at $\sqrt{s} = 8$ TeV to improve the simulation of the underlying event. This MC sample is used to estimate the acceptance of the $t\bar{t}$ signal. Alternative

$t\bar{t}$ samples are generated with POWHEG v2 varying several modelling parameters in order to assess modelling uncertainties on the $t\bar{t}$ acceptance. These samples will be described later.

For estimating the background from the production of a single top quark or antiquark in association with a W boson (tW), MC samples are produced at NLO using the POWHEG v1 [46] generator. The DY and the production of W or Z bosons in association with $t\bar{t}$ events (referred to as $t\bar{t}V$), are generated at NLO using the aMC@NLO v2.2.2 [42] generator. The production of the DY process is simulated with up to two additional partons and the FxFx scheme is used for the matching of the matrix elements (ME) and parton showers (PS) [73]. The contributions from WW, WZ, and ZZ (collectively referred to as VV) processes are simulated at LO using PYTHIA v8.205 [40].

The response of the CMS detector to the passage of the particles through the different layers of the subdetector is simulated for all the generated events using the GEANT4 package [74]. The effect of the PU is also simulated in the events by adding extra interactions for each hard scattering event.

Simulated events are normalised according to the integrated luminosity used and the best precision theoretical cross section calculation for each process. In particular, the DY theoretical cross section is computed at NNLO [75], approximate NNLO order for the tW process [76], and NLO for VV production [77] and the $t\bar{t}W$ and $t\bar{t}Z$ processes [78]. A list of the cross section (multiplied by the branching ratio of the considered final state) used to normalize the MC distributions is shown in table 5.1.

Process	Order	$\sigma \times$ BR (pb)
$t\bar{t}$	NNLO	831.8
tW, $\bar{t}$W	NNLO	35.85
$Z/\gamma^* \to \ell\ell$, $10\,\text{GeV} < m_{\ell\ell} < 50\,\text{GeV}$	NNLO	22635.1
$Z/\gamma^* \to \ell\ell$, $m_{\ell\ell} > 50\,\text{GeV}$	NNLO	6025.2
$W \to \ell\nu_\ell$(+jets)	NNLO	61526.7
WW	NLO	115.0
WZ	NLO	47.13
ZZ	NLO	16.523
$t\bar{t}W$, $W \to \ell\nu$	NLO	0.2043
$t\bar{t}W$, $W \to q'\bar{q}$	NLO	0.4062
$t\bar{t}Z$, $Z \to \ell\ell$ or $\nu\nu$	NLO	0.2529
$t\bar{t}Z$, $Z \to q\bar{q}$	NLO	0.5297

TABLE 5.1: Theoretical cross sections used to normalize the MC yields and order of the approximation.

The NNPDF 3.0 [22] PDF set is used for all the samples. Parton showering and hadronization are handled by PYTHIA in all the generated samples. The underlying event for all the background samples is modelled with the CUETP8M1 [79] tune.

5.3.2 Object definition

In this section, the selection requirements of the different objects used in the analysis are described.

5.3.2.1 Electrons

Electron candidates are required to have a p_T larger than 20 GeV and $|\eta| < 2.4$, excluding the pseudo-rapidity range of $1.444 - 1.566$, to avoid the crack between the barrel and endcap modules.

To avoid misidentifying electrons from hadronic jets or photons, a series of quality cuts are required on the variables described in section 3.3.3. These cuts are applied on quantities related to the reconstructed track of the electrons, the calorimetric deposits and the matching between the two. Most of the selection criteria are different for electrons reconstructed in the barrel ($|\eta| < 1.479$) and endcap ($|\eta| > 1.479$) regions.

The pseudorapidity width of the ECAL superclusters associated to the electron is required to be smaller than 0.01 (0.03) for barrel (endcap) electrons. The angular separation between the electron track from the vertex to the supercluster position has to be $\Delta\eta_{In} < 0.003(0.006)$ and $\Delta\phi_{In} < 0.08(0.04)$ for electrons in the barrel (endcap) region. The ratio between the measured energy in the ECAL for a given electron and the associated energy in the HCAL cells behind the electron superclusters has to be smaller than 4 (6.4)%. Moreover, the quantity $|1/\mathrm{E} - 1/\mathrm{p}|$ has to be smaller than 0.013. A conversion veto is set to reject tracks from electrons that may come from the interactions of photons with the detector material. From the innermost layer of the detector, the first valid hit of these electrons is not necessarily located in the first layer, so extrapolating the track of these electrons back to the interaction point, detector layers with no hits could be found. Furthermore, the electron candidates are required not to have missing hits in their track. Finally, a selection cut on the transverse and longitudinal impact parameters of $|d_{xy}| < 0.05$ (0.10) cm and $|d_z| < 0.10$ (0.20) cm respectively, for barrel (endcap) electrons is required. The identification criteria for electrons is summarised in Table 5.2.

The selected electrons are required to be isolated. The PF relative isolation, defined in equation (3.8), is calculated using PF candidates in a cone of $\Delta R = 0.3$. A requirement

	barrel	endcap
$\lvert d_z \rvert$	$< 0.10\,\mathrm{cm}$	$< 0.20\,\mathrm{cm}$
$\lvert d_{xy} \rvert$	$< 0.05\,\mathrm{cm}$	$< 0.10\,\mathrm{cm}$
$\sigma_{i\eta i\eta}$	< 0.01	< 0.03
$\lvert \Delta\phi_{In} \rvert$	< 0.08	< 0.04
$\lvert \Delta\eta_{In} \rvert$	< 0.003	< 0.006
H/E	< 0.04	< 0.064
$\lvert 1/E - 1/p \rvert$	< 0.013	
p_T	$> 20\,\mathrm{GeV}$	
$\lvert \eta \rvert$	$< 2.4, \notin [1.444, 1.566]$	
Conversion rejection		
No missing pixel hits		

TABLE 5.2: Electron selection requirements.

of $I^e_{PF} < f(p_\mathrm{T}(e), \eta(e))$ is done, where $f(p_\mathrm{T}(e), \eta(e))$ has a dependence on the electron transverse momentum and pseudorapidity, with integrated values of about 0.03 and 0.04 for barrel and endcap regions respectively. The contribution to the energy in the isolation cone from PF candidates associated to pileup events is subtracted following the procedure described in section 3.3.1.1.

5.3.2.2 Muons

The muon candidates are selected from PF candidates that are global muons with a p_T larger than 20 GeV and $|\eta| < 2.4$. They are required to have at least two matched stations and one valid pixel hit. The number of valid hits in the inner tracker must be of at least 6. The fit to the global muon track is required to have $\chi^2/\mathrm{ndof} < 10$. The transverse impact parameter, d_xy, is required to be less than 0.2 cm and less than 0.5 cm for the Z component of the impact parameter, d_z. These requirements are summarised in table 5.3.

p_T	$> 20\,\mathrm{GeV}$
$\lvert \eta \rvert$	< 2.4
$\lvert d_z \rvert$	$< 0.5\,\mathrm{cm}$
$\lvert d_{xy} \rvert$	$< 0.2\,\mathrm{cm}$
χ^2/ndof	< 10
Number of matched stations	≥ 2
Number of valid tracked hits	≥ 6
Is global muon	
I^μ_{PF}	< 0.15

TABLE 5.3: Muon selection requirements.

The relative muon isolation is computed from PF candidates in a cone of $\Delta R = 0.4$ and as defined in equation (3.8). The charged PF candidates from PU events are subtracted and a correction is applied for the expected contribution of neutral hadrons, following the procedure described in section 3.3.1.1. The selected muons are require to have $I^{\mu}_{PF} < 0.15$.

5.3.2.3 Jets and b identification

Jets are reconstructed from PF candidates. Selected jets must have a neutral fraction of hadronic energy < 0.99, a fraction of neutral electromagnetic energy < 0.99, a fraction of charged hadronic energy > 0, a fraction of charged electromagnetic energy < 0.99, a charge multiplicity > 0, and a number of constituents ≥ 2. On top of that, selected jets are required to have a $p_{\mathrm{T}} > 30\,\mathrm{GeV}$ and $|\eta| < 2.4$. The momentum of the jets is corrected according to the procedured exposed in section 3.3.5. Jets that overlap with selected leptons in a cone of $\Delta R = 0.4$ are not selected, to avoid double-counting of objects. The jet selection requierements are summarized in table 5.4.

p_{T}	$\geq 30\,\mathrm{GeV}$
$\lvert\eta\rvert$	< 2.4
Neutral hadronic energy	< 0.99
Neutral electromagnetic energy	< 0.99
Charged hadronic energy	$< 0.$
Charged electromagnetic energy	< 0.99
Charged multiplicity	$> 0.$
Number of constituents	$\geq 2.$
$\Delta R(\mathrm{jet, lepton})$	> 0.4

TABLE 5.4: Jet selection requirements.

Jets are b tagged using the CSVv2 algorithm defined in section 3.3.5.1. A working point of 0.848 is used, corresponding to a mistag rate of 1% and a b-tagging efficiency of about 70%. The b-tagging efficiency and mistag rate in simulation is corrected by applying jet-η- and jet-p_{T}-dependent scale factors to the CSVv2 value. These corrections are obtained from efficiency measurements in QCD multijet events [64].

5.3.2.4 Missing transverse momentum

Finally, the missing transverse momentum is reconstructed from PF candidates following the equation (3.3), with the corrections explained in section 3.3.6.

5.3.3 Event selection

In order to have a pure sample of $t\bar{t}$ events decaying into an $e^{\pm}\mu^{\mp}$ pair, an event selection is required. This selection is optimized to produce a high signal efficiency and acceptance while rejecting most of the background events. In figure 5.3, a scheme of the objects that are reconstructed in a $t\bar{t}$ event in the $e^{\pm}\mu^{\mp}$ channel is shown.

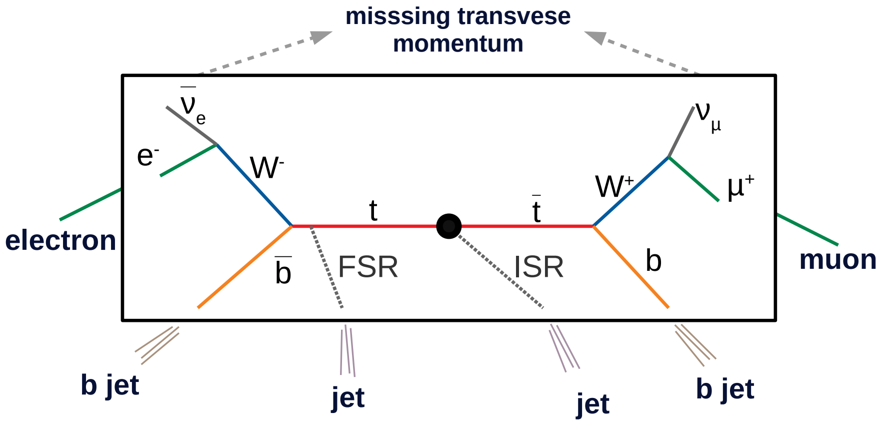

FIGURE 5.3: Scheme of the reconstructed objects from a $t\bar{t}$ event.

The selected events are required to pass either a single or a double lepton trigger. Double muon triggers are based on the presence of two isolated muons with $p_T >$ 23 GeV and 8 GeV respectively for the leading and subleading muons. Double electron triggers require the presence of two electrons with a $p_T > 23$ and 12 GeV. Electron-muon triggers are also used, requiring the presence of a muon with $p_T > 23$ GeV and a electron with $p_T > 12$ GeV or an electron with $p_T > 23$ GeV and a muon of $p_T > 8$ GeV. Single electron triggers used in this analysis require the presence of one electron with $p_T > 27$ GeV and some quality requirements. For the single muon triggers in this analysis, the presence of one isolated muon with $p_T > 24$ GeV is required.

The selected events are required to contain at least two leptons with $p_T > 25$ (20) GeV for the leading (subleading) lepton. The pair formed by the two leading leptons must have an invariant mass larger than 20 GeV. Regarding the charge of each lepton, if the leptons have the same sign of the charge (SS) they are classified as a SS event and stored apart to be later used in the nonprompt background estimate (section 5.3.5.1). If the pair contains one positive charge and one negative charge, the event is classified as opposite-sign (OS) pair and it is selected.

Furthermore, the events are classified in three different categories according to the flavour of the leptons: e^+e^-, $\mu^+\mu^-$, $e^{\pm}\mu^{\mp}$. The cross section measurement is done using events in the $e^{\pm}\mu^{\mp}$ channel. On the other hand, events in the e^+e^- and $\mu^+\mu^-$

channels are used as a cross check and to estimate the DY background contamination in the $e^{\pm}\mu^{\mp}$ channel, as explained in section 5.3.5.2. To reject the overwhelming amount of dilepton events comming from a Z boson in the same-flavour channels, a Z-veto cut is defined as $m_{\ell\ell} \notin |m_Z - 15|$, where $m_{\ell\ell}$ is the invariant mass of the dilepton pair and $m_Z = 91.19\,\text{GeV}$ is the mass of the Z boson [67]. Finally, selected events are requited to contain at least two jets and at least one b-tagged jet.

5.3.4 Efficiency measurements and corrections to the MC simulation

Simulated events have to be corrected to match the efficiency measurements in data. Several corrections, applied as weights to each event, are parametrized according to the p_T and $|\eta|$ of the leptons or other observables. In this section, these corrections are detailed.

Corrections to lepton reconstruction, identification and isolation efficiencies
The reconstruction, identification and isolation efficiencies are measured for muons and electrons with the tag-and-probe technique [61, 80], using events from Z decays. The tag-and-probe method uses narrow-width resonances as J/ψ or Z decaying into two leptons. One of the leptons (tag) is required to be a well identified and isolated lepton, while the other lepton (probe) passes a selection criteria that will define the denominator of the efficiency calculation. The pair must have an invariant mass close to the resonance. This invariant mass is reconstructed for data events in different phase space regions (typically p_T and η bins) and the resulting histogram is fitted with a signal+background model. The reconstruction, identification or isolation requirement of which we want to measure the efficiency is applied on the probe lepton and tag-and-probe pairs are classified into passing and failing categories depending on the outcome. The histograms with events in each category are fitted to a background + signal model and the efficiency is computed as the ratio of signal yields in both categories.

For electrons, the reconstructed efficiency has been measured as a function of η. The data-to-MC SF are shown in figure 5.4. The efficiencies of electron identification and isolation, as defined above for this analysis, have been measured taking reconstructed electrons as reference. The SF with associated uncertainties are shown in figure 5.5. The uncertainties are calculated by comparing the efficiencies with new efficiencies extracted with alternative fit models for both signal and background.

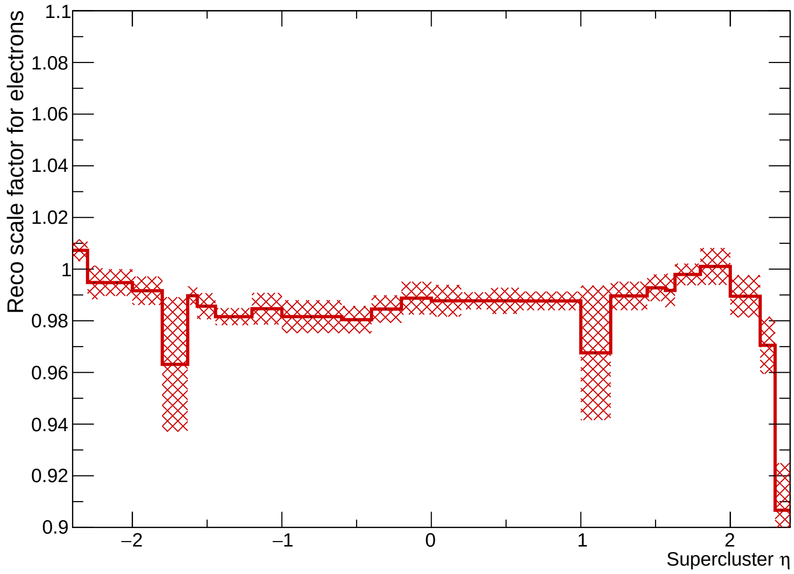

FIGURE 5.4: Electron reconstruction data-to-MC scale factors as a function of η of the associated supercluster, measured with respect to general electron candidates.

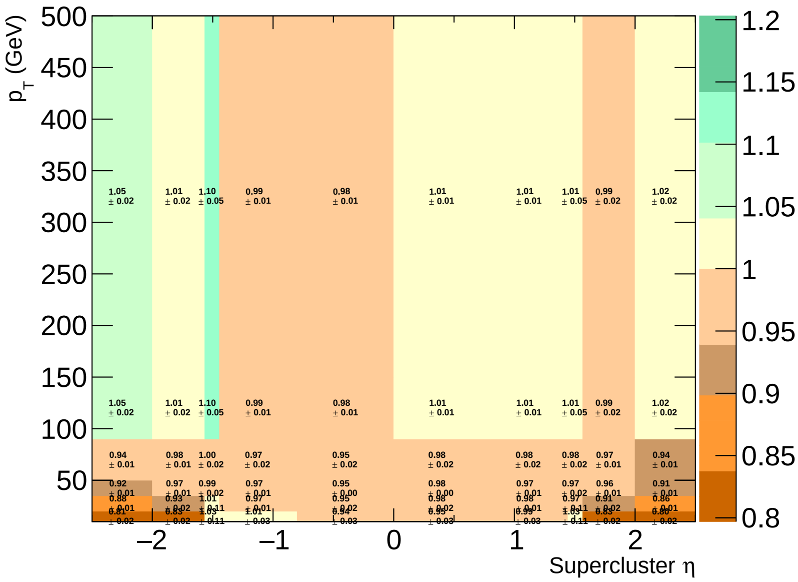

FIGURE 5.5: Electron identification and isolation scale factors as a function of p_T and η of the associated supercluster, measured with respect to reconstructed electrons.

For muons, the reconstruction efficiency is found to be very close to one in both data and simulation, so no scale factor is applied. The muon identification efficiency, defined with the aforementioned criteria, is measured with respect to isolated tracks, for each era of the 2016 data taking. To cope with a change in the detector performance, mainly due to changes in the instantaneous luminosity, the scale factors are grouped into one histogram for eras B, C, D, E and F and another histogram for eras G and H. The scale factors are shown in figure 5.6. The statistical errors are usually of the order or below 0.1% and a systematic uncertainty of 0.5% is applied. This uncertainty takes into account the precision of the method and is calculated by comparing with alternative efficiency measurements changing the definition of the mass window considered for the tag-and-probe pair, the isolation and p_{T} of the tag lepton, the number of bins in the fitted mass window and the fit models.

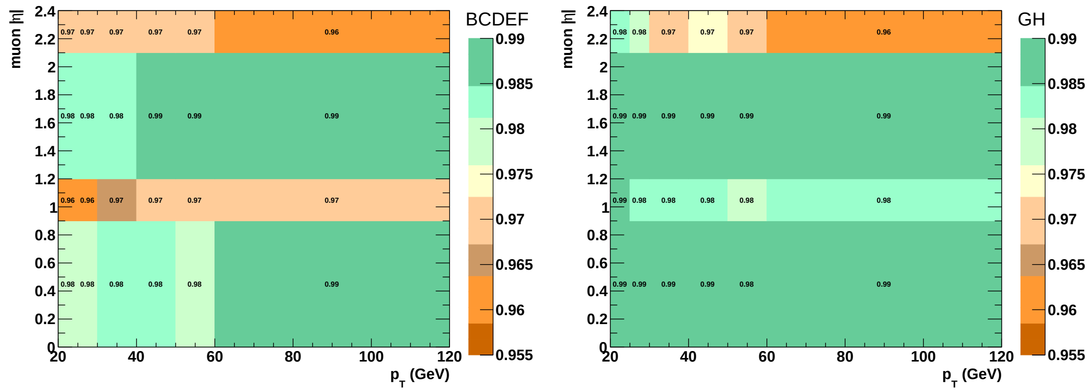

FIGURE 5.6: Muon identification scale factors for eras B, C, D, E and F (left) and eras G and H (right) of the 2016 data taking.

Finally, the muon isolation efficiencies are measured with respect to the previously identified muons. The isolation scale factors are shown in figure 5.7. The statistical uncertainties are small. An uncertainty on 1% is considered from the effect of hadronic activity in the phase space of the analysis, that is different from the one for DY events, used to measure the efficiency. The uncertainties coming from the method are small in comparison with this extrapolation uncertainty.

Trigger efficiencies and scale factors

The efficiency of the specific combination of trigger paths used in this analysis is measured using two different techniques: a tag-and-probe and a cross-trigger method. For the tag-and-probe, signal leptons from $Z \to e^+e^-$, $\mu^+\mu^-$ are used as signal. The trigger efficiency is measured independently for each lepton and combined after. The cross-trigger method uses events passing a series of $p_{\mathrm{T}}^{\mathrm{miss}}$-based trigger paths (orthogonal to

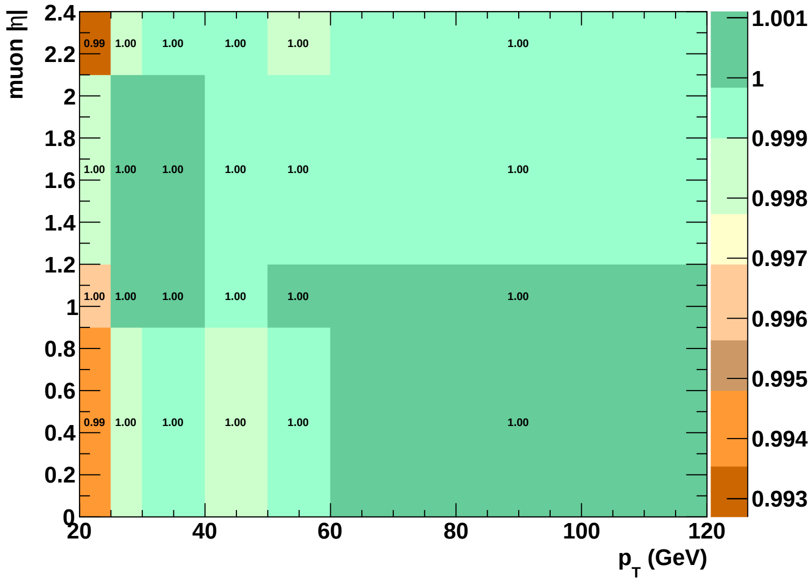

FIGURE 5.7: Muon isolation scale factors measured with respect to well identified muons.

lepton triggers) and checking if the selected events are collected by the combination of the leptonic triggers used in the analysis.

The two techniques are compared, obtaining similar results. The overall trigger efficiency for the selected events in the analysis is of about 98%, with some dependence in p_{T} and η. The efficiencies are also measured in MC. Small differences between the efficiencies in data and MC are corrected applying data-to-MC scale factors parameterised using the pseudorapidity of the two leptons. Other p_{T} and η parametrizations were tested but the dependence of the SFs on these observables is small. The 2D maps of trigger SFs applied to the simulated events is shown in figure 5.8.

Corrections to the b-tagging efficiencies

The b tagging efficiencies are measured in QCD data as a function of the discriminant value using the CSVv2 algorithm, as introduced in section 3.3.5.1. The discriminant value of the simulated jets is corrected according to p_{T}- and η-dependent SF, modifying the global b tagging and mistag efficiencies in simulation.

Pileup reweighting

The simulated PU in MC samples is corrected by applying weights to simulated events so the distribution of the number of vertices matches the observed distribution. The distribution of number of vertices before and after applying the reweighting for selected events after the dileptonic requirements is shown in figure 5.9.

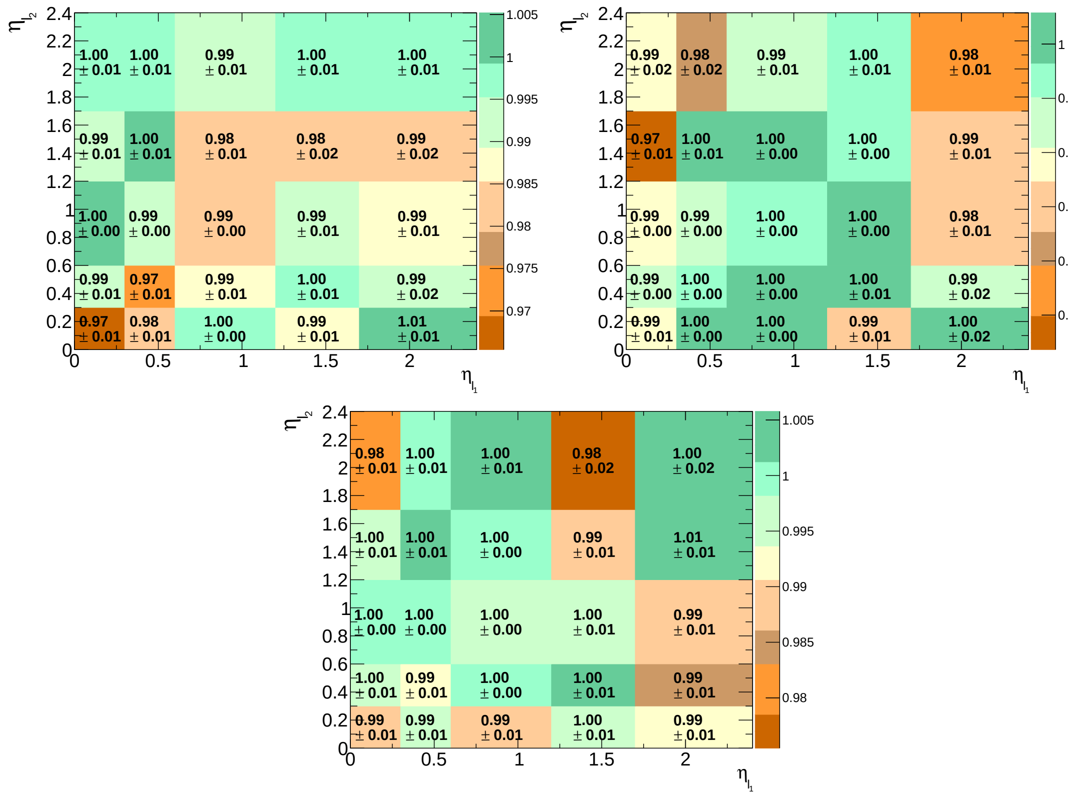

FIGURE 5.8: Trigger scale factors to be applied as weights on simulated e^+e^- (upper left), $\mu^+\mu^-$ (upper right) and $e^\pm\mu^\mp$ (lower) events.

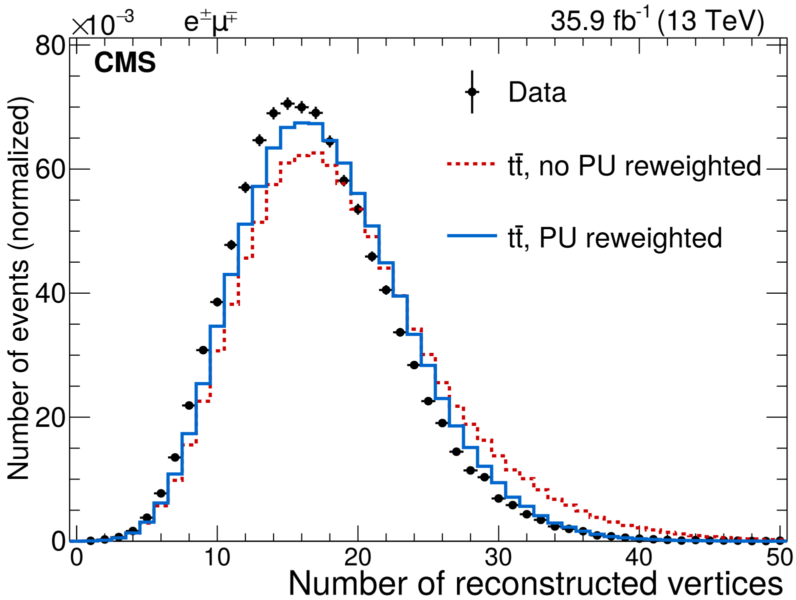

FIGURE 5.9: Distribution of the number of vertices for data, MC and PU-reweighted MC, for events containing an $e^\pm\mu^\mp$ pair.

5.3.5 Background estimate

In this analysis, the measurement of the $t\bar{t}$ cross section is done in dileptonic final states, so events coming from $t\bar{t}$ with semileptonic (or full hadronic) decays are considered as background. In this case, these events have only one lepton coming from the decay of a W boson (prompt lepton), so it must contain at least one nonprompt lepton, coming from the decay of a heavy flavour hadron or as the misidentification of a jet. A small background contamination of events coming from the production of a W boson accompanied by radiated jets, that may contain nonprompt leptons, are also expected. These events are grouped together into the nonprompt lepton background and are estimated from data, as detailed in section 5.3.5.1. The background events coming from DY production are estimated as detailed in section 5.3.5.2.

Background events arising from tW, $t\bar{t}$W, $t\bar{t}$Z and diboson events, in which at least two prompt leptons are produced from Z or W decays, are determined from simulation. This simulation includes all the corrections mentioned in section 5.3.3. The simulated events are weighted to the expected number of events using the most precise theoretical cross sections, shown in table 5.1.

5.3.5.1 Nonprompt leptons

The background contribution from events containing nonprompt leptons is usually not well modelled by MC simulation. To estimate this background, we consider the fact that the rate of identification of nonprompt leptons from a misidentified jet or a heavy flavour decay is independent of the charge of the nonprompt leptons. This implies that the nonprompt identification rate is the same if we select OS or SS dilepton pairs.

A SS control region is defined with the same criteria as for the signal event selection except for the charge of the dilepton pair. The number of events in the signal (OS) region is taken from SS data and extrapolated using a factor R. This factor is estimated from MC simulation and takes into account the difference in number of events with nonprompt leptons in the SS and OS regions. The factor R is estimated using $t\bar{t}$ events with semileptonic decays and events from W+jets production, as these are the processes with a dominant contribution to events with nonprompt leptons. The number of events with nonprompt leptons in the SS control region is estimated by subtracting the expected SS background contribution with prompt leptons (mainly $t\bar{t}$W and $t\bar{t}$Z production, and dileptonic $t\bar{t}$ decays with misassigned electron charge) to the observed data. The factor R is defined as:

$$R = \frac{N^{\mathrm{SS\,MC}}_{\mathrm{nonprompt}}}{N^{\mathrm{OS\,MC}}_{\mathrm{nonprompt}}}, \tag{5.3}$$

where $N^{\mathrm{SS\,MC}}_{\mathrm{nonprompt}}$ and $N^{\mathrm{OS\,MC}}_{\mathrm{nonprompt}}$ is the number of expected semileptonic $t\bar{t}$ and W +jets events with nonprompt leptons in the SS and OS regions respectively. Finally, the nonprompt leptons background estimate, $N^{\mathrm{OS}}_{\mathrm{nonprompt}}$, is estimated as:

$$N^{\mathrm{OS}}_{\mathrm{nonprompt}} = R\left(N^{\mathrm{SS}} - N^{\mathrm{SS\,MC}}_{\mathrm{prompt}}\right) \tag{5.4}$$

where N^{SS} is the observed events in data in the SS region and $N^{\mathrm{SS\,MC}}_{\mathrm{prompt}}$ is the number of events with prompt leptons expected in the SS region, calculated from MC simulation. The contribution of number of SS events for each process is detailed in table 5.5.

Source	$e^{\pm}\mu^{\mp}$
$t\bar{t} \rightarrow e\mu$	850 ± 100
Drell-Yan	42 ± 6
tW	70 ± 20
Dibosons	23 ± 7
$t\bar{t}$V	174 ± 52
Total promtp SS	1200 ± 110
Data	2539

TABLE 5.5: Number of observed and expected SS events with prompt leptons from different sources. The uncertainties come from the size of the sample and systematic uncertainties.

The distribution of expected and observed events for the number of jets for SS electron-muon events and for the b tag multiplicity for events containing an $e\mu$ SS pair and at least two jets is shown in figure 5.10. The nonprompt lepton estimate is splitted into the semileptonic $t\bar{t}$ contribution and others. The SS background with prompt leptons is divided into charge mismeasurements (charge flips), mainly from dileptonic $t\bar{t}$, and other processes, mainly from $t\bar{t}$W and $t\bar{t}$Z.

Finally, the nonprompt estimate in the $e^{\pm}\mu^{\mp}$ channel after the full event selection is shown in table 5.6.

SS data - Nonprompt	1340 ± 100
Nonprompt SS from MC	970 ± 80
Nonpromtp OS from MC	1100 ± 60
R	1.1 ± 0.1
Nonprompt leptons	1600 ± 170

TABLE 5.6: Estimation of background events from processes with nonprompt leptons, using a data-driven method in a SS control region.

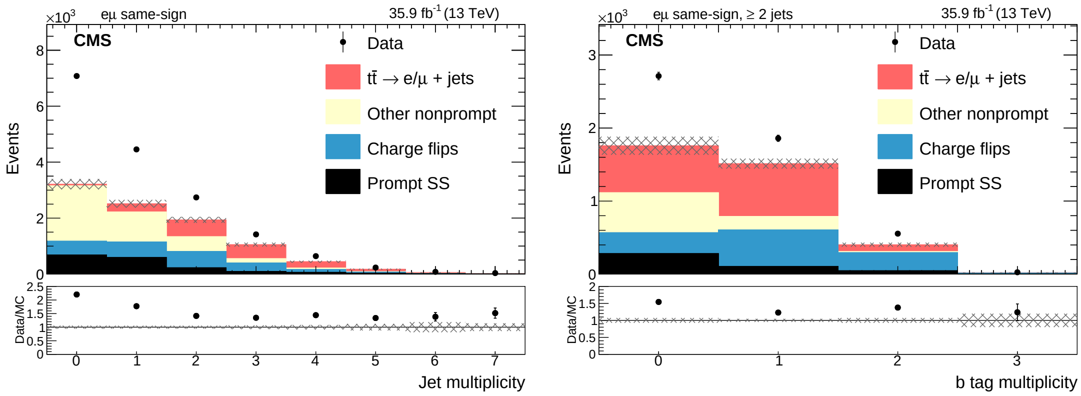

FIGURE 5.10: Distribution of the number of jets (left) and number of b-tagged jets (right) for events containing an $e\mu$ SS pair and an $e\mu$ SS pair plus at least 2 jets respectively. The uncertainties include MC statistics and experimental uncertainties on the MC simulation. The lower panel shows the ratio between the observed data and the MC prediction.

5.3.5.2 Drell-Yan

The DY events in the $e^{\pm}\mu^{\mp}$ final state come from the decay chain $Z/\gamma^* \to \tau\tau \to e^{\pm}\mu^{\mp}\nu_e\nu_\tau\nu_\mu\nu_\tau$. This background is estimated from data using the $R_{\mathrm{out/in}}$ method, as in previous $\mathrm{t\bar{t}}$ cross section measurements [66].

To estimate this background, the number of DY events in the Z-veto region (outside the Z peak) is estimated from data in the same-flavour channels ($N^{\ell\ell}_{\mathrm{out}}$, where ℓ is either e or μ). This estimation is done by counting the number of observed events within the Z region (defined as inverting the Z-veto cut), denoted as $N^{\ell\ell}_{\mathrm{in}}$, subtracting the expected background and extrapolating the result to the Z-veto region using the $R_{\mathrm{out/in}}$ multiplicative factor, estimated from DY MC simulation. The distributions of the leading lepton p_{T} and $|\eta|$ in each of the same-flavour channels is shown in figure 5.11. The invariant mass of the dielectron and dimuon pairs close to the mass of the Z boson is shown in figure 5.12. A good data-prediction agreement is observed.

The expected background in the Z region in data is estimated as the number of observed events in the $e^{\pm}\mu^{\mp}$ channel in the Z mass window ($N^{e\mu}_{\mathrm{in}}$), where no peak from DY is expected, multiplied by a factor 1/2 to correct for the branching ratio of the opposite-flavour channel and a factor $k_{\ell\ell}$ that corrects the acceptance of the lepton in the $e^{\pm}\mu^{\mp}$ channel different from the flavour of the lepton ℓ. This factor is defined for e^+e^- and $\mu^+\mu^-$, respectively, as

$$k_{ee} = \sqrt{N^{ee}_{\mathrm{in}}/N^{\mu\mu}_{\mathrm{in}}}, \text{ and } k_{\mu\mu} = \sqrt{N^{\mu\mu}_{\mathrm{in}}/N^{ee}_{\mathrm{in}}}. \tag{5.5}$$

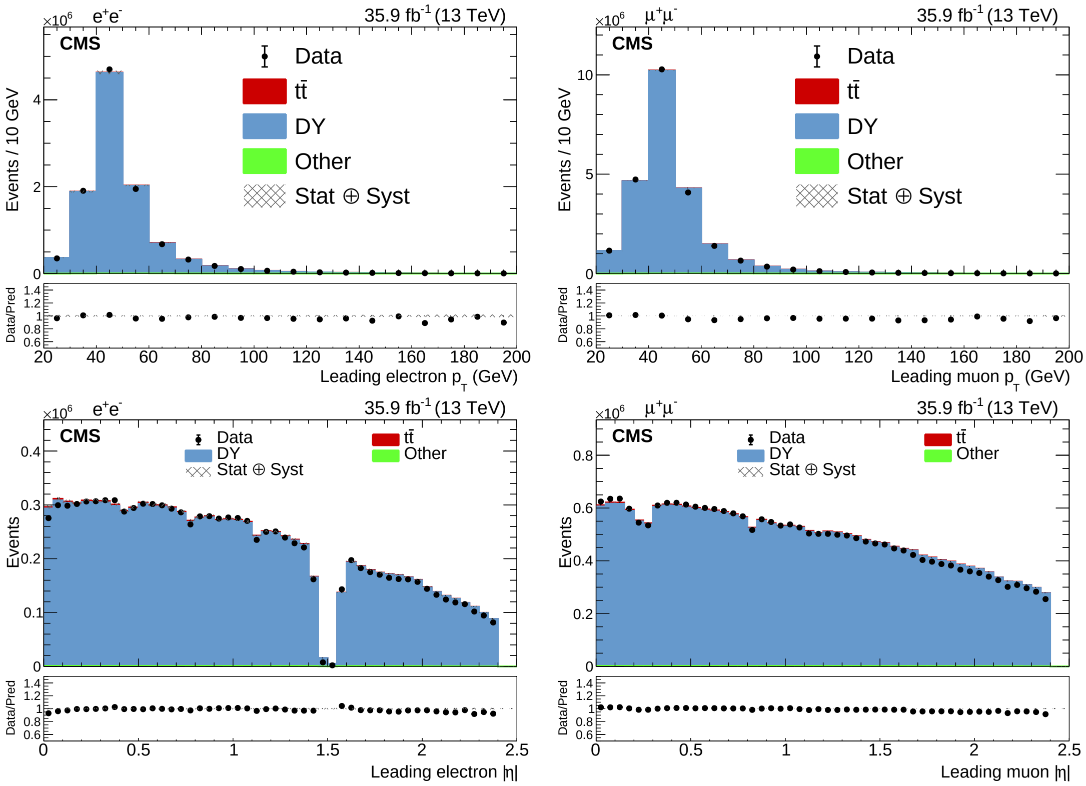

FIGURE 5.11: Leading lepton p_T (upper) and $|\eta|$ (lower) distributions of the highest-p_T lepton for selected events containing an e^+e^- (left) or $\mu^+\mu^-$ (right) pair. The background contribution from tW, VV and t$\bar{\text{t}}$V events are grouped into the "Other" category. The uncertainty bands represent the errors coming from the experimental uncertainties. The lower panel shows the ratio between the observed data and the MC prediction.

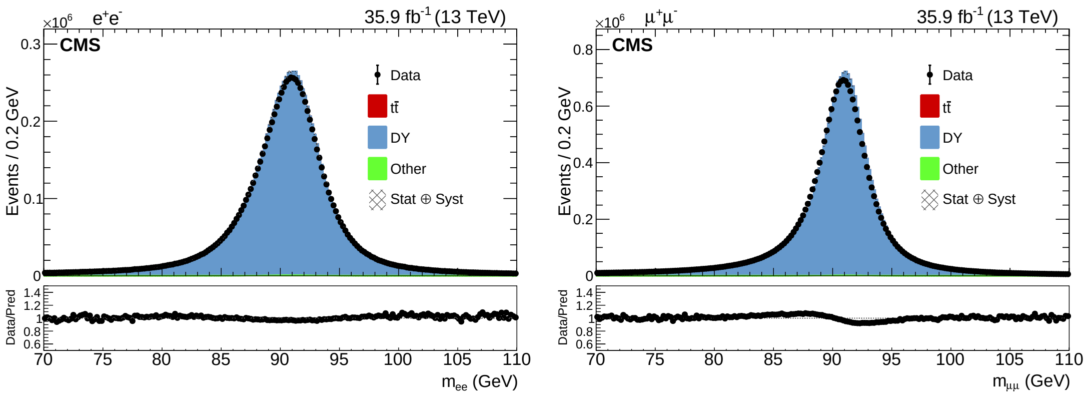

FIGURE 5.12: Invariant mass distributions close to the Z mass for selected events containing an e^+e^- (left) or $\mu^+\mu^-$ (right) pair. The background contribution from tW, VV and t$\bar{\text{t}}$V events are grouped into the "Other" category. The uncertainty bands represent the errors coming from the experimental uncertainties.

The factors k_{ee} and $k_{\mu\mu}$ are one the inverse of the other. Finally, the $R_{\text{out/in}}$ factor is estimated as the ratio between the number of events outside the Z peak ($N_{\text{out}}^{\text{DY MC}}$) and inside ($N_{\text{in}}^{\text{DY MC}}$), estimated with a DY MC sample

$$R_{\text{out/in}} = \frac{N_{\text{out}}^{\text{DY MC}}}{N_{\text{in}}^{\text{DY MC}}}. \tag{5.6}$$

The number of events in the same-flavour channels is obtained as:

$$N_{\text{out}}^{\ell\ell} = R_{\text{out/in}} \left(N_{\text{in}}^{\ell\ell} - \frac{1}{2} N_{\text{in}}^{e\mu} k_{\ell\ell} \right). \tag{5.7}$$

Finally, the number of expected events in the $e^{\pm}\mu^{\mp}$ channel is obtained by multiplying the DY MC prediction by a scale factor $SF_{e\mu}^{\text{DY}}$ defined as:

$$SF_{e\mu}^{\text{DY}} = \sqrt{SF_{ee}^{\text{DY}} \cdot SF_{\mu\mu}^{\text{DY}}}, \tag{5.8}$$

where the scale factors $SF_{\ell\ell}^{\text{DY}}$ are calculated for the same-flavour channels as the ratio between the DY observed events outside the Z region, calculated with equation (5.7), and the expected number of events in the same region calculated with the simulated DY MC sample. The histograms of the dilepton invariant mass of the selected events used for the DY estimation with the $R_{\text{out/in}}$ in the e^+e^- and $\mu^+\mu^-$ channels are shown in figure 5.13. The calculation of the scale factor after the full event selection for the $e^{\pm}\mu^{\mp}$ channel can be seen in table 5.7. Finally, the DY estimate is obtained by scaling the MC prediction by $SF_{e\mu}^{\text{DY}}$.

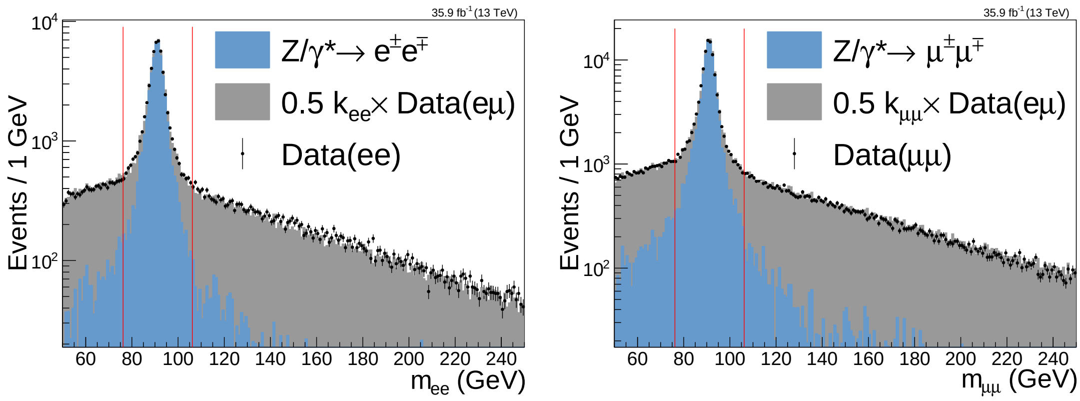

FIGURE 5.13: Histograms representing observed data and MC prediction for DY events after the selection, used to predict the DY background in the signal region, for the e^+e^- (left) and $\mu^+\mu^-$ (right) channels. The regions inside and outside the Z peak are shown.

To check the stability of the DY scale factor, it was derived for different jet selections: inclusive selection, at least two selected jets, at least two selected jets and at least

	e^+e^-	$\mu^+\mu^-$	$e^\pm\mu^\mp$
$N_{\mathrm{in}}^{\mathrm{DY\,MC}}$	46600 ± 600	97100 ± 900	
$N_{\mathrm{out}}^{\mathrm{DY\,MC}}$	3800 ± 200	8200 ± 300	
$R_{\mathrm{out/in}}$	0.081 ± 0.006	0.085 ± 0.004	
$k_{\ell\ell}$	0.692 ± 0.008	1.44 ± 0.02	
$N_{\mathrm{in}}^{\ell\ell}$	57300 ± 200	117200 ± 300	31000 ± 200
$N_{\mathrm{out}}^{\ell\ell}$	3800 ± 200	8000 ± 300	
$SF_{\ell\ell}^{\mathrm{DY}}$	1.00 ± 0.06	0.98 ± 0.04	0.99 ± 0.05

TABLE 5.7: DY estimate from data using the $R_{\mathrm{out/in}}$ method for events after the full event selection. The background contribution from tW, VV and $\mathrm{t\bar{t}V}$ events are grouped into the "Other" category. The uncertainties correspond to systematic and statistic sources.

one b-tagged jet. The SFs calculated in this exercise are shown in table 5.8. From this result, a systematic uncertainty of 15% is applied to the estimate of the DY background yield. Moreover, all the statistical uncertainties from the method are propagated to the DY scale factor and into the DY yield. The MC prediction for the distribution of the number of jets for dileptonic events is shown in figure 5.14. The agreement between data and prediction is good up to high jet multiplicities.

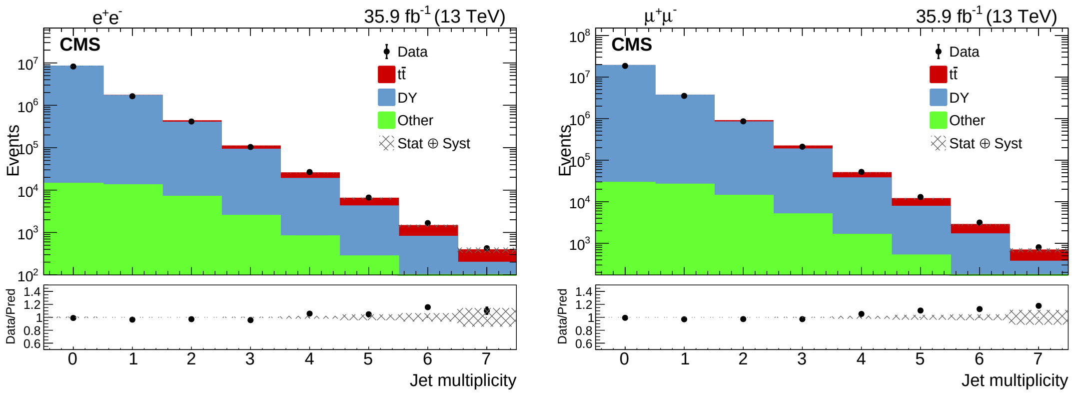

FIGURE 5.14: Jet multiplicity distributions for selected events containing an e^+e^- (left) or $\mu^+\mu^-$ (right) pair. The background contribution from tW, VV and $\mathrm{t\bar{t}V}$ events are grouped into the "Other" category. The uncertainty bands represent the errors coming from the experimental uncertainties. The lower panel shows the ratio between the observed data and the MC prediction.

	e^+e^-	$\mu^+\mu^-$	$e^\pm\mu^\mp$
≥ 1 b tag	1.00 ± 0.06	0.98 ± 0.04	0.99 ± 0.05
≥ 2 jets	0.993 ± 0.003	0.986 ± 0.002	0.990 ± 0.003
Dilepton	0.9940 ± 0.0001	0.9900 ± 0.0001	0.9920 ± 0.0001

TABLE 5.8: DY scale factors obtained with the $R_{\mathrm{out/in}}$ method for events after different event selections.

5.3.6 Methodology of the measurement

The cross section measurement is performed by counting the observed events after the selection, subtracting the expected background and extrapolating to the full phase space, using the formula

$$\sigma_{t\bar{t}} = \frac{N_{\text{obs}} - N_{\text{bkg}}}{\mathcal{A} \cdot \varepsilon \int \mathcal{L}dt \cdot BR}, \tag{5.9}$$

where N_{obs} and N_{bkg} are the number of observed and predicted background events, respectively, $\mathcal{A}$ accounts for the acceptance, ε is the efficiency, $\int \mathcal{L}dt$ is the integrated luminosity and BR is the branching fraction of $t\bar{t}$ events into the $e^{\pm}\mu^{\mp}$ final state.

The event selection described in 5.3.3 optimizes the term $N_{\text{obs}} - N_{\text{bkg}}$, so the statistical uncertainty is almost negligible and the background contribution is small. The distribution of the jet multiplicity of each background process, signal and data for events containing an $e^{\pm}\mu^{\mp}$ pair is shown in figure 5.15. The selected events must contain at least 2 jets. The distribution of b-tag multiplicity for these events with at least two jets is found in figure 5.16, where the high purity of the sample after selecting events with at least one b-tagged jet is shown.

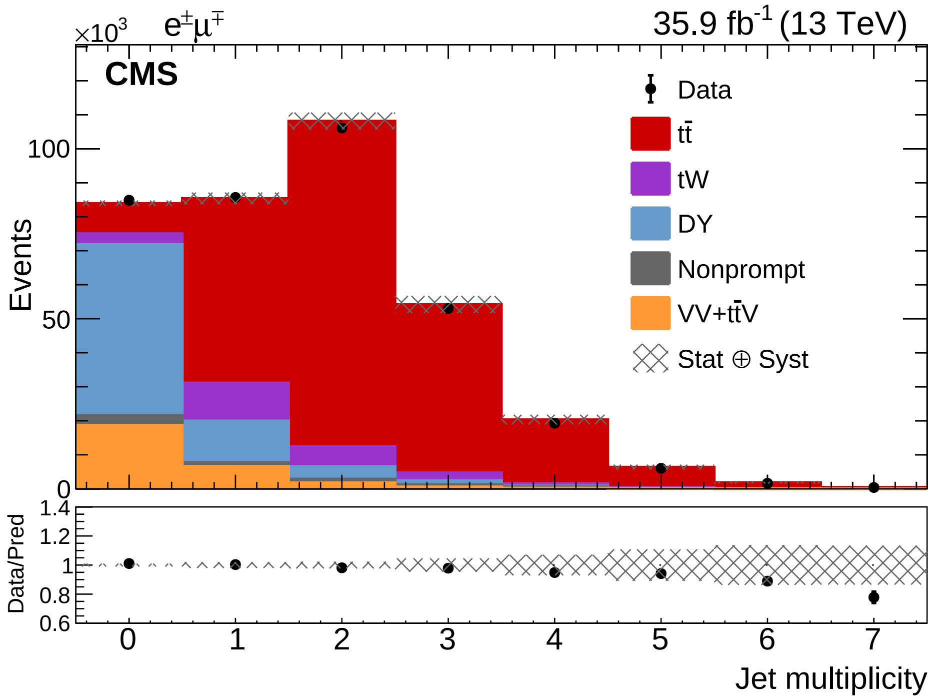

FIGURE 5.15: Distribution of the jet multiplicity for selected events containing an $e^{\pm}\mu^{\mp}$ pair. The error bands include statistical and systematic uncertainties. The lower panel shows the ratio between the observed data and the prediction.

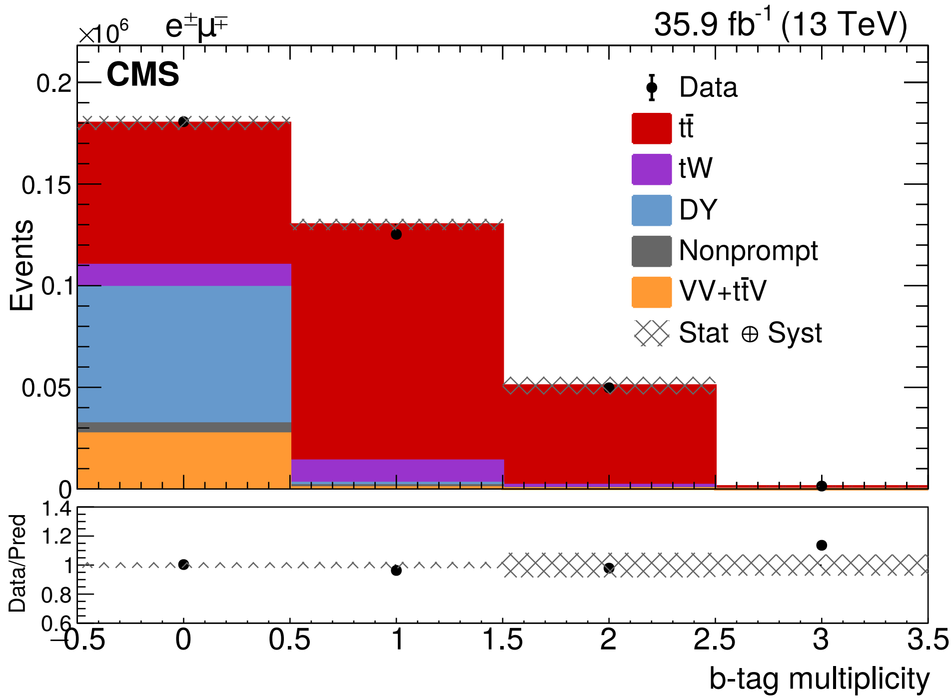

FIGURE 5.16: Distribution of the multiplicity of b-tagged jets for selected events containing an $e^{\pm}\mu^{\mp}$ pair and at least two jets. The error bands include statistical and systematic uncertainties. The lower panel shows the ratio between the observed data and the prediction.

The efficiency ε is estimated from the $t\bar{t}$ MC sample, after applying the corrections to the efficiency explained in section 5.3.3. The acceptance is estimated from MC simulation as the ratio between generated events passing the event selection applied on the generated particles over the total generated $t\bar{t} \to e^{\pm}\mu^{\mp}$ events. To avoid extrapolation uncertainties to the full phase space in the acceptance, the fiducial cross section is measured. The fiducial cross section is also called visible cross section, as it is calculated by counting events in the phase space region of sensitivity. It is defined using equation (5.9) but with $\mathcal{A} = 1$.

The selected phase space is found to reduce the background contamination, reaching a signal purity of about 94%, with a expected contribution of about 4% from tW production, being the other backgrounds very small. Figure 5.17 shows control plots for leading and subleading leptons in the signal region. All the expected background events not coming from tW production, estimated using MC simulation, are grouped into a single category called “Other”. Figure 5.18 shows control plots for the kinematics of the leading and subleading jets for selected events. Finally, 5.19 shows the distributions of electron-muon invariant mass and H_T, as defined in equation (3.11).

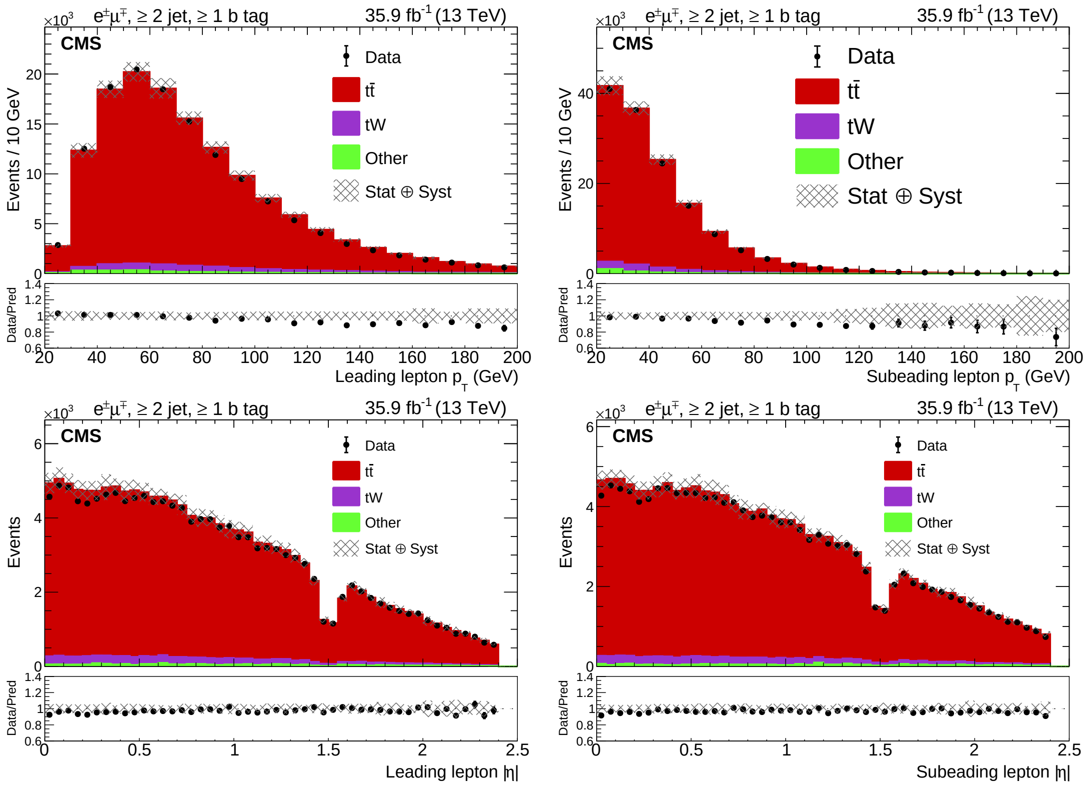

FIGURE 5.17: Lepton p_{T} (upper) and $|\eta|$ (lower) distributions of the highest-p_{T} (left) and second-highest-p_{T} (right) lepton for selected events containing an $e^{\pm}\mu^{\mp}$ pair, at least one jet and at least one b-tagged jet. Events from $\mathrm{t\bar{t}}$V, VV and DY processes are grouped into the "Other" category. The error bands include statistical and systematic uncertainties. The lower panel shows the ratio between the observed data and the prediction.

5.3.7 Systematic uncertainties

The $\mathrm{t\bar{t}}$ cross section measurement is affected by several sources of systematic uncertainties. In this section, the description of the sources of uncertainties is shown and their magnitude on the cross section measurement is presented. The different uncertainties are grouped in different categories, depending on the nature of the source and on which is the affected quantity in equation (5.9):

- The background uncertainties are associated to the background estimate N_{bkg} and includes uncertainties from theoretical calculations and from the data-driven methods. These uncertainties are summarised in section 5.3.7.1.
- The experimental uncertainties arise from different experimental sources mostly related with the efficiency ε. These uncertainties include effects from trigger efficiencies, jet energy scale (JES) an resolution (JER), b-tagging efficiencies, lepton identification an isolation efficiencies, etc. The effect of these sources are

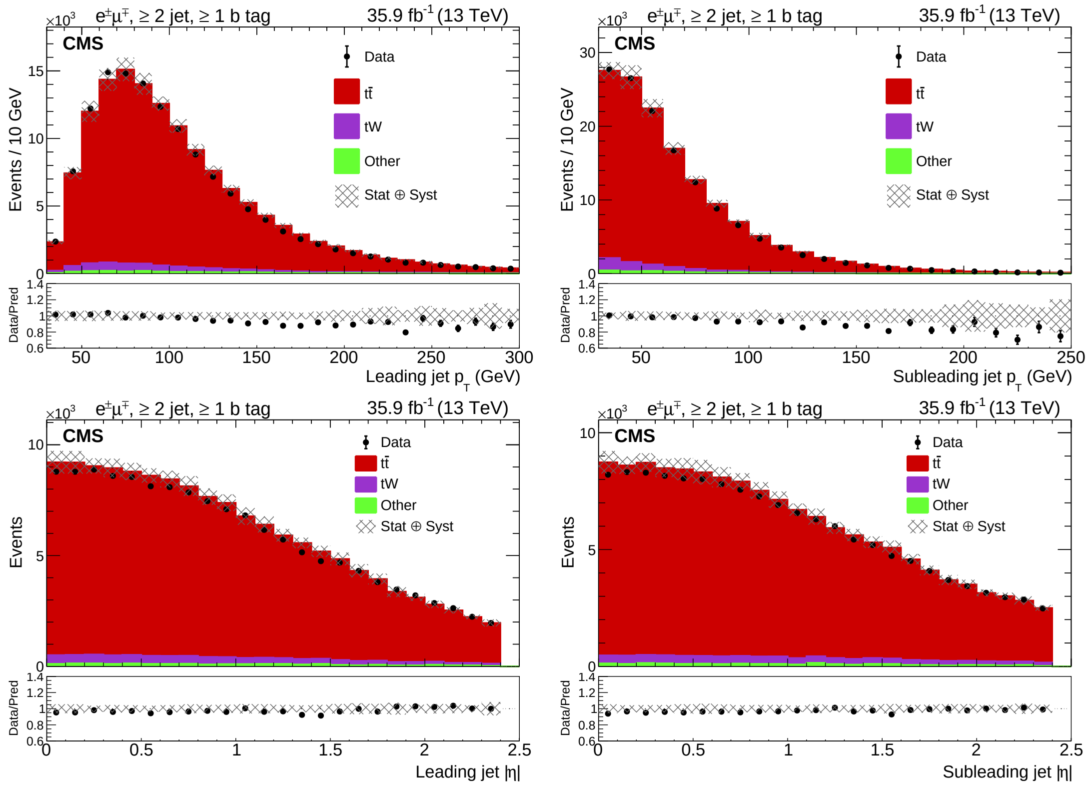

FIGURE 5.18: Jet p_T (upper) and $|\eta|$ (lower) distributions of the highest-p_T (left) and second-highest-p_T (right) jets for selected events containing an $e^{\pm}\mu^{\mp}$ pair, at least one jet and at least one b-tagged jet. Events from $t\bar{t}V$, VV and DY processes are grouped into the "Other" category. The error bands include statistical and systematic uncertainties. The lower panel shows the ratio between the observed data and the prediction.

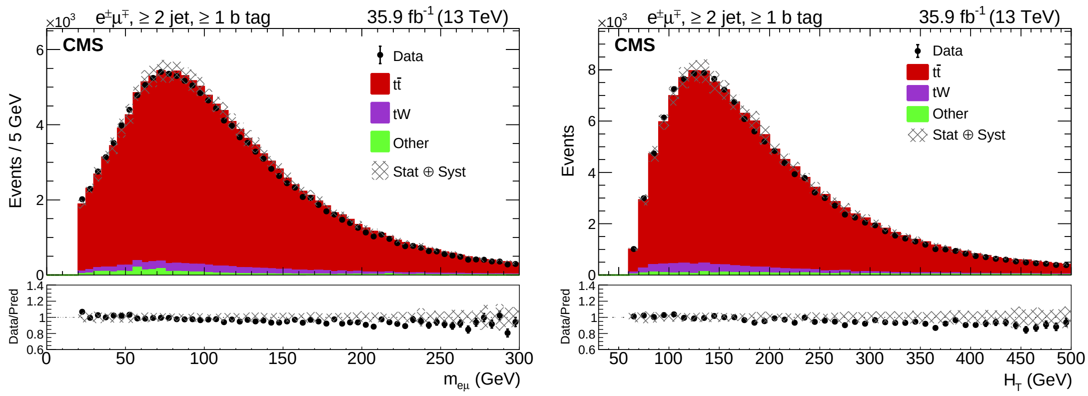

FIGURE 5.19: Invariant mass on the dilepton pair (left) and H_T (right) distribution for selected events containing an $e^{\pm}\mu^{\mp}$ pair, at least one jet and at least one b-tagged jet. Events from $t\bar{t}V$, VV and DY processes are grouped into the "Other" category. The error bands include statistical and systematic uncertainties. The lower panel shows the ratio between the observed data and the prediction.

propagated to the background and signal efficiencies. Details on how these uncertainties are computed are given in section 5.3.7.2.

- The modelling of the signal process, from a NLO MC sample, introduces uncertainties on the acceptance $\mathcal{A}$. Several sources of uncertainty are considered, affecting different aspects of the $t\bar{t}$ modelling such as the ME scales, proton PDFs or UE. The modelling uncertainties are explained in section 5.3.7.3.

The statistical uncertainty on the measurement depends only on the observed number of events, N_{obs}. Otherwise, the statistical uncertainties from the data-driven background estimations are considered as uncertainties on the background estimate.

The luminosity uncertainty is assigned to the $\int \mathcal{L}dt$ factor in equation (5.9). The uncertainty on the luminosity affects also the normalisation of the background estimate taken from MC simulation but this uncertainty is not quoted as luminosity uncertainty but within the background uncertainties. The uncertainty in the integrated luminosity is estimated to be 2.5% [81].

5.3.7.1 Uncertainties on the background estimate

Several uncertainties are considered in the background normalisation for the background contributions exposed in section 5.3.5. For the DY estimate, the statistical uncertainties from the method are propagated to the corresponding yield in the $e^{\pm}\mu^{\mp}$ channel. An extra 15% uncertainty is applied, covering differences in the scale factor with the jet and b tag multiplicity, as shown in section 5.3.5.2.

Normalisation uncertainties for the nonprompt leptons background are taken from the data-driven method. That includes the statistical uncertainties from SS data, experimental uncertainties on the SS prompt estimate and on the SS to OS factor. The total systematic uncertainty of the nonprompt estimate is 30%.

For the background processes estimated from MC, the experimental uncertainties presented in section 5.3.7.2 are considered. Normalisation uncertainties are also considered, taking into account the uncertainties on the theoretical cross section of each process. For tW, dibonsons, $t\bar{t}W$ and $t\bar{t}Z$ backgrounds, a normalisation uncertainty of 30% is considered.

The uncertainties on the background estimates are propagated to the total background yield N_{bkg} and to the measured cross section. The total effect of the uncertainties of each background contribution to the measured cross section is shown in table 5.10.

5.3.7.2 Experimental sources

The uncertainties on the trigger efficiency are propagated to the measurement by varying the data-to-MC SF shown in figure 5.8. These uncertainties are of the order of 1%, with a small dependency on the pseudorapidity of the leptons.

The electron reconstruction, identification and isolation efficiencies are varied within their uncertainties (statistical an systematic) [61], taken from the SFs shown in figures 5.4 and 5.5. The uncertainties on muon identification and isolation efficiencies are taken from the uncertainties on the SFs, of about 0.5% for identification and 1% for isolation [80]. The statistical uncertainties of the SFs are also taken into account.

The uncertainties associated with the JES and JER are determined by varying the momentum of the jets in bins of p_T and η, according to the uncertainties in the jet energy corrections, which amount to a few percent [82, 83]. These uncertainties are propagated to the selection of jets, which affect the expected $t\bar{t}$ and background yields in the analysis.

The uncertainties associated with the b-tagging efficiency and mistag rate are determined by varying the scale factors for correcting the efficiencies of the b-tagged jets and mistagged light-flavour jets, according to their uncertainties, as measured in QCD multijet events [64]. The average uncertainties on these scale factors for a $t\bar{t}$ sample are of the order of 1%, with a certain dependence on p_T and η.

Finally, the uncertainty from the PU reweighting procedure is evaluated by varying the inelastic pp cross section by its uncertainty of $\pm 4.6\%$ [84]. That uncertainty modifies the expected distribution of number of reconstructed vertices, which gives different values for the PU weights. The effect in the yields of varying the PU jets by their uncertainties is computed.

A summary of the experimental uncertainties in the $t\bar{t}$ cross section is shown in table 5.10.

5.3.7.3 Signal modelling

Several modelling uncertainties are calculated for the $t\bar{t}$ process, reflecting the limited knowledge of the main theoretical parameters used in the simulation, which mainly affect the estimation of the acceptance. The ranges of variation of these parameters were set in several previous CMS analyses [72] and the modelling of the $t\bar{t}$ process has been shown to accurately describe several kinematic variables within the systematic uncertainties [85]. The effect of this uncertainties on the $\mathrm{t\bar{t}}$ cross section measurement can be seen in table 5.10.

The uncertainty in the modelling of the hard interaction is assessed in the POWHEG sample by changing μ_{R} and μ_{F} by factors of 2 and 1/2 relative to their common nominal value of $\mu_{\mathrm{F}}^2 = \mu_{\mathrm{R}}^2 = m_{\mathrm{t}}^2 + p_{\mathrm{T,t}}^2$, where $p_{\mathrm{T,t}}^2$ denotes the square of the transverse momentum of the top quark in the $\mathrm{t\bar{t}}$ rest frame. The factors are varied independently and the effect of the variation is propagated to the acceptance and the cross section measurement. The maximum variation in the measured cross section is taken as an uncertainty. The cases where μ_{F}^2 and μ_{R}^2 are varied in different directions are considered nonphysical and discarded from the uncertainty propagation.

The uncertainty coming from the proton PDFs is propagated to the acceptance by reweighting the $\mathrm{t\bar{t}}$ simulated events according to the variations of a PDF set of 100 NNPDF3.0 replicas. The uncertainty is obtained as the root mean square value of the difference between the nominal yield and the variated yields, corresponding to each of the 100 variations [22]. The uncertainty on the value of α_S used in the generation of the $\mathrm{t\bar{t}}$ MC sample is propagated by reweighting the events by two sets with variations (up and down) according to the uncertainty of α_S. The uncertainty due to α_S on the cross section is taken as the difference between the nominal value and the maximum variation of the cross sections calculated with the two variation of α_S. The uncertainty from the proton PDFs and α_S added in quadrature.

The impact of the modelling uncertainties of the initial- and final-state radiation (ISR and FSR) is evaluated by varying the PS scales by factors of 2 and 1/2 [43] independently. FSR and ISR are considered as two separated sources of uncertainty. In addition, the impact of the matching between the ME and PS, which is parameterised by the POWHEG generator using a damping parameter defined as $h_{\mathrm{damp}} = 1.58^{+0.66}_{-0.59} m_{\mathrm{t}}$ [72], is calculated by varying this parameter, within its uncertainties and propagating the result to the final yields.

An uncertainty is assigned to the tune of the PYTHIA parameters to reproduce the observed UE [72, 86]. This uncertainty is computed by varying the tuned parameters by their uncertainties and propagate the effect to the acceptance in the $\mathrm{t\bar{t}}$ cross section measurement.

Finally, an uncertainty coming from the limited knowledge of the colour reconnection in $\mathrm{t\bar{t}}$ events is estimated by comparing different colour reconnection models and taking as the uncertainty the maximum variation in the $\mathrm{t\bar{t}}$ yields with respect to the nominal value. The procedure and the colour reconnection models are described in detail in Ref. [86].

5.3.8 Results

The number of observed and expected events after the final selection is shown in table 5.9. The expected tW background corresponds to about 4% of the observed events, being less than 2% the expected contribution from other processes.

Source	$e^{\pm}\mu^{\mp}$
Drell-Yan	$520 \pm 60 \pm 80$
Nonprompt leptons	$1600 \pm 170 \pm 500$
tW	$6400 \pm 50 \pm 1900$
Dibosons	$190 \pm 15 \pm 60$
$\mathrm{t\bar{t}V}$	$430 \pm 7 \pm 130$
Total background	$9100 \pm 120 \pm 2000$
$\mathrm{t\bar{t}} \to e\mu$	$135000 \pm 230 \pm 5700$
Data	139950

TABLE 5.9: Observed an expected events for each background contribution and $\mathrm{t\bar{t}}$ events after the selection. The uncertainties correspond to statistical and systematic uncertainties respectively.

The detailed set of uncertainties in the cross section is shown in table 5.10. The total uncertainty on the measured $\mathrm{t\bar{t}}$ cross section is of 4.3%, being dominated by the systematic uncertainty of 3.6%. The dominant systematic uncertainties come from the effect of the JES and lepton efficiencies.

The measured inclusive cross section is

$$\sigma_{\mathrm{t\bar{t}}} = 804 \pm 2\,(\mathrm{stat}) \pm 29\,(\mathrm{syst}) \pm 20\,(\mathrm{lum})\,\mathrm{pb}$$

in agreement with the SM prediction. Using generator quantities of $\mathrm{t\bar{t}}$ events for a top quark mass of 172.5 GeV, an acceptance of $\mathcal{A} = 0.457 \pm 0.006$ is obtained. Using a value of the branching ratio for the $\mathrm{t\bar{t}} \to e^{\pm}\mu^{\mp} + 2\mathrm{b}$ decay of BR = 0.0326 [67], the value of the fiducial cross section is

$$\sigma_{\mathrm{t\bar{t}}}^{\mathrm{fid}} = 12.0 \pm 0.03\,(\mathrm{stat}) \pm 0.42\,(\mathrm{syst}) \pm 0.29\,(\mathrm{lum})\,\mathrm{pb}.$$

The total efficiency, including all the efficiencies related to trigger, leptons, jets and b tagging, is $\varepsilon = 0.3041 \pm 0.0085$.

5.3.8.1 Dependency as a function of the top quark mass

In addition, alternative $\mathrm{t\bar{t}}$ signal MC samples are produced with different top quark masses, so the dependency of the measured cross section with the top quark MC mass

Source	Uncertainty (pb)	(%)
Electron efficiencies	11.8	1.5
Muon efficiencies	10.1	1.3
Trigger efficiencies	5.2	0.6
JES	12.0	1.5
JER	1.0	0.1
b-tagging efficiency	9.0	1.1
Mistagging efficiency	0.9	0.1
PU	3.4	0.4
UE	4.6	0.6
ME/PS matching (hdamp)	5.5	0.7
ISR scale	4.1	0.5
FSR scale	10.5	1.3
μ_{R} and μ_{F} scales	1.1	0.1
PDF+α_S	4.9	0.6
Color reconnection	8.2	1.0
MC statatistics	1.4	0.2
Dibosons	0.3	0.04
Nonprompt leptons	3.1	0.4
$\mathrm{t\bar{t}V}$	0.8	0.1
tW	11.7	1.5
DY	0.5	0.1
Total systematic	28.6	3.6
Integrated luminosity	19.6	2.4
Statistical	2.3	0.3
Total	34.7	4.3

TABLE 5.10: Summary of all the uncertainty sources affecting the cross section measurement and their impacts on the $\mathrm{t\bar{t}}$ cross section measurement.

can be studied. The cross section is measured with different acceptance values for m_{t} between 166.5 and 178.5 GeV. The results are fit using a linear function. A difference of -4.22 ± 0.07 pb in the $\mathrm{t\bar{t}}$ cross section for each mass difference of 0.5 GeV in the top quark mass is observed. The fit to the measured cross section can be seen in figure 5.20.

5.4 Measurement at $\sqrt{s} = 5.02\,\mathrm{TeV}$

In this section, the $\mathrm{t\bar{t}}$ inclusive cross section measurement at $\sqrt{s} = 5.02\,\mathrm{TeV}$ is presented [5]. This is the first $\mathrm{t\bar{t}}$ cross section measurement at this centre-of-mass energies, which is the lowest centre-of-mass energy where the $\mathrm{t\bar{t}}$ cross section is measured in pp collisions. Moreover, it is the only $\mathrm{t\bar{t}}$ cross section measurement up to date at $\sqrt{s} = 5.02\,\mathrm{TeV}$.

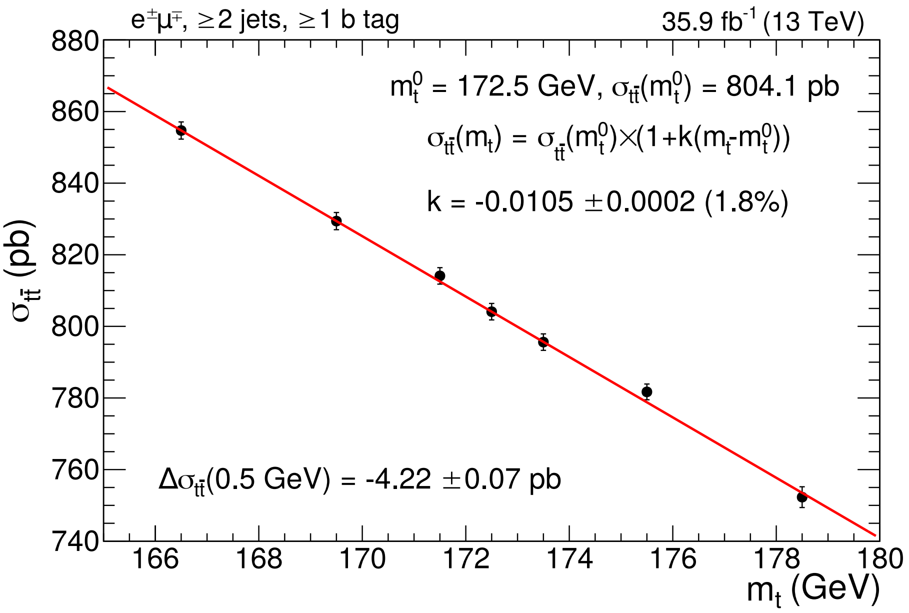

FIGURE 5.20: Measurement of the top quark pair production cross section as a function of the top quark mass. The measured dots are fitted to a linear function. The errors correspond to statistical uncertainties (from MC sample size).

5.4.1 Introduction

At the end of the 2015 LHC data taking, a heavy ion collisions run was planed, at a centre-of-mass energy of $\sqrt{s} = 5.02\,\text{TeV}$. In preparation for these collisions, a short reference run with pp collisions at the same $\sqrt{s}$ was taken. An integrated luminosity of $27.4 \pm 0.6\,\text{pb}^{-1}$ was recorded [87]. The main difference in the running conditions in comparison with the collisions at $\sqrt{s} = 13\,\text{TeV}$ is the amount of pileup interactions: the mean number of collisions per bunch crossing during this run is about $< n >= 1$.

The $\text{t}\bar{\text{t}}$ inclusive cross section is expected to highly increase with the centre-of-mass energy, so the predicted cross section at $\sqrt{s} = 5.02\,\text{TeV}$ is much lower than at $\sqrt{s} = 13\,\text{TeV}$. The theoretical cross section is calculated at NNLO, including resummation at next-to-next-to-leading-logarithmic accuracy [70], performed with the TOP++ 2.0 program [71], using the NNPDF 3.0 set of NNLO PDFs, obtaining a value of:

$$\sigma_{\text{t}\bar{\text{t}}}^{5.02\,\text{TeV}} = 68.9^{+1.9}_{-2.3}\,(\text{scale}) \pm 2.3\,(\text{PDF})^{+1.4}_{-1.0}\,(\alpha_S)\,\text{pb}. \tag{5.10}$$

One unique feature of this measurement is its particular sensitivity to high-x gluon PDF, as $\text{t}\bar{\text{t}}$ pairs are produced at $\sqrt{s} = 5.02\,\text{TeV}$ mostly by gluons that carry a relatively large amount of the energy of the proton. In this analysis we demonstrate that a $\text{t}\bar{\text{t}}$

cross section measurement at this centre-of-mass energy improves the knowledge of the proton PDF [5].

The measurement is performed independently using $e^{\pm}\mu^{\mp}$ and $\mu^{+}\mu^{-}$ events and later combined with a measurement in the lepton + jets channel. For the measurement in the $e^{\pm}\mu^{\mp}$ channel, a strategy very close to the one explained in this chapter is followed. The measurement in the $\mu^{+}\mu^{-}$ channel is presented in section 5.4.3. The combined results are shown in section 5.4.4.

5.4.2 The $e^{\pm}\mu^{\mp}$ channel

In this analysis, events are selected from single-muon triggers with a p_{T} threshold of 18 GeV. Selected electrons are require to have a $p_{\mathrm{T}} > 20$ GeV and $|\eta| < 2.4$. Muons are selected if their p_{T} is of at least 18 GeV and they are in a pseudorapidity range of $|\eta| < 2.4$. On the other hand, in order to increase the number of selected events, jets are selected in a range of pseudorapidity of $|\eta| < 3$ and $p_{\mathrm{T}} > 25$ GeV.

Selected events must contain one electron-muon pair with $m_{e\mu} > 20$ GeV and at least two selected jets. In order to avoid reducing the size of the sample, no b tagging requirements are done. Dedicated efficiency corrections are derived for this analysis, taking into account the low luminosity conditions, with a PU profile different from other data-taking periods in the Run 2.

The DY and nonprompt lepton backgrounds are estimated from data, with the methods described in sections 5.3.5.2 and 5.3.5.1, respectively. In this analysis, given that no b tagging selection is required, the dominant background contribution comes from DY events. The contribution from $\mathrm{t\bar{t}Z}$, $\mathrm{t\bar{t}W}$ and ZZ processes are not taken into account in this analysis, as they are expected to be negligible. The purity of $\mathrm{t\bar{t}}$ events in the final sample is lager than 80%.

The uncertainty of this measurement is highly dominated by the large statistical uncertainty due to the small size of the sample. The systematic uncertainties, estimated using conservative approaches in most of the cases, are the lepton efficiencies, $\mathrm{t\bar{t}}$ modelling uncertainties and the DY background estimate.

In figure 5.21 the data and MC distributions of the jet multiplicity and H_{T} after the dilepton selection, and the distributions of the dilepton p_{T} and invariant mass after requiring two jets are shown.

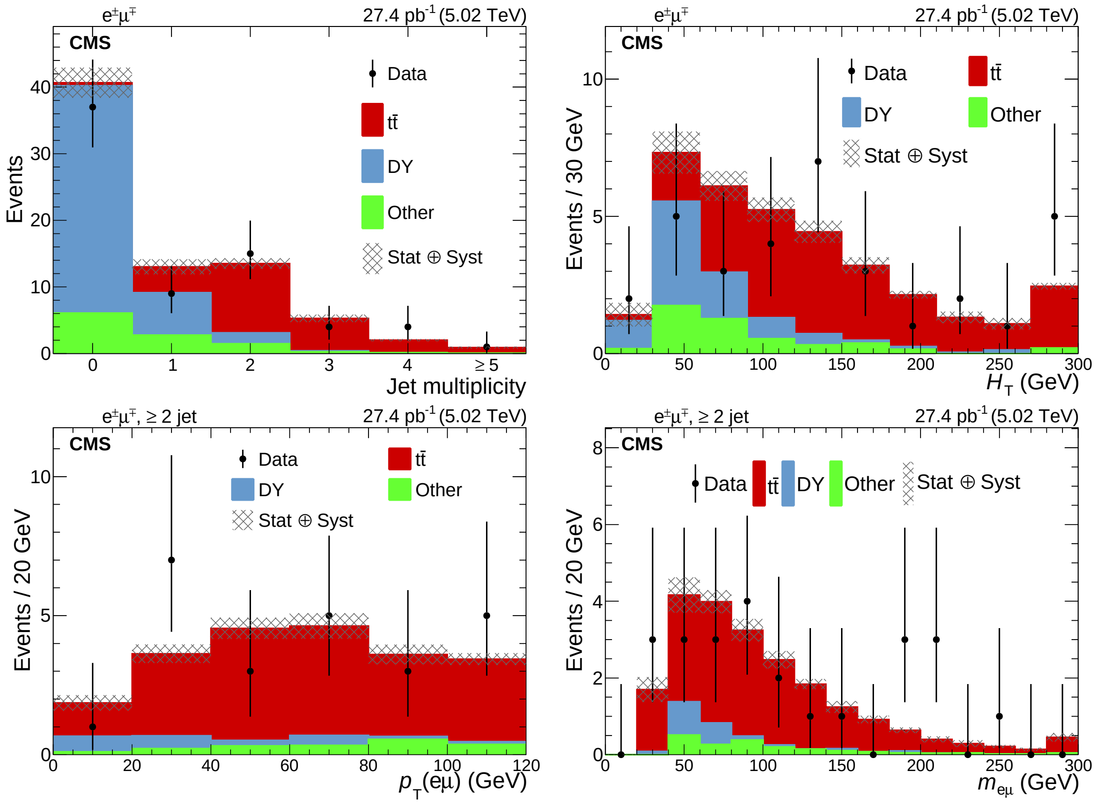

FIGURE 5.21: Distributions of the number of jets (upper left) and H_T (upper right) for expected and observed events containing an $e^{\pm}\mu^{\mp}$ pair and distributions of the dilepton p_T of the $e^{\pm}\mu^{\mp}$ pair (lower left) and the invariant mass of the leptons (lower right) for expected and observed events containing an $e^{\pm}\mu^{\mp}$ pair and at least two jets. The error bands represent statistic and experimental uncertainties. The last bin includes the overflow.

5.4.3 The $\mu^+\mu^-$ channel

The main difference between the $t\bar{t}$ cross section measurement in the $\mu^+\mu^-$ and $e^{\pm}\mu^{\mp}$ channels is the overwhelming amount of DY background events in the former. Extra selection requirements are applied to reject DY events. Furthermore, the branching ratio of $t\bar{t}$ events into the $\mu^+\mu^-$ final state is about half the one into the $e^{\pm}\mu^{\mp}$ channel. Due to this difference of the branching ratio and the extra selection requirements, the number of expected $t\bar{t}$ events in this channel is very low and its contribution to the combined measurement is limited.

A Z-veto cut defined as $|m_{\mu\mu} - m_Z| > 15\,\text{GeV}$ is applied, coinciding with the selection requirement described in section 5.3.5.2, used for the DY data-driven estimate. This requirement rejects most of the DY background events. However, the DY background is still larger than the expected $t\bar{t}$ contribution after this requirement.

To further reduce the number of DY events, a extra cut on the $p_{\mathrm{T}}^{\mathrm{miss}}$ of the event is set. The total amount of $p_{\mathrm{T}}^{\mathrm{miss}}$ in DY events is expected to be close to zero (although it is usually different from zero because of resolution effects of the detector). The observed and MC expected $p_{\mathrm{T}}^{\mathrm{miss}}$ distribution for dimuon events after the Z-veto cut is shown in figure 5.22.

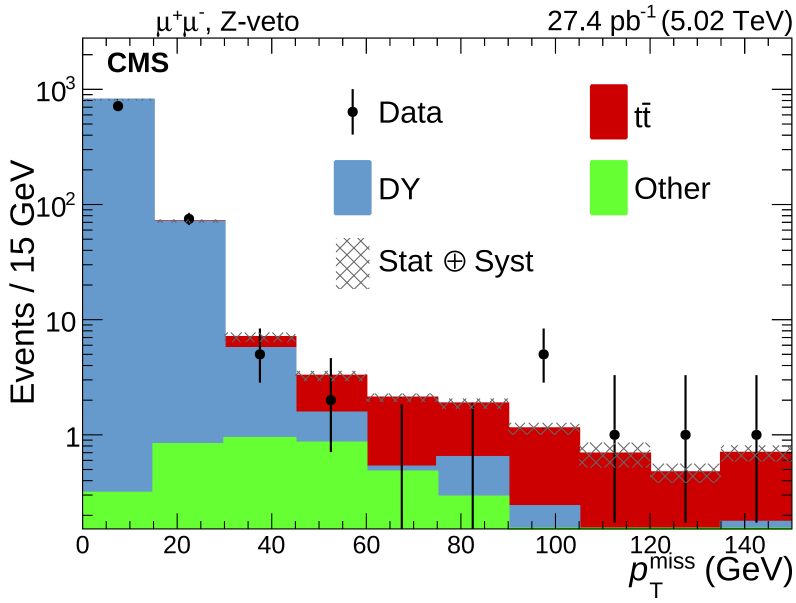

FIGURE 5.22: Distribution of the $p_{\mathrm{T}}^{\mathrm{miss}}$ for expected and observed events containing a $\mu^+\mu^-$ pair after the Z-veto cut. The error bands represent statistic and experimental uncertainties. The last bin includes the overflow.

The cut on $p_{\mathrm{T}}^{\mathrm{miss}}$ is optimised to avoid reducing the number of $\mathrm{t\bar{t}}$ events below the 80% with respect to the expected events before this cut. A ROC curve for the efficiency of the $p_{\mathrm{T}}^{\mathrm{miss}}$ cut for DY and $\mathrm{t\bar{t}}$ events is shown in figure 5.23. A value of 35 GeV is chosen, with a $\mathrm{t\bar{t}}$ selection efficiency of about 80% and rejecting 99% of the DY events.

Finally, the observed and expected $m_{\mu\mu}$ distributions for the selected dimuon events after the Z-veto and $p_{\mathrm{T}}^{\mathrm{miss}} > 35\,\mathrm{GeV}$ cuts are shown in figure 5.24.

5.4.4 Results

After the full event selection, 24 and 7 events are observed in the $e^{\pm}\mu^{\mp}$ and $\mu^+\mu^-$ channels, respectively. The number of observed and predicted events after the selection is shown in table 5.11.

A summary of the uncertainties on the measurements if the $e^{\pm}\mu^{\mp}$ and $\mu^+\mu^-$ channels is shown in table 5.12. The total relative uncertainties are 25% and 52% for the $e^{\pm}\mu^{\mp}$

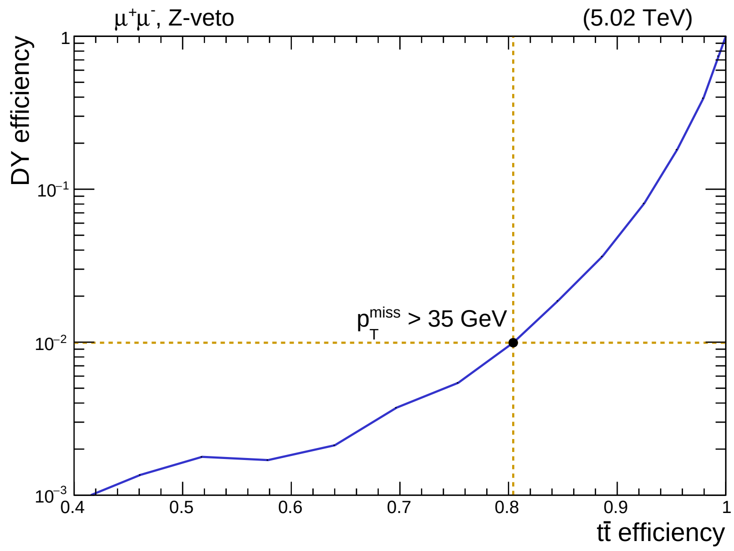

FIGURE 5.23: ROC curve of $p_{\mathrm{T}}^{\mathrm{miss}}$ for $\mathrm{t\bar{t}}$ and DY selection efficiencies. The selected operating point corresponds to $p_{\mathrm{T}}^{\mathrm{miss}} > 35\,\mathrm{GeV}$.

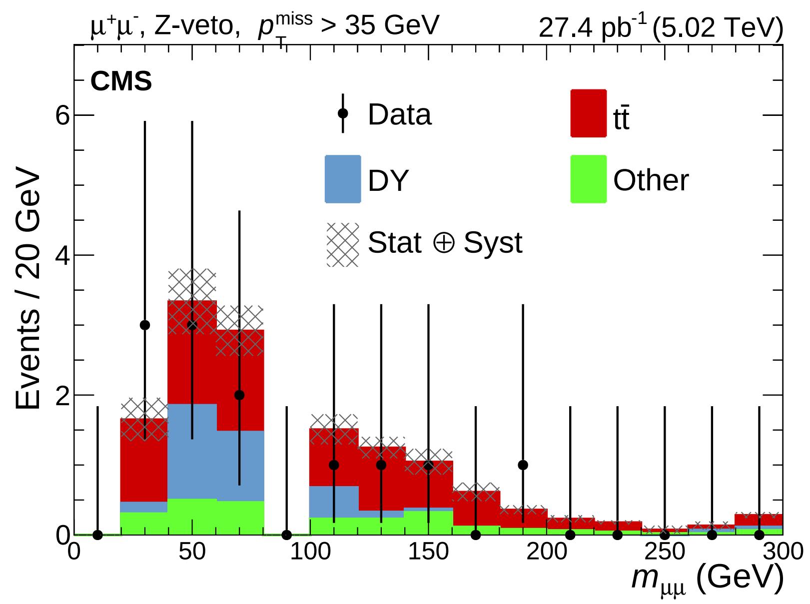

FIGURE 5.24: Distribution of the invariant mass of the $\mu^{+}\mu^{-}$ pair for expected and observed events after the Z-veto and $p_{\mathrm{T}}^{\mathrm{miss}} > 35\,\mathrm{GeV}$ cuts. The error bands represent statistic and experimental uncertainties. The last bin includes the overflow.

Source	$e^{\pm}\mu^{\mp}$	$\mu^{+}\mu^{-}$
Drell-Yan	1.6 ± 0.2	1.1 ± 0.8
Nonprompt leptons	1 ± 0.9	0.04 ± 0.01
tW	0.92 ± 0.02	0.29 ± 0.01
WW + WZ	0.44 ± 0.02	0.15 ± 0.01
Total background	4.0 ± 0.9	1.6 ± 0.8
$\mathrm{t\bar{t}} \rightarrow \ell\ell$	18.0 ± 0.3	6.4 ± 0.2
Data	24	7

TABLE 5.11: Number of observed and expected events for the final selection in the $e^{\pm}\mu^{\mp}$ and $\mu^{+}\mu^{-}$ channels. The quoted uncertainties on the yields correspond to statistical and systematic uncertainties.

and $\mu^{+}\mu^{-}$ channels, respectively. The measured values of the inclusive cross section are

$$\sigma_{\mathrm{t\bar{t}}}(e^{\pm}\mu^{\mp}) = 77 \pm 19\,(\mathrm{stat}) \pm 4\,(\mathrm{syst}) \pm 2\,(\mathrm{lum})\,\mathrm{pb}$$

for the $e^{\pm}\mu^{\mp}$ channel and

$$\sigma_{\mathrm{t\bar{t}}}(\mu^{+}\mu^{-}) = 59 \pm 29\,(\mathrm{stat}) \pm 11\,(\mathrm{syst}) \pm 1\,(\mathrm{lum})\,\mathrm{pb}$$

for the $\mu^{+}\mu^{-}$ channel. Both measurements are in agreement with the SM prediction, shown in equation (5.10). These measurements are further combined with a measurement in the lepton+jets channel. The combined measurement gives a total cross section of

$$\sigma_{\mathrm{t\bar{t}}}(\mathrm{combination}) = 69.5 \pm 6.1\,(\mathrm{stat}) \pm 5.6\,(\mathrm{syst}) \pm 1.6\,(\mathrm{lum})\,\mathrm{pb}$$

corresponding to a relative uncertainty of 12%. The weights of the individual measurements in the combination are 81.8% for e/μ+jets, 13.5% for $e^{\pm}\mu^{\mp}$, and 4.7% $\mu^{+}\mu^{-}$ channels.

5.5 Summary

In this chapter, different $\mathrm{t\bar{t}}$ cross section measurements in pp collisions at $\sqrt{s} = 13\,\mathrm{TeV}$ are presented. A first measurement performed using a small amount of data, corresponding to $42 \pm 5\,\mathrm{pb}^{-1}$ [3], shows a good agreement of the observed and predicted cross sections. More precise measurements are done using luminosities of $2.2\,\mathrm{fb}^{-1}$ [4]

	$e^{\pm}\mu^{\mp}$		$\mu^{+}\mu^{-}$	
Source	$\Delta\sigma_{t\bar{t}}/\sigma_{t\bar{t}}$ (%)	$\Delta\sigma_{t\bar{t}}$ (pb)	$\Delta\sigma_{t\bar{t}}/\sigma_{t\bar{t}}$ (%)	$\Delta\sigma_{t\bar{t}}$ (pb)
Electron efficiencies	1.4	1.0	—	—
Muon efficiencies	3.0	2.3	6.1	3.6
JES	1.3	1.0	1.3	0.7
JER	< 0.1	< 0.1	< 0.1	< 0.1
Missing transverse momentum	—	—	0.7	0.4
PS	1.2	0.9	1.7	1.0
μ_R, μ_F scales of $t\bar{t}$ signal	0.2	0.1	1.1	0.6
Hadronization model of $t\bar{t}$ signal	1.2	0.9	5.2	3.1
PDF+α_S	0.5	0.4	0.4	0.2
MC sample size	1.4	1.1	2.4	1.4
tW	1.4	1.1	1.6	0.9
WW + WZ	0.7	0.5	0.9	0.5
DY	2.7	2.1	15	9.1
Nonprompt leptons	2.5	1.9	0.7	0.4
Total systematic	5.8	4.4	18	11
Integrated luminosity	2.3	1.8	2.3	1.4
Statistical uncertainty	25	19	48	29
Total	25	19	52	31

TABLE 5.12: Summary of the individual contributions to the uncertainties on the $t\bar{t}$ cross section measurement in the $e^{\pm}\mu^{\mp}$ and $\mu^{+}\mu^{-}$ channels. .

and 35.9 fb^{-1} [6], reaching a better precision that the most accurate $t\bar{t}$ cross section predictions.

The $t\bar{t}$ cross section is measured at $\sqrt{s} = 5.02\,\text{TeV}$ for the first time, obtaining a good agreement with respect to the SM prediction. The measurements in the $e^{\pm}\mu^{\mp}$ and $\mu^{+}\mu^{-}$ channels are combined with the lepton+jets channel to obtain a final measurement with a total uncertainty of 12%. These measurements are introduced into a QCD analysis [5], illustrating the potential improvement on our knowledge of the proton PDF.

The $t\bar{t}$ measurements presented in this chapter are shown as a function of $\sqrt{s}$ in figure 7.1. This figure also includes the legacy measurements at $\sqrt{s} = 7$ and 8 TeV, in which I participated with an event-counting analysis as a cross check of the main measurement.

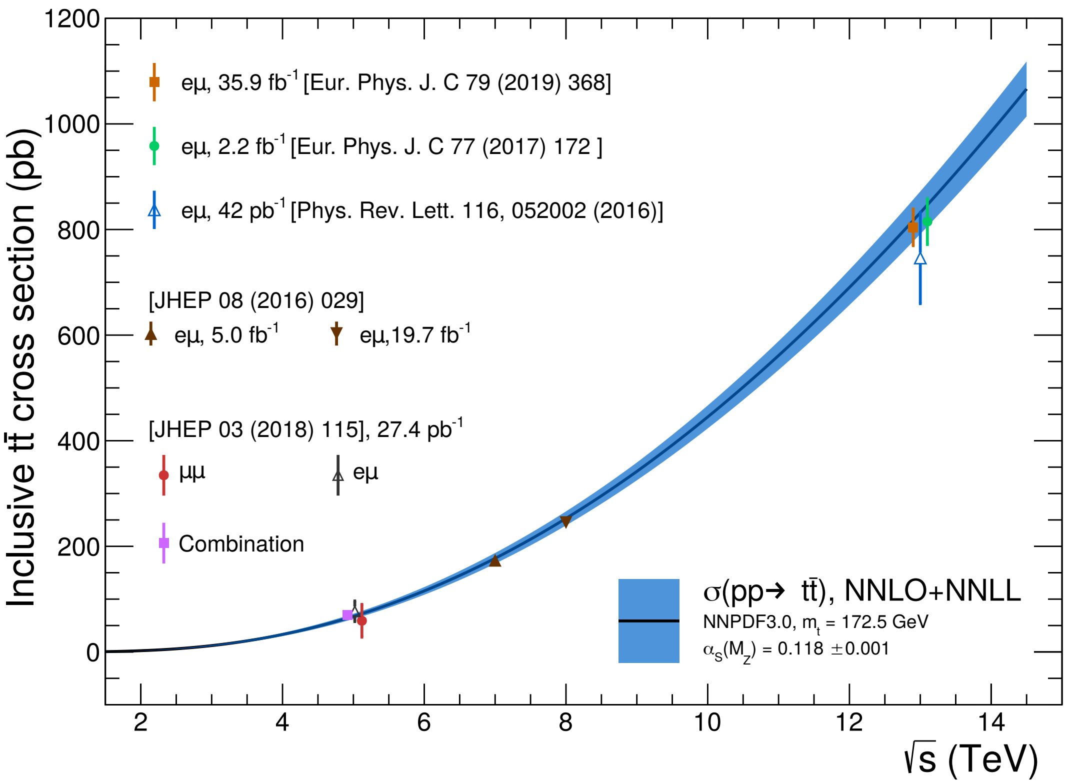

FIGURE 5.25: Summary of the measurements of the $t\bar{t}$ production cross section presented in this thesis as a function of the centre-of-mass energy. The SM predictions were derived using the PDF sets and α_S and m_t values indicated in the plot [70].

Chapter 6

Search for supersymmetric partners of the top quark

6.1 Introduction

Supersymmetry is probably the most popular BSM theory. Since the discovery of the Higgs boson, its search became one of the main goals for the ATLAS and CMS collaborations, especially at the beginning of the Run 2, when a new energy regime was explored for the first time: pp collisions at $\sqrt{s} = 13\,\text{TeV}$. At this centre-of-mass energy a wide range of the SUSY spectra was expected to become available. All the data collected during the Run 2 and the data that will be collected in the next years will allow physicists to explore most of the corners of the SUSY spectra up to masses of the SUSY particles up to about 2 TeV.

In this thesis a search for the production of a pair of the scalar partner of the top quark (stop quarks or top squarks, $\tilde{\mathrm{t}}_1$) and neutralinos ($\tilde{\chi}^0_1$) that are degenerate or nearly degenerate in mass with the top quark is presented. Stop quarks are mainly produced in pairs and, in this search, stop quarks are assumed to decay as $\tilde{\mathrm{t}}_1 \rightarrow \mathrm{t}\tilde{\chi}^0_1$, as shown in figure 6.1.

The search for stops with a mass close to m_{t} is well motivated by naturalness arguments of SUSY theories, as explained in section 6.2. From the experimental point of view, this SUSY process leads to final states very similar to the ones given by SM $\mathrm{t\bar{t}}$ production. Given that the target SUSY signal and the SM top quark pair production processes are characterised by equivalent final states with very similar kinematics, most of the top squark searches by the ATLAS [88–92] and CMS [93–100] collaborations do not have enough sensitivity for observing the production of top squarks in

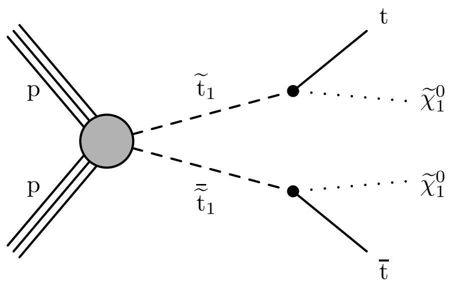

FIGURE 6.1: Diagram of the top squark pair production with further decay into a $t\bar{t}$ pair and two neutralinos.

these scenarios. The summary of stop exclusion limits by CMS is shown in figure 6.2, where the exclusion limits at 95% confidence level (CL) is shown for various CMS analysis as a function of the stop quark mass and neutralino mass. The target region of the analysis presented in this chapter is not excluded by any of the CMS searches.

As discriminating signal from $t\bar{t}$ events is almost impossible, sensitivity to the presence of new physics can be reached by an accurate measurement of the $t\bar{t}$ production cross section. The strategy followed in this search to estimate the SM $t\bar{t}$ background follows closely the one presented in section 5.3 to measure the $t\bar{t}$ cross section at $\sqrt{s} = 13\,\text{TeV}$. Limits on the production cross section of signals described by the model in figure 6.1 have previously been set through $t\bar{t}$ production cross section measurements at 8 TeV by the CMS [66] and ATLAS [102, 103] collaborations, excluding the presence of a top squark with a mass of up to 191 GeV for a neutralino mass of 1 GeV.

In the analysis presented here, the full 2016 dataset of pp collisions recorded by CMS, corresponding to an integrated luminosity of 35.9 fb^{-1}, is used. In particular, this analysis uses events in which the resulting top (anti)quark decays into a bottom (anti)quark and a W boson that in turn decays into a lepton and a neutrino. As in the $t\bar{t}$ cross section measurement presented in section 5.3, events in the $e^{\pm}\mu^{\mp}$ channel are selected. This search is published in reference [16].

6.2 Theoretical basis of supersymmetry

Supersymmetry is a theoretical principle that proposes a link between fermions and bosons, postulating the existence of a new fermion for each SM boson and a new boson for each SM fermion [9–15]. As such particles have not been observed yet, the symmetry between fermions and bosons (supersymmetry) should be broken, and the supersymmetric partners of the SM particles must have larger masses.

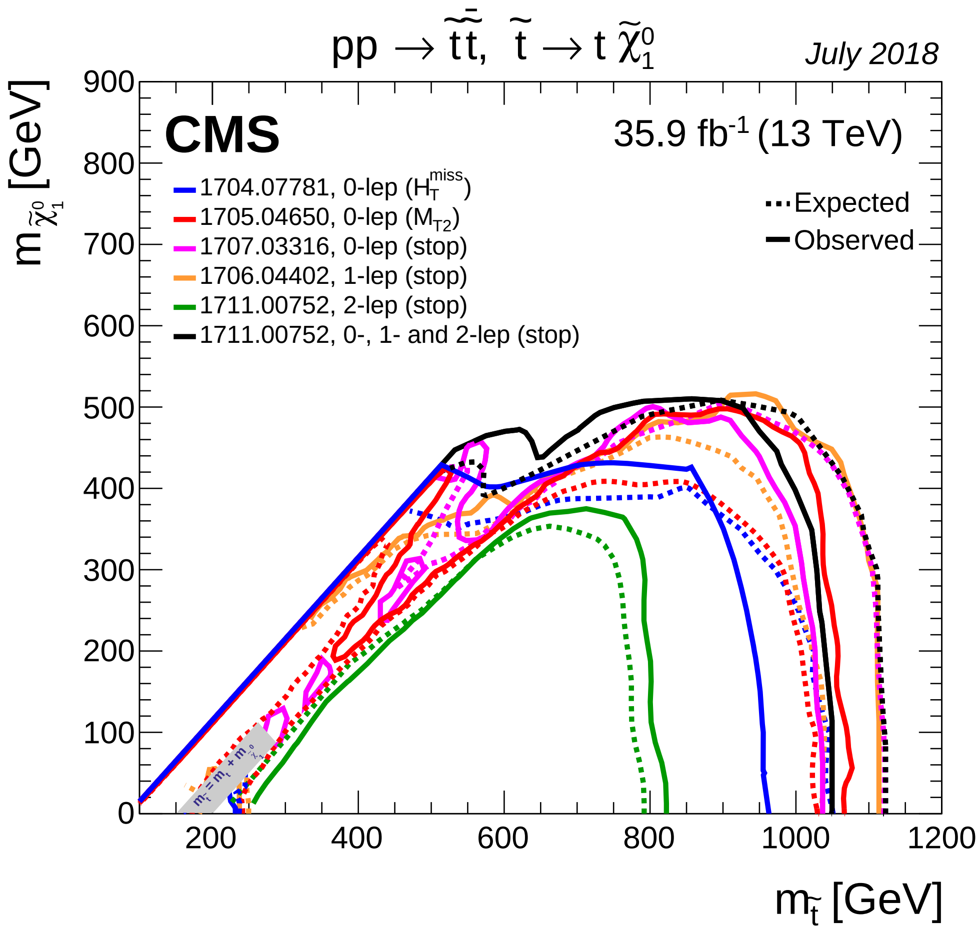

FIGURE 6.2: Mass limits for a simplified model of stop quark pair production with stop decays to an on- or off-shell top quark and the lightest neutralino, leading to final states with two bottom quarks, two W bosons, and two neutralinos [101]. The rectangle drawn in the degenerate region reflects the imposibility of having any information on the exclusion limits in this region from the analysis presented in the figure.

There are several models constructed under this principle. The minimal extension of the SM that introduces SUSY is called Minimal Supersymmetric Standard Model (MSSM) [104]. The particle spectrum of this model duplicates the one from the SM (with the exception of containing 5 supersymmetric partners of the Higgs boson) and contains 125 free parameters.

The supersymmetric partners of the SM fermions (sfermions) are named adding an "s" before the name of their SM partners, while the partners of the SM bosons are called with the suffix "-ino". In this model, the bosinos are combined to form two charged and four neutral flavour eigenstates called charginos and neutralinos respectively. A new quantum number called R-parity is introduced. It is 1 for SM particles and -1 for their SUSY partners. The R-parity is conserved in the MSSM.

The idea of supersymmetry has become very popular because it solves several SM problems. In particular, SUSY solves the hierarchy problem in a natural way [104, 105]. The SUSY solution to the hierarchy problem is discussed in section 6.2.1. Furthermore, the introduction of SUSY particles to the calculation of the running of the coupling constants predicts the unification of the strong and electroweak forces at some energy scale [106–108]. Also, the R-parity conservation implies that the lightest SUSY particle (LSP) is stable. In most SUSY models, the LSP is the lightest neutralino. This particle is a WIMP and thus a good DM candidate, as explained in section 2.3.2.

The interpretation of SUSY searches are based on simplified models [109, 110], in which most of the 125 free parameters are fixed and a few parameters (typically the masses of some particles) are scanned. In this chapter, a simplified model is used to interpret the results.

6.2.1 Solution to the hierarchy problem and naturalness

The quadratic divergences on the renormalisation of the Higgs boson mass, exposed in section 2.3.1, is one of the main arguments to search for BSM physics. Supersymmetry solves this SM problem by introducing new terms to the quadratic corrections of the Higgs mass. The femionic loops of the SM particles contribute as m_{f}^2 to the term in Λ^2, where m_{f}^2 is the squared mass of the fermion. In SUSY, the bosonic partners of the SM bosons add negative contributions proportional to $m_{\tilde{\mathrm{f}}}^2$, where $m_{\tilde{\mathrm{f}}}^2$ is the squared mass of the SUSY partner of the SM fermions. Taking into account these new terms, the 1-loop corrections run over all the fermions and their SUSY partners, as shown in figure 6.3.

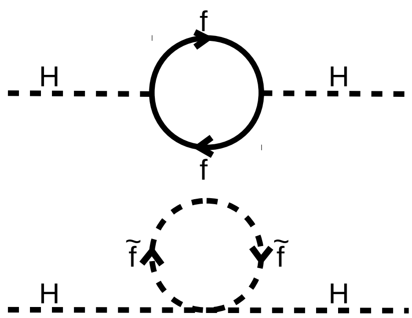

FIGURE 6.3: One-loop diagrams contributing to the renormalisation of the Higgs mass of the corrections due to a fermion loop (upper) and its SUSY partner (lower).

Taking into account the terms introduced by SUSY particles, the qudratically-divergent term in Λ^2 in equation (2.35) cancels out and the residual correction is proportional to the difference of the squared masses of SUSY and SM particles as

$$\Delta m_{\mathrm{H}} \sim \left(m_{\tilde{\mathrm{f}}}^2 - m_{\mathrm{f}}^2\right). \tag{6.1}$$

If SUSY were an exact symmetry, the mass of the supersymmetric particles would be the same as the one of the SM particles and the cancellation of the terms in equation (6.1) would be perfect, leading to a natural solution of the problem. However, the mass of the SUSY partners is larger than the masses of the SM particles (otherwise, they would have been already observed) but the solution is still natural (i.e. needs low levels of parameter tuning) if the masses of the SUSY particles are close to the ones of the SM particles: $|m_{\tilde{\mathrm{f}}}^2 - m_{\mathrm{f}}^2| \lesssim 1\,\mathrm{TeV}^2$ [111]. This argument is used to justify (from the theoretical point of view) the SUSY searches at the LHC.

The largest contribution from SM particles comes from the top quark, as it is by far the most massive fermion. A natural SUSY solution would have a stop with a mass close to that of the top quark. On the other hand, the stop quark is the lightest squark in some SUSY scenarios, so might be the first to be observed.

6.3 Search strategy

In this analysis, the top squark signal and the $\mathrm{t\bar{t}}$ process have very similar final states. The object definition and event selection are the same as the one described in sections 5.3.2 and 5.3.3. Events containing an $e^{\pm}\mu^{\mp}$ pair, at least two jets and at least one b-tagged jet are selected. As we have seen in the previous chapter, the vast majority of the expected SM events after this event selection (≈98%) comes from top quark production processes ($\mathrm{t\bar{t}}$, tW).

The challenge of this analysis consists on precisely estimate the overwhelming top quark background, so the signal can be detected as a deviation of the SM prediction. The expected signal cross section decreases with the mass of the $\tilde{\mathrm{t}}_1$ ($m_{\tilde{\mathrm{t}}_1}$). For $m_{\tilde{\mathrm{t}}_1} = 175\,\mathrm{GeV}$, it amounts to 125 pb, corresponding to about 15% of the SM $\mathrm{t\bar{t}}$ production cross section. This cross section decreases down to ≈ 24 pb for $m_{\tilde{\mathrm{t}}_1} = 245\,\mathrm{GeV}$. Taking into account that the acceptance of the selection for signal and $\mathrm{t\bar{t}}$ events is similar, the background estimate must be precise enough to appreciate the presence of such a small signal.

The background estimation follows the $\mathrm{t\bar{t}}$ cross section measurement presented in chapter 5. The top quark background is estimated using MC simulation and exploiting the 6% theoretical uncertainties on the predicted cross section ([71], equation (5.2)) and the even smaller experimental uncertianties on the measurement ([4, 66], section 5.3.7). The details of the $t\bar{t}$ background estimate are given in section 6.4.

Additional sensitivity comes from the small kinematic differences between the target signal and the $t\bar{t}$ background, which become more important with increasing top squark mass and increasing mass difference between the top squark and neutralino. In particular, the presence of massive neutralinos in the event can result in additional $p_{\mathrm{T}}^{\mathrm{miss}}$. The sensitivity to the signal due to the large $p_{\mathrm{T}}^{\mathrm{miss}}$ in the event becomes dominant when the mass of the neutralino ($m_{\tilde{\chi}_1^0}$) is larger than about 50 GeV. To account for this, following previous top squark searches [96], the sensitivity of the analysis is further increased by using the shape of the m_{T2} variable, defined as

$$m_{\mathrm{T2}} = \min_{\vec{p}_{\mathrm{T},1}^{\mathrm{miss}} + \vec{p}_{\mathrm{T},2}^{\mathrm{miss}} = \vec{p}_{\mathrm{T}}^{\mathrm{miss}}} \left(\max \left[m_{\mathrm{T}}(\vec{p}_{\mathrm{T}}^{\ell 1}, \vec{p}_{\mathrm{T},1}^{\mathrm{miss}}), m_{\mathrm{T}}(\vec{p}_{\mathrm{T}}^{\ell 2}, \vec{p}_{\mathrm{T},2}^{\mathrm{miss}}) \right] \right), \tag{6.2}$$

where m_{T} is the transverse mass of the muons, and $\vec{p}_{\mathrm{T}1}^{\mathrm{miss}}$ and $\vec{p}_{\mathrm{T}2}^{\mathrm{miss}}$ correspond to the estimated transverse momenta of two neutrinos that are presumed to determine the total $\vec{p}_{\mathrm{T}}^{\mathrm{miss}}$ of the event. The transverse mass is calculated for each lepton-neutrino pair, for different assumptions of the neutrino p_{T}. The computation of m_{T2} is done using the algorithm discussed in reference [112].

The result of the minimisation in the computation of m_{T2} is zero for about one third of the signal events. This value is obtained when the $\vec{p}_{\mathrm{T}}^{\mathrm{miss}}$ is situated between the two leptons in the transverse plane, so there is a solution in which each hypothetical neutrino is aligned with its lepton. In this case, each transverse mass $m_{\mathrm{T}}(\vec{p}_{\mathrm{T}}^{\ell i}, \vec{p}_{\mathrm{T,i}}^{\mathrm{miss}})$ is zero, so $m_{\mathrm{T2}} = 0$ is obtained for the event. Since these cases do not provide any discrimination between signal and $t\bar{t}$ background, only events with $m_{\mathrm{T2}} > 0$ GeV are selected.

For $t\bar{t}$ events, if $\vec{p}_{\mathrm{T}}^{\mathrm{miss}}$ and the leptons are well measured, one of the possible hypothesis for the neutrinos would match with the "real" $p_{\mathrm{T}}^{\mathrm{miss}}$ of the neutrinos in the event. In this case, the transverse mass of each lepton-neutrino pair would correspond to the transverse mass of the W boson, whose distribution has an endpoint at the W mass. As a consequence, the largest value of m_{T2} for $t\bar{t}$ events would be m_{W}. This value corresponds to the kinematic endpoint of the m_{T2} distribution. On the other hand, for signal events the missing energy of the neutralinos contribute to the $\vec{p}_{\mathrm{T}}^{\mathrm{miss}}$ of the event and then the case of the hypothetical neutrinos in the m_{T2} computation matching the real ones may not be possible, so no kinematic endpoint is found in the m_{T2} distribution for these events.

Figure 6.4 shows the m_{T2} distributions for signal with different mass hypotheses for the stop squark and neutralino, and background. The m_{T2} distributions of the simulated signal models are characterised by a large difference for $m_{T2} > m_W$, because of the presence of the endpoint in the m_{T2} distribution for $t\bar{t}$ events, which increases significantly when $\Delta m = m_{\tilde{t}_1} - m_{\tilde{\chi}^0_1}$ is different from the top quark mass (figure 6.4 left). Furthermore, the differences in m_{T2} are large for signal points characterised by large neutralino masses, which have additional p_T^{miss} to the event (keeping $\Delta m \approx m_t$, figure 6.4 right).

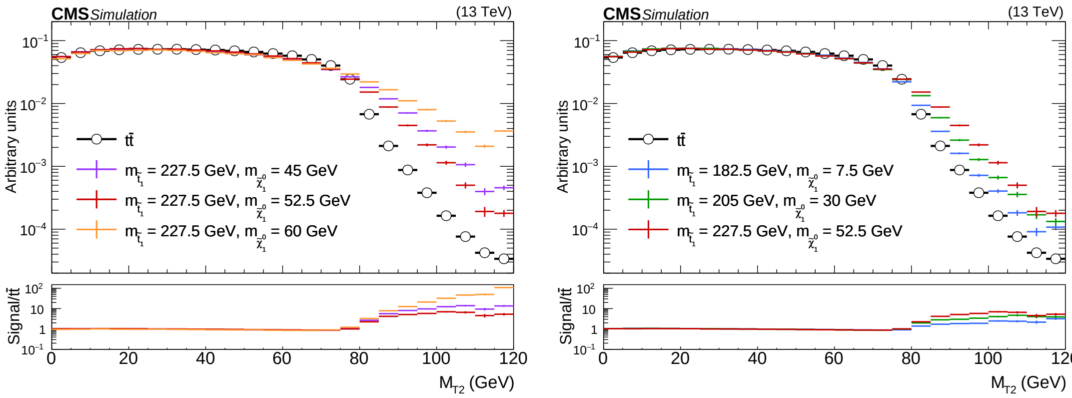

FIGURE 6.4: Normalised m_{T2} distributions for various mass hypotheses for the top squark and for the neutralino. Variables at the generator level are used for $t\bar{t}$ and signal events with two generated leptons with p_T of at least 20 GeV and $|\eta| \leq 2.4$. The last bin includes the overflow.

The resolution effects of the reconstruction of the p_T^{miss} of the event would affect the m_{T2} distribution. Therefore, a small $t\bar{t}$ background is expected at high m_{T2} values.

6.3.1 Signal MC simulation and normalisation

The T2tt model from the simplified model spectra [109, 110] is used to model the SUSY signal, in which top quarks are polarised and a branching fraction of 100% is assumed for the stop quark decaying into a top quark and a neutralino. The generation of signal samples is performed using the MADGRAPH generator at LO [42].

The signal events are normalised to the theoretical NLO cross section [113–118] obtained from the simplified model spectrum for the T2tt model.

The NNPDF 3.0 [22] set of PDF is used in the signal MC simulation. The parton showering and hadronization are handled by PYTHIA v8 using the CUETP8M1 [79] tune for the UE. As for the rest of the simulation of background processes, the GEANT4 package is used to simulate the response of the CMS detector. The efficiency corrections exposed in section 5.3.3 are also applied to the SUSY simulation.

6.4 Background estimate

The background from $t\bar{t}$, tW, $t\bar{t}W$, $t\bar{t}Z$, DY and diboson processes, in which at least two prompt leptons are produced from Z or W decays, is determined from MC simulation including all the corrections mentioned in section 5.3.3. The MC samples used in this analysis are described in section 5.3.1.

The $t\bar{t}$ background is estimated from MC as presented in section 5.3.1. This sample is used in the $t\bar{t}$ cross section measurement and is shown to accurately describe the data. The main parameters affecting the $t\bar{t}$ modelling and their associated uncertainties are discussed in section 6.5. The cross sections used to normalise the background yields estimated from MC simulation are shown in table 5.1.

The amount of background events containing nonprompt leptons is estimated following the strategy used for the $t\bar{t}$ cross section measurement, exposed in section 5.3.5.1, but extended to be estimated for each m_{T2} bin. The method is discussed in section 6.4.1.

6.4.1 Nonprompt leptons

Events containing nonprompt leptons are estimated from data using the method exposed in section 5.3.5.1. The expected yield in each bin of the m_{T2} distribution is estimated from SS data using the equation (5.4).

The expected and observed m_{T2} distributions for SS electron-muon events containing at least two jets and at least one b-tagged jet is shown in figure 6.5. The estimate of background events with nonprompt leptons is splitted into the semileptonic $t\bar{t}$ contribution and others. The SS background with prompt leptons is divided into two contributions: charge mismeasurements (charge flips), mainly from dileptonic $t\bar{t}$, and other processes, mainly from $t\bar{t}W$ and $t\bar{t}Z$.

The expected background with an OS pair of leptons containing at least one nonprompt lepton is taking by subtracting to the observed SS data the expected prompt SS distribution and multiplying the resulting distribution by the transfer factor derived in (5.3). The data-driven and MC simulation background expectations for events with nonprompt leptons are shown in figure 6.6. The data-driven yields are above the MC in the full m_{T2} range.

The uncertainties on the nonprompt leptons background prediction come from the uncertainties in the prompt background subtraction, statistical uncertainties from data

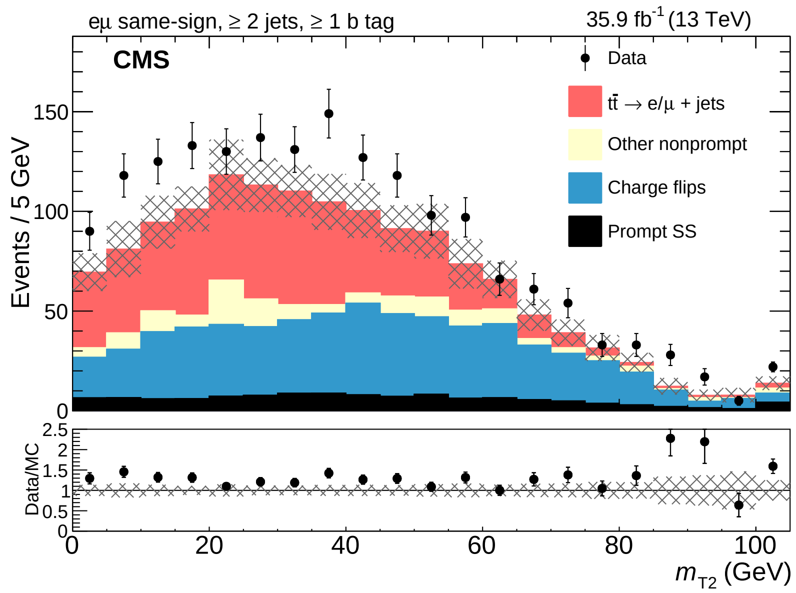

FIGURE 6.5: Distribution of m_{T2} for events containing an $e\mu$ same-sign pair, at least two jets and at least one b-tagged jet. The uncertainties include MC statistics and experimental uncertainties on the MC simulation. The last bin includes the overflow.

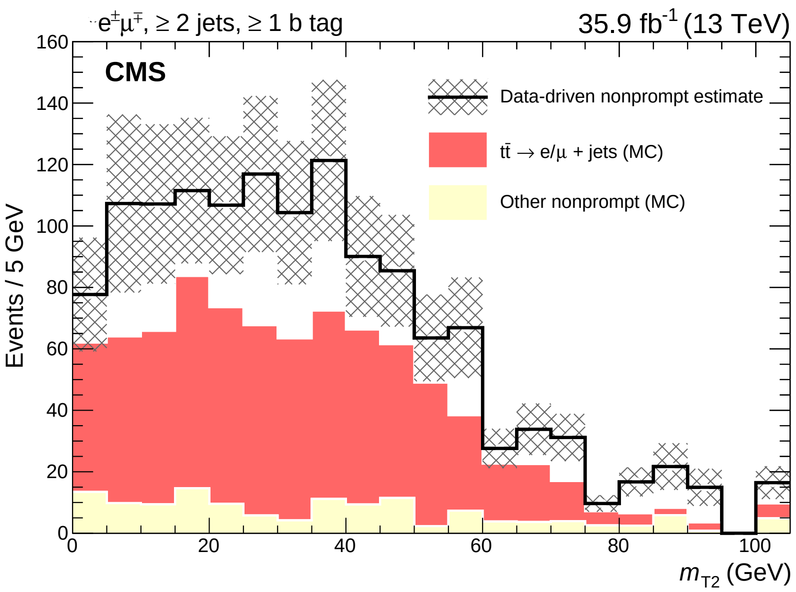

FIGURE 6.6: Distribution of m_{T2} for events after the full event selection. The data-driven prediction is shown with the total (statistics+systematic) uncertainties. The MC prediction is shown as a stack of filled histograms. The last bin includes the overflow.

and statistical uncertainties from the calculation of the transfer factor. The average uncertainty is about 30%, compatible with the results from other CMS searches [119].

6.5 Uncertainties

The experimental uncertainties exposed in section 5.3.7.2 are estimated for every background and signal prediction. The uncertainties are propagated to the expected yield on each bin of the m_{T2} distribution.

The uncertainties on the JES and JER are propagated to the calculation of the $p_{\mathrm{T}}^{\mathrm{miss}}$ of the event. An uncertainty on the unclustered particles contributing to the $p_{\mathrm{T}}^{\mathrm{miss}}$ calculation is also propagated, varying the unclustered energy by the uncertainties associated to each subdetector. The uncertainties on the $p_{\mathrm{T}}^{\mathrm{miss}}$ are propagated to the calculation of m_{T2}. A summary of the effect of the experimental uncertainties on the $\mathrm{t\bar{t}}$ background m_{T2} shape is shown in table 6.1.

Source	Range for $\mathrm{t\bar{t}}$ and signal (%)
Trigger efficiency	≈0.6
Muon efficiencies	≈1.4
Electron efficiencies	≈1.5
Lepton energy scale	0.5–2.0
JES	1.5–3.0
JER	0.3–3.5
b-tagging efficiency	1.2–2.0
Mistag efficiency	0.2–0.6
Unclustered energy	0.5–1.5
PU	0.5–3.5

TABLE 6.1: Summary of the uncertainties in $\mathrm{t\bar{t}}$ background and signal simulation resulting from experimental uncertainties. The numbers represent typical values of the uncertainties in the signal and $\mathrm{t\bar{t}}$ background yields or ranges for these uncertainties in different m_{T2} bins and in different signal samples.

Furthermore, the uncertainty on electron and muon energy scale, which are of about 0.2 to 0.5 GeV for electrons and about 0.1 to 0.4 GeV for muons, are propagated to the m_{T2} computation. These uncertainties are negligible when they are propagated to the total yield, as in the measurement of the $\mathrm{t\bar{t}}$ cross section, but can have a moderate effect of the tails of the m_{T2} distribution, as the edge at m_{W} can be broken if the lepton p_{T} is missmeasured.

The uncertainties on the background normalisation are the same as for the $\mathrm{t\bar{t}}$ cross section measurement, described in section 5.3.7.1. For the $\mathrm{t\bar{t}}$ background, the normalisation uncertainty is taken from the most precise theoretical prediction [70], in equation (5.2). An uncertainty on the top quark MC mass of ± 1 GeV is assumed and propagated to the cross section calculation using the TOP++ 2.0 program [71]. The maximum variation with respect to the nominal value is taken as an uncertainty. The total normalisation uncertainty, including the uncertainties on PDF, μ_R and μ_F, and m_t, is 6%. This uncertainty is propagated to the expected $t\bar{t}$ yields. Moreover, the uncertainty in the integrated luminosity, which affects the signal and background normalisation, is estimated to be 2.5% [81].

The modelling uncertainties shown in 5.3.7.3 are derived for the $t\bar{t}$ background expectation. In this search, the modelling uncertainties are propagated to both the shape and the normalisation of the m_{T2} distribution. On top of the uncertainties described for the $t\bar{t}$ cross section measurement, an uncertainty on the p_T of the generated top quarks is considered. The top quark p_T is known to be slightly mismodelled [72]. A reweighting procedure, based on these studies, has been derived. The factor ω_t to weight the event for each top quark depends on the top quark p_T as $\omega_t = e^{0.0615-0.0005 p_T^t}$, where p_T^t is the p_T of the top quark. This formula is derived to get the generated top quark p_T distribution to match the observed one. This reweighting procedure is not applied for the $t\bar{t}$ background prediction but the difference between the obtained m_{T2} distribution applying and not applying the reweighting is taken as an uncertainty. The effect of the reweighting on the $t\bar{t}$ yields is small and the range of the uncertainty can be seen in table 6.2.

The uncertainty on the signal cross sections for the range of stop masses of this analysis is of the order of 15% [113] and is propagated to the expected signal yields. Following the same procedure as for the $t\bar{t}$ modelling uncertainties, explained in section 5.3.7.3, the uncertainties on the signal acceptance due to the factorisation and renormalisation scales are taken into account by varying μ_R and μ_F by factors 2 and 1/2 both. This uncertainty is propagated to the signal yields, resulting in an uncertainty in each m_{T2} bins of the order of 0.5 to 1.0%.

The MADGRAPH LO modelling of the ISR in signal events is improved by scaling the p_T distribution of the ISR jets in MC simulation, according to a correction derived using $t\bar{t}$ events. The weights applied to each event depend on the number of ISR jets in the event and keep the total normalisation constant. The reweighting is derived following the same procedure described in reference [94], using a MADGRAPH LO $t\bar{t}$ MC sample and comparing with observed data. An uncertainty is applied by considering variations of half the difference between the corrections and unity. The effect of this uncertainty on the signal yields is about 1%, with individual values assigned to each m_{T2} bin.

Source	Range (%)
μ_F and μ_R scales	0.3–1.0
PDF+α_S	≈0.6
ISR	0.5–1.0
FSR	0.6–1.2
ME/PS matching (h_{damp})	0.3–2.0
UE	≈0.8
Colour reconnection	≈1.5
Top quark p_T reweighting	0.1–0.5
Top quark mass (acceptance)	≈1.0

TABLE 6.2: Summary of the uncertainties on the m_{T2} distribution resulting from $t\bar{t}$ background modelling uncertainties. The ranges correspond to variations of the uncertainty along the m_{T2} distribution. When only one number is shown, the uncertainty is approximately constant over the entire m_{T2} range.

6.6 Results

The distributions of the leading and subleading lepton p_T, p_T^{miss}, and the angle between the momentum of the leptons in the transverse plane ($\Delta\phi(e\mu)$) for events after the full selection, including events with $m_{T2} = 0$ GeV, are shown in figure 6.7. These figures include all the experimental and modelling uncertainties described in the previous section. A good agreement between data and SM prediction is observed within the uncertainties. These variables are used to construct m_{T2}.

The predicted and observed m_{T2} distributions for selected events are shown in figure 6.8. No significant deviation from the SM expectation is observed. The integrated number of observed and predicted events, for $m_{T2} > 0$ GeV and $m_{T2} > 90$ GeV, are shown in table 5.9. The number of events with $m_{T2} > 90$ GeV reflects the discriminating power for different stop quark and neutralino masses at high values of m_{T2}.

6.6.1 Interpretation

The SUSY hypothesis is tested against the SM-only hypothesis. A binned profile likelihood fit of the m_{T2} distribution is performed, where the nuisance parameters are modelled using log-normal distributions. The experimental and modelling uncertainties described in section 6.5 are assigned to each m_{T2} bin individually and treated as correlated among all the bins of the m_{T2} distribution and processes. The statistical uncertainties are treated as uncorrelated nuisance parameters in each of the m_{T2} bins. The postfit m_{T2} distribution for background and observed data is shown in figure 6.9.

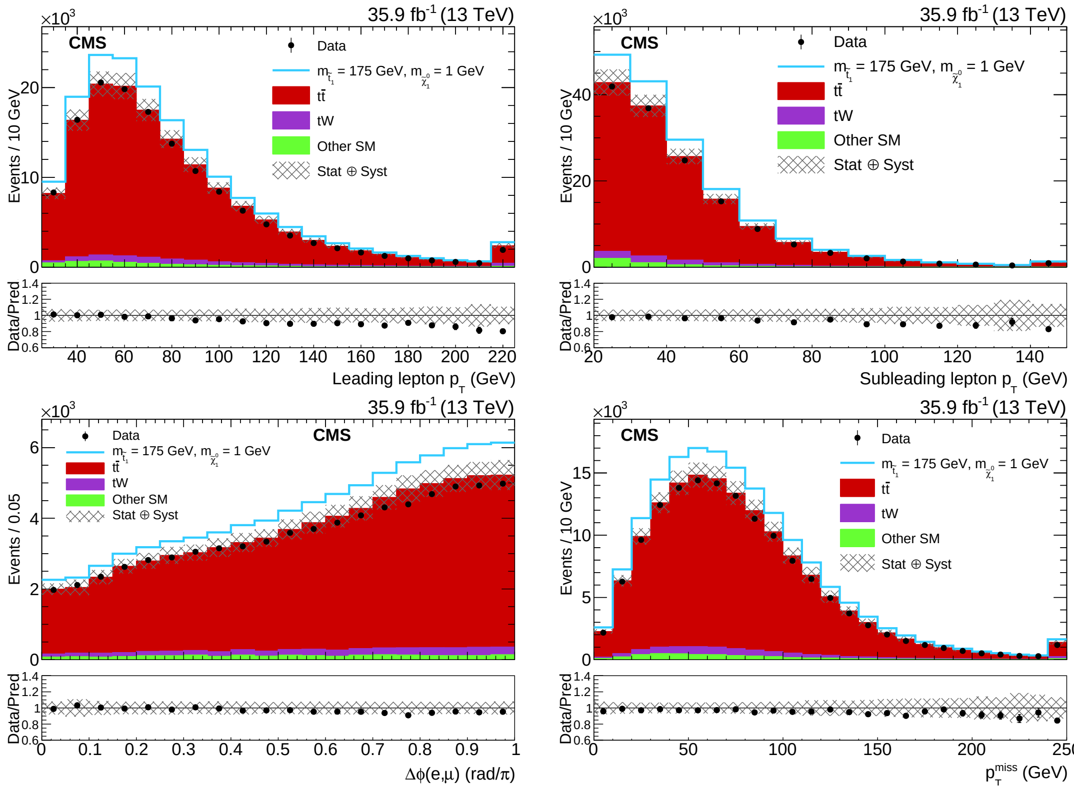

FIGURE 6.7: Distributions for leading and subleading lepton p_T, $\Delta\phi(e, \mu)$, and p_T^{miss}. The uncertainty band includes statistical and all systematic uncertainties described in section 6.5. The last bin contains the overflow events. The signal is stacked on top of the background prediction for a mass hypothesis of $m_{\tilde{t}_1} = 175$ GeV and $m_{\tilde{\chi}^0_1} = 1$ GeV. The lower panel shows the ratio between the observed data and the predicted SM background.

Process	with $m_{T2} > 0$ GeV	with $m_{T2} > 90$ GeV
$t\bar{t}$	$102\,400 \pm 7400$	1680 ± 260
tW	4700 ± 1400	92 ± 32
Nonprompt leptons	1330 ± 400	30 ± 11
DY + $t\bar{t}$V + Dibosons	570 ± 100	19 ± 6
Total Background	$109\,000 \pm 7600$	1821 ± 260
Signal: $m_{\tilde{t}_1} = 175.0$ GeV, $m_{\tilde{\chi}^0_1} = 1.0$ GeV	$16\,400 \pm 2500$	276 ± 53
Signal: $m_{\tilde{t}_1} = 205.0$ GeV, $m_{\tilde{\chi}^0_1} = 22.5$ GeV	8070 ± 1240	232 ± 41
Signal: $m_{\tilde{t}_1} = 205.0$ GeV, $m_{\tilde{\chi}^0_1} = 30.0$ GeV	7830 ± 1200	157 ± 27
Signal: $m_{\tilde{t}_1} = 205.0$ GeV, $m_{\tilde{\chi}^0_1} = 37.5$ GeV	6140 ± 650	262 ± 45
Signal: $m_{\tilde{t}_1} = 242.5$ GeV, $m_{\tilde{\chi}^0_1} = 67.5$ GeV	3550 ± 540	106 ± 19
Data	$105\,893$	1694

TABLE 6.3: Number of expected and observed events after the selection, with $m_{T2} > 0$ and $m_{T2} > 90$ GeV. The quoted uncertainties reflect both the statistical and systematic contributions.

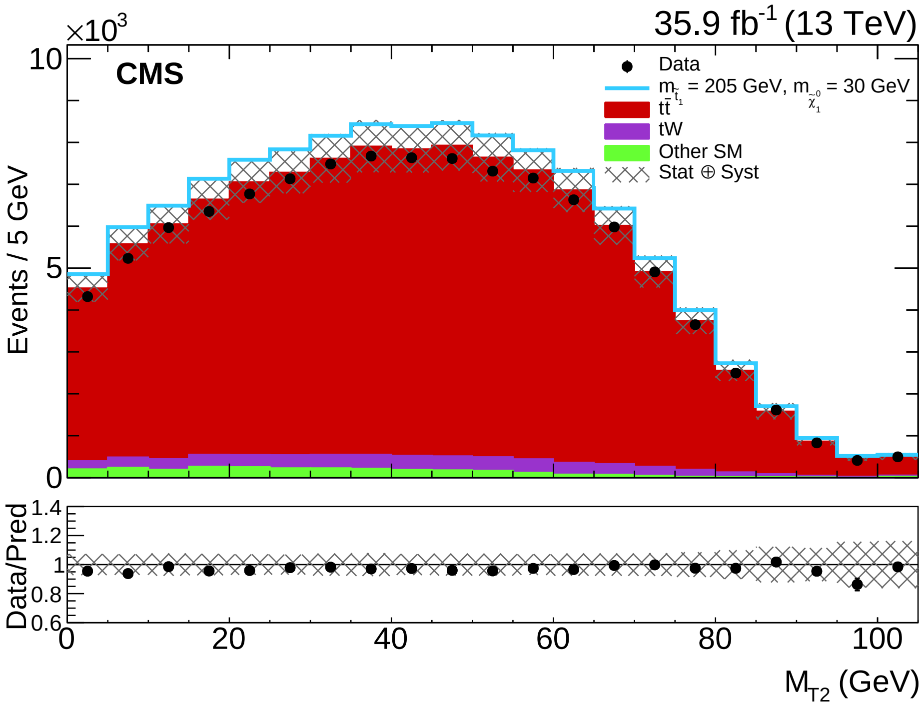

FIGURE 6.8: m_{T2} distribution (prefit) for data and predicted background. The m_{T2} distribution for a signal corresponding to a stop mass of 205 GeV and a neutralino mass of 30 GeV is also shown, stacked on top of the background estimate. The hatched band corresponds to the combined systematic and statistical uncertainties on background rates. The last bin of the histogram includes the overflow events. The lower panel shows the ratio between the observed data and the predicted SM background.

In addition, the results are interpreted for different signal models characterised by stop quark masses from about 170 GeV to 250 GeV and three different mass differences between the stop and the neutralino: $\Delta m(\tilde{t}_1, \tilde{\chi}_1^0) = 167.5$, 175.0, and 182.5 GeV. Upper limits on the stop quark pair production cross section are calculated at 95% CL using a modified frequentist approach, implemented through an asymptotic approximation [120–123]. The uncertainties on background and signal yields are treated as nuisance parameters and profiled in the fit.

The sensitivity of the analysis to SUSY models with low neutralino masses and $\Delta m(\tilde{t}_1, \tilde{\chi}_1^0) = m_t$ comes mostly from the signal normalisation, i.e. from the precision measurement of the $t\bar{t}$ cross section. On the other hand, the differences on m_{T2} shape become important for stop quarks with masses greater than 210 GeV. For the difference in masses of $\Delta m(\tilde{t}_1, \tilde{\chi}_1^0) = 167.5$ and 182.5 GeV, the sensitivity of the analysis is mostly driven by the differences between the signal and $t\bar{t}$ distributions for high m_{T2} values ($> m_W$).

Some of the systematic uncertainties are constrained in fit to the m_{T2} distribution, specially the ones related to the $t\bar{t}$ modeling and normalization. Some of the uncertainties affecting the m_{T2} tail, as the JES, are dominant in the signal extraction for models with

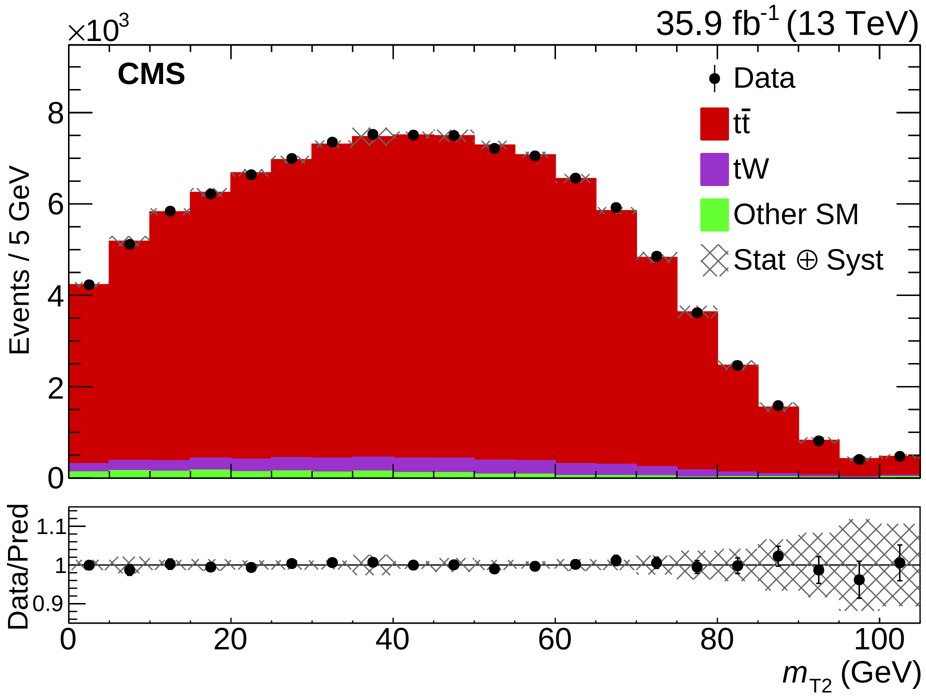

FIGURE 6.9: m_{T2} postfit distribution for data and prediction. The hatched band corresponds to the combined postfit systematic and statistical uncertainties on background rates. The last bin of the histogram includes the overflow events. The lower panel shows the ratio between the observed data and the predicted SM background.

high $m_{\tilde{\chi}_1^0}$. The uncertainty with the largest impact is $\mathrm{t\bar{t}}$ normalization uncertainty. The expected and observed upper limits on the signal strength, defined as the ratio between the excluded and the predicted signal cross sections, are shown in figure 6.10. Under the assumptions of the signal model, stop quark with a mass up to 208 GeV for $\Delta m(\tilde{\mathrm{t}}_1, \tilde{\chi}_1^0) - 175 = 0\,\mathrm{GeV}$ is excluded at 95% CL and up to stop quark masses of 235 (242) GeV for $\Delta m(\tilde{\mathrm{t}}_1, \tilde{\chi}_1^0) - 175 = +(-)7.5\,\mathrm{GeV}$.

6.7 Summary

The existence of a stop quark that counteracts the top quark contribution to the renormalisation of the Higgs boson mass would suppose a natural SUSY solution to the hierarchy problem. Recent searches by the ATLAS and CMS collaborations have excluded the presence of such particle up to $m_{\tilde{\mathrm{t}}_1}$ values of above 1 TeV, while the sensitivity to light stops is limited due to the overwhelming $\mathrm{t\bar{t}}$ background.

The expertise gained on $\mathrm{t\bar{t}}$ physics has allowed us to search for stop pair production in this phase space region, $m_{\tilde{\mathrm{t}}_1} - m_{\tilde{\chi}_1^0} \approx m_{\mathrm{t}}$. The search is performed using events with one opposite-sign electron-muon pair, at least two jets, and at least one b-tagged

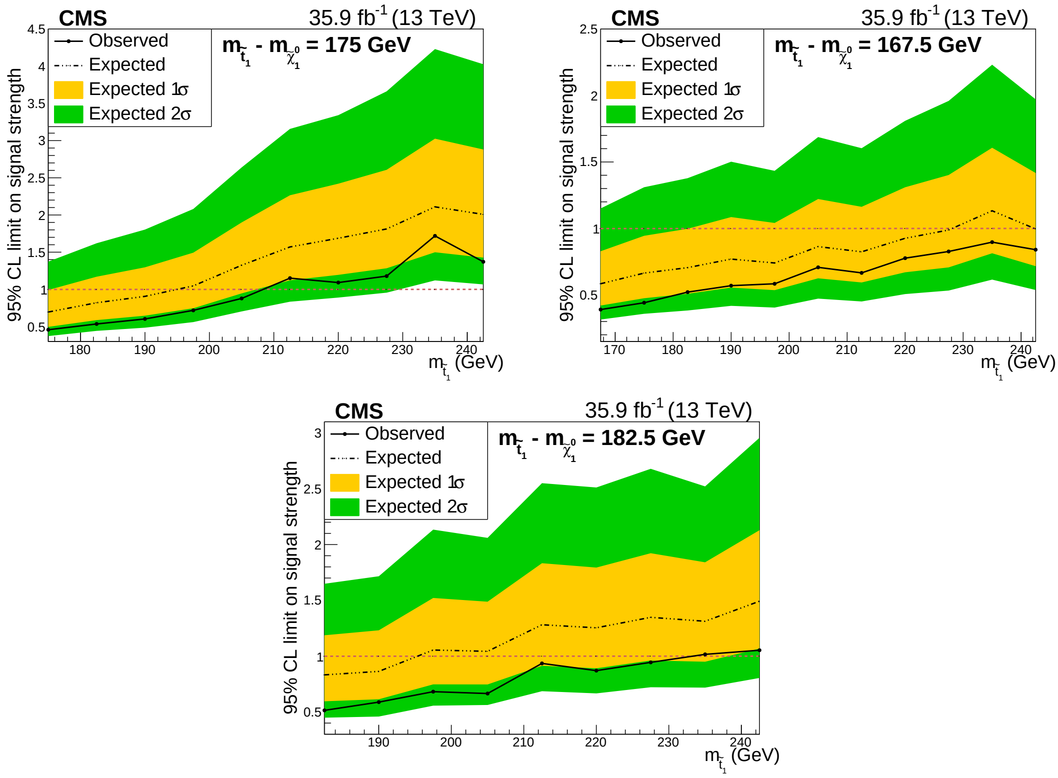

FIGURE 6.10: Expected and observed upper limits at 95% CL on the signal strength as a function of the stop mass for $m_{\tilde{t}_1} - m_{\tilde{\chi}^0_1} = 175\,\text{GeV}$ (upper left), $m_{\tilde{t}_1} - m_{\tilde{\chi}^0_1} = 167.5\,\text{GeV}$ (upper right) and $m_{\tilde{t}_1} - m_{\tilde{\chi}^0_1} = 182.5\,\text{GeV}$ (lower). The green dark and yellow light bands correspond to the 68 and 95% CL ranges of the expected upper limits.

jet. The $\tilde{t}_1 \to t\tilde{\chi}^0_1$ decay mode is considered, and top squark masses are explored up to about 240 GeV. A precise estimation of the SM background allows us to be sensitive to the SUSY hypothesis with light top squarks. The m_{T2} variable is used in a binned profile likelihood fit to increase the sensitivity, due to the different kinematic distributions between the signal and the $t\bar{t}$ background, especially for higher stop masses or larger differences on $|m_{\tilde{t}_1} - m_{\tilde{\chi}^0_1}| - m_t$.

No excess is observed and upper limits are set at 95% confidence level on the stop quark production cross section for $m_{\tilde{t}_1}$ up to 208 GeV in models with $m_{\tilde{t}_1} - m_{\tilde{\chi}^0_1} \approx m_t$ and $m_{\tilde{t}_1}$ up to 235 (242) GeV in models with a mass difference of $+$ $(-)$ 7.5 GeV. This result significantly extends the exclusion limits of stop quark searches at the LHC to higher stop masses in the region with a nearly degenerate stop quark.

Chapter 7

Summary and conclusions

This thesis presents results of precision measurements of Standard Model (SM) parameters and a search for supersymmetric particles. The analyses use different datasets of pp collisions recorded during the Run 2 by the CMS detector. Furthermore, the effect of the radiation expected during the future HL-LHC on the performance of the CMS drift tube (DT) chambers was studied with data taken at the CERN Gamma Irradiation Facility (GIF++).

A DT chamber was irradiated inside the GIF++ bunker to a total integrated dose equivalent to twice the one foreseen in the most irradiated CMS DT chambers at the end of the HL-LHC run. In order to characterise the effect of the radiation in the performance of the DT chambers, the hit efficiency was measured regularly during the irradiation period using cosmic muons at several working conditions. Measurements with test beam muons were also performed at several stages of the irradiation period. The analysis shows an expected maximum efficiency drop of 38%. The effect of the ageing is extrapolated to the full DT system, however no significant efficiency loss is expected for the CMS offline muon reconstruction. This study is crucial for an improved design of the trigger strategy at the HL-LHC using DT chambers, to optimize the muon reconstruction algorithms at trigger level, and to plan the operation of the DT system in the following years.

The top quark pair production cross section is measured at two different centre-of-mass energies, 13 TeV and 5.02 TeV, using different LHC running conditions and, in the first case, different datasets. First, the $\mathrm{t\bar{t}}$ cross section is measured using the full 2015 dataset, corresponding to an integrated luminosity of 2.2 fb^{-1} at $\sqrt{s} = 13$ TeV. A precise result is obtained with a value of

$$\sigma_{\mathrm{t\bar{t}}} = 815 \pm 9\,(\mathrm{stat}) \pm 38\,(\mathrm{syst}) \pm 19\,(\mathrm{lum})\,\mathrm{pb},$$

in agreement with the SM prediction of $832^{+20}_{-29}\,(\text{scale}) \pm 35\,(\text{PDF}+\alpha_S)\,\text{pb}$ [70]. The total uncertainty of the measurement is 5.3%, of the order of the theory uncertainties.

After that, the $\text{t}\bar{\text{t}}$ cross section is measured using the full 2016 dataset, corresponding to $35.9\,\text{fb}^{-1}$ of pp collisions at $\sqrt{s} = 13\,\text{TeV}$. In this analysis some of the uncertainties are reduced, obtaining a better precision on the signal efficiency and acceptance. The measured cross section is

$$\sigma_{\text{t}\bar{\text{t}}} = 804 \pm 2\,(\text{stat}) \pm 29\,(\text{syst}) \pm 20\,(\text{lum})\,\text{pb},$$

corresponding to a total uncertainty of 4.2%, better than the best theoretical prediction.

The $\text{t}\bar{\text{t}}$ cross section is also measured at $\sqrt{s} = 5.02\,\text{TeV}$ for the first time, using an integrated luminosity of $27.4\,\text{pb}^{-1}$. The measurement presented in this thesis is the only measurement up to date of the $\text{t}\bar{\text{t}}$ cross section at this centre-of-mass energy. The measurement is first done using events containing an electron-muon pair and at least two jets and further combined with the the measurements in the final states with a dimuon pair and an electron or a muon accompanied by jets. With such a small amount of data and at this relatively low centre-of-mass energy, the uncertainty of the measurement is dominated by the size of the sample. The measured cross section is

$$\sigma_{\text{t}\bar{\text{t}}}(\text{combination}) = 69.5 \pm 6.1\,(\text{stat}) \pm 5.6\,(\text{syst}) \pm 1.6\,(\text{lum})\,\text{pb},$$

in agreement with the SM prediction of $68.9^{+1.9}_{-2.3}\,(\text{scale}) \pm 2.3\,(\text{PDF})^{+1.4}_{-1.0}\,(\alpha_S)\,\text{pb}$ [70], with a total uncertainty of 12%.

A summary of the $\text{t}\bar{\text{t}}$ production cross section measurements by CMS and CDF and D0 as a function of the centre-of-mass energy is shown in figure 7.1. Several points of this graph correspond to measurements presented in this thesis.

Finally, a search for the supersymmetric partners of the top quark (stop) is also presented. In this search, a stop pair decays into top quarks and neutralinos with such a mass that it is nearly degenerate with the SM $\text{t}\bar{\text{t}}$ production. In this scenario, the stop pair production can only be detected as an excess of events over the $\text{t}\bar{\text{t}}$ prediction. Because of this, most of the previous SUSY searches have no sensitivity to this process. The analysis presented here is a dedicated search in which can be taken some advantage from the precision measurement of the $\text{t}\bar{\text{t}}$ production cross secction. Furthermore, the shape of a discriminant observable is used to increase the sensitivity to stop production models in which the mass difference between the stop and neutralino is different from the mass of the top quark.

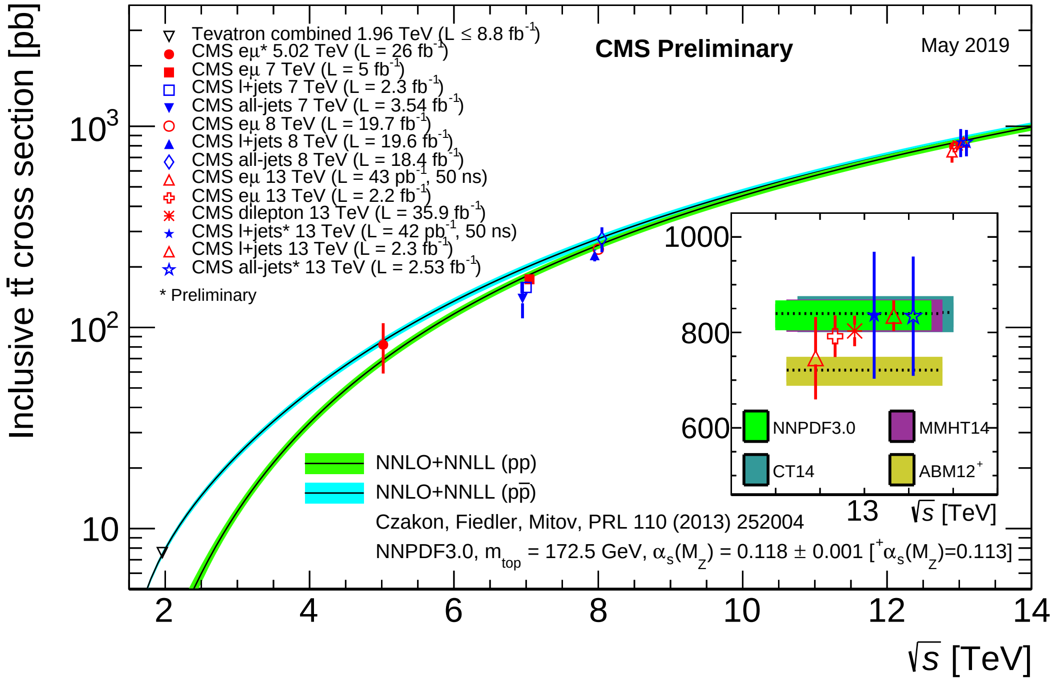

FIGURE 7.1: Summary of the measurements of the $t\bar{t}$ production cross section as a function of the centre-of-mass energy.

Using $35.9\,\text{fb}^{-1}$ of data from 2016 at $\sqrt{s} = 13\,\text{TeV}$, no deviation is observed over the background prediction. Exclusion limits are set at 95% confidence level on the stop quark production cross section for a stop mass up to 208 GeV, under the assumptions taken, in models in which the mass difference between the stop and the neutralino are equal to about the mass of the top quark. This result represents an important step towards covering the phase space where new particles can be found.

To summarise, the results presented in this thesis contribute to increase the knowledge about the most fundamental aspects of nature and to explore the possible extensions of this knowledge by probing the existence of new particles. Furthermore, the studies on the ageing of the DT system contribute to pave the way for working with a new machine that will push the luminosity frontiers.

Chapter 8

Resumen y conclusiones

En esta tesis se presentan los resultados tanto de medidas de precisión del Modelo Estándar (ME) como de una búsqueda de partículas supersimétricas. Para ello, se utilizan diferentes conjuntos de datos de colisiones protón-protón tomados durante el Run 2 por el detector CMS. Además, se presenta una serie de estudios sobre el efecto de la raciación en el rendimiento de las cámaras de deriva de CMS durante el LHC a alta luminosidad, utilizando datos tomados en la Instalación de Irradiación Gamma (GIF++) en el CERN.

Como parte de los estudios de detector para la mejora de CMS en la fase 2, se ha realizado un estudio sobre el rendimiento de las cámaras de muones en función de la radiación absorbida que se espera durante el HL-LHC.

En septiembre de 2017, se introdujo en las instalaciones de GIF++ una cámara similar a las cámaras MB2 de CMS, que fue irradiada hasta acumular una dosis de radiación equivalente al doble de lo esperado para la cámaras más irradiadas al final del periodo de funcionamiento del HL-LHC. Durante la toma de datos, para caracterizar la pérdida de eficiencia de las cámaras se realizaron múltiples medidas de la eficiencia bajo diferentes condiciones de funcionamiento, usando un haz de muones y muones cósmicos. El análisis de los datos muestra una disminución de la eficiencia de hasta 38% para las cámaras más irradiadas al final del periodo de funcionamiento del HL-LHC. Sin embargo, no se espera una pérdida de eficiencia significativa en la reconstrucción de muones en CMS. Este estudio es crucial para poder diseñar la estrategia de trigger utilizando cámaras de muones, optimizar los algoritmos de reconstrucción y planificar la operación del detector en los próximos años.

Por otra parte, se ha presentado la medida de la sección eficaz de producción de quarks top-antitop a diferentes energías en el centro de masas, 13 TeV y 5.02 TeV, usando conjuntos de datos tomados con diferentes condiciones de funcionamiento del LHC durante 2015 y 2016. Primero, la sección eficaz de $\mathrm{t\bar{t}}$ se ha medido usando una pequeña cantidad de datos, correspondiente a $42 \pm 5\,\mathrm{pb}^{-1}$ a $\sqrt{s} = 13\,\mathrm{TeV}$, que fueron tomados durante las primeras semanas del RUN 2. Esta medida no sólo muestra un buen acuerdo entre la predicción del ME y el experimento, sino que también demuestra que el experimento CMS estaba en perfecto funcionamiento, preparado para producir resultados con los datos que se estaban tomando a una energía en el centro de masas nunca antes explorada.

La sección eficaz de $\mathrm{t\bar{t}}$ se ha medido también utilizando el conjunto completo de datos tomados en 2015, que se corresponde con una luminosidad de $2.2\,\mathrm{fb}^{-1}$ a $\sqrt{s} = 13\,\mathrm{TeV}$. El resultado de la medida es

$$\sigma_{\mathrm{t\bar{t}}} = 815 \pm 9\,(\mathrm{stat}) \pm 38\,(\mathrm{syst}) \pm 19\,(\mathrm{lum})\,\mathrm{pb},$$

en acuerdo con la predicción del ME de $832^{+20}_{-29}\,(\mathrm{scale}) \pm 35\,(\mathrm{PDF}{+}\alpha_S)\,\mathrm{pb}$ [70]. La incertidumbre total de la medida es 5.3%, que es del orden de las incertidumbres teóricas.

Finalmente, se ha medido la sección eficaz de $\mathrm{t\bar{t}}$ usando el conjunto entero de datos tomados en 2016, correspondientes a una luminosidad de $35.9\,\mathrm{fb}^{-1}$ a $\sqrt{s} = 13\,\mathrm{TeV}$. En este analisis, se redujeron algunas de las incertidumbres sistemáticas, obteniendo una mejora en la precisión con respecto a las medidas anteriormente expuestas. La medida es

$$\sigma_{\mathrm{t\bar{t}}} = 804 \pm 2\,(\mathrm{stat}) \pm 29\,(\mathrm{syst}) \pm 20\,(\mathrm{lum})\,\mathrm{pb}.$$

con una incertidumbre total de 4.2%, que es mejor que la de predicción teórica más reciente.

La medida de la sección eficaz de $\mathrm{t\bar{t}}$ también se ha llevado a cabo a $\sqrt{s} = 5.02\,\mathrm{TeV}$ por primera y única vez, utilizando una luminosidad integrada de $27.4\,\mathrm{pb}^{-1}$. Esta medida se ha realizado primero usando sucesos con un par electrón-muon y al menos dos jets y posteriormente el resultado ha sido combinado con la medida en los canales $\mu^+\mu^-$ y $e/\mu + \mathrm{jets}$. Con la pequeña cantidad de datos disponibles, la incertidumbre de la medida está dominada por el error estadístico. El resultado es de

$$\sigma_{\mathrm{t\bar{t}}}(\text{combinación}) = 69.5 \pm 6.1\,(\mathrm{stat}) \pm 5.6\,(\mathrm{syst}) \pm 1.6\,(\mathrm{lum})\,\mathrm{pb},$$

en acuerto con la predicción del ME, de $68.9^{+1.9}_{-2.3}\,(\mathrm{scale}) \pm 2.3\,(\mathrm{PDF})^{+1.4}_{-1.0}\,(\alpha_S)\,\mathrm{pb}$ [70].

En la figura 8.1 se presenta un resumen de las medidas de la sección eficaz de $t\bar{t}$ en función de la energía en el centro de masas, tomadas por CMS y CDF y D0, donde se encuentran varias de las medidas presentadas en esta tesis.

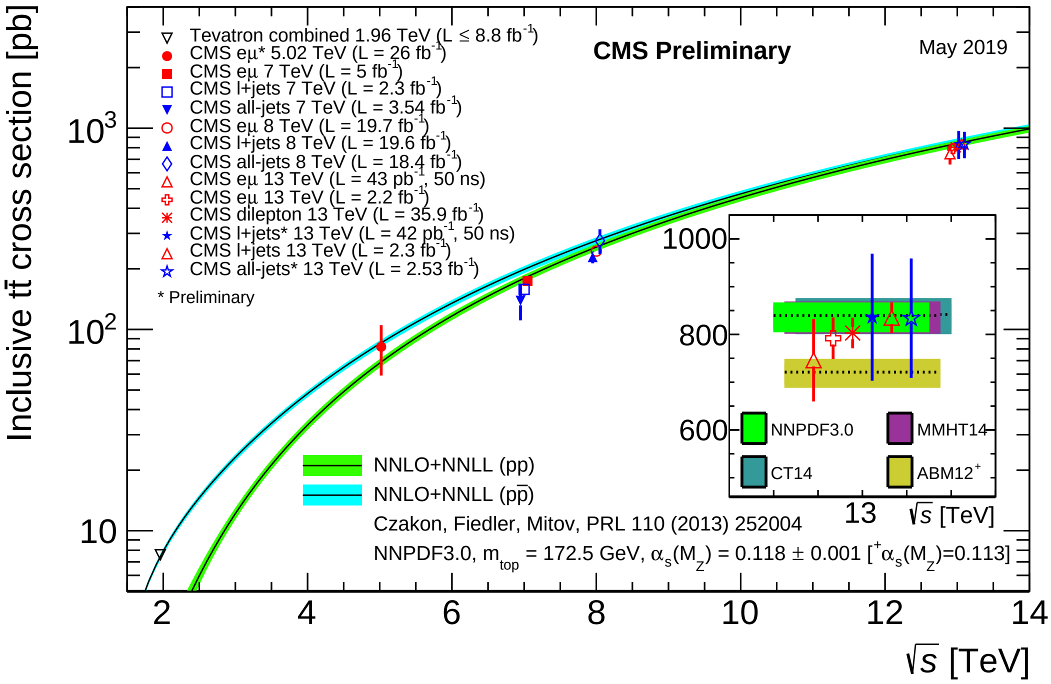

FIGURE 8.1: Resumen de las medidas de la sección eficaz de producción de $t\bar{t}$ en función de la energía en el centro de masas. También se observa la predicción teórica para colisiones protón-protón y protón-antiprotón, incluyendo la medida combinada de la sección eficaz en Tevatrón.

Por último, se ha realizado una búsqueda de partículas supersimétricas, una teoría que puede complementar el ME resolviendo algunas de las cuestiones abiertas de la física de partículas actual. En esta búsqueda, la señal está formada por pares de quarks stop que se desintegran en un par top-antitop y neutralinos con una masa tal que este proceso está degenerado con el proceso $t\bar{t}$ del ME. En este caso, la producción de pares de quarks stop solo puede ser detectada como un exceso de sucesos en la medida de la sección eficaz de $t\bar{t}$. Por ello, la mayor parte de las búsquedas de supersimetría no logran ser sensibles a la presencia de este proceso. El análisis que se presenta en esta tesis es una búsqueda dedicada que aprovecha el esfuerzo hecho para medir con precisión la sección eficaz de producción de sucesos $t\bar{t}$. Además, se utiliza la distribución del observable m_{T2} para aumentar la sensibilidad a la presencia de la señal supersimétrica en el caso de que la diferencia de masas entre el quark stop y el neutralino es diferente de la masa de quark top. En este caso, la producción de stop no está completamente degenerada con $t\bar{t}$ y la distribución de m_{T2} se puede usar para lograr aumentar la sensibilidad del análisis.

No se observa ningún exceso sobre la predicción del fondo del ME. Se establecen límites en la sección eficaz de producción de la producción de pares de quarks stop a un nivel de confianza del 95% para quarks stop con una masa de hasta 208 GeV, en modelos en los que la diferencia de masas entre el quark stop y el neutralino es aproximadamente igual a la masa del quark top. Este resultado representa un importante avance en las búsquedas de supersimetría, alcanzando sensibilidad en una región del espacio de fases donde otras búsquedas no han podido llegar.

Los resultados presentados en esta tesis contribuyen a mejorar el conocimiento que tenemos sobre los más fundamentales aspectos de nuestra naturaleza y a explorar las posibles extensiones a este conocimiento gracias a la búsqueda de nuevas partículas. Además, los estudios sobre el envejecimiento de las cámaras de deriva de CMS permiten planificar el funcionamiento del detector usando un acelerador que incrementará notablemente su luminosidad, impulsando así las fronteras del conocimiento.

Bibliography

[1] S. Chatrchyan et al. The CMS Experiment at the CERN LHC. *JINST*, 3, 2008. doi: 10.1088/1748-0221/3/08/S08004.

[2] V. Khachatryan et al. The phase-2 upgrade of the CMS muon detectors. (CERN-LHCC-2017-012. CMS-TDR-016), Sep 2017. URL `https://cds.cern.ch/record/2283189`.

[3] V. Khachatryan et al. Measurement of the top quark pair production cross section in proton-proton collisions at $\sqrt{s} = 13$ TeV. *Phys. Rev. Lett.*, 116(5), 2016. doi: 10.1103/PhysRevLett.116.052002.

[4] V. Khachatryan et al. Measurement of the $t\bar{t}$ production cross section using events in the eμ final state in pp collisions at $\sqrt{s} = 13$ TeV. *Eur. Phys. J. C*, 77, 2017. doi: 10.1140/epjc/s10052-017-4718-8.

[5] A. M. Sirunyan et al. Measurement of the inclusive $\mathrm{t\bar{t}}$ cross section in pp collisions at $\sqrt{s} = 5.02$ TeV using final states with at least one charged lepton. *JHEP*, 03, 2018. doi: 10.1007/JHEP03(2018)115.

[6] A. M. Sirunyan et al. Measurement of the $\mathrm{t\bar{t}}$ production cross section, the top quark mass, and the strong coupling constant using dilepton events in pp collisions at $\sqrt{s} = 13$ TeV. *Eur. Phys. J. C*, 79, 2019. doi: 10.1140/epjc/s10052-019-6863-8.

[7] Georges Aad et al. Observation of a new particle in the search for the Standard Model Higgs boson with the ATLAS detector at the LHC. *Phys. Lett.*, B716, 2012. doi: 10.1016/j.physletb.2012.08.020.

[8] S. Chatrchyan et al. Observation of a new boson at a mass of 125 GeV with the CMS experiment at the LHC. *Phys. Lett.*, B716, 2012. doi: 10.1016/j.physletb.2012.08.021.

[9] Pierre Ramond. Dual theory for free fermions. *Phys. Rev. D*, 3, 1971. doi: 10.1103/PhysRevD.3.2415.

[10] Yu. A. Golfand and E. P. Likhtman. Extension of the algebra of Poincaré group generators and violation of P invariance. *JETP Lett.*, 13, 1971. URL http://www.jetpletters.ac.ru/ps/1584/article_24309.pdf.

[11] A. Neveu and J. H. Schwarz. Factorizable dual model of pions. *Nucl. Phys. B*, 31, 1971. doi: 10.1016/0550-3213(71)90448-2.

[12] J. Wess and B. Zumino. A Lagrangian model invariant under supergauge transformations. *Phys. Lett. B*, 49, 1974. doi: 10.1016/0370-2693(74)90578-4.

[13] J. Wess and B. Zumino. Supergauge transformations in four-dimensions. *Nucl. Phys. B*, 70, 1974. doi: 10.1016/0550-3213(74)90355-1.

[14] Pierre Fayet. Supergauge invariant extension of the Higgs mechanism and a model for the electron and its neutrino. *Nucl. Phys. B*, 90, 1975. doi: 10.1016/0550-3213(75)90636-7.

[15] Hans Peter Nilles. Supersymmetry, supergravity and particle physics. *Phys. Rept.*, 110, 1984. doi: 10.1016/0370-1573(84)90008-5.

[16] A. M. Sirunyan et al. Search for the pair production of light top squarks in the $e^{\pm}\mu^{\mp}$ final state in proton-proton collisions at $\sqrt{s} = 13\,\text{TeV}$. *JHEP*, 03, 2019. doi: 10.1007/JHEP03(2019)101.

[17] Steven Weinberg. The Search for Unity: Notes for a History of Quantum Field Theory. 1997. URL https://www.jstor.org/stable/20024506.

[18] Michael E. Peskin and Daniel V. Schroeder. An Introduction to quantum field theory. 1995. URL http://www.slac.stanford.edu/~mpeskin/QFT.html.

[19] David Griffiths. Introduction to elementary particles. *Weinheim, Germany: Wiley-VCH (2008) 454 p*, 2008.

[20] Steven Weinberg. A Model of Leptons. *Phys. Rev. Lett.*, 19, 1967. doi: 10.1103/PhysRevLett.19.1264.

[21] F. D. Aaron et al. Combined Measurement and QCD Analysis of the Inclusive $e^{\pm}p$ Scattering Cross Sections at HERA. *JHEP*, 01, 2010. doi: 10.1007/JHEP01(2010)109.

[22] Richard D. Ball et al. Parton distributions for the LHC Run II. *JHEP*, 04, 2015. doi: 10.1007/JHEP04(2015)040.

[23] Richard D. Ball et al. Parton distributions with LHC data. *Nucl. Phys.*, B867, 2013. doi: 10.1016/j.nuclphysb.2012.10.003.

[24] H. Abramowicz et al. Measurement of high-Q2 neutral current deep inelastic e^+p scattering cross sections with a longitudinally polarized positron beam at HERA. *Phys. Rev.*, D87(5), 2013. doi: 10.1103/PhysRevD.87.052014.

[25] F. D. Aaron et al. Inclusive Deep Inelastic Scattering at High Q^2 with Longitudinally Polarised Lepton Beams at HERA. *JHEP*, 09, 2012. doi: 10.1007/JHEP09(2012)061.

[26] H. Abramowicz et al. Combination and QCD Analysis of Charm Production Cross Section Measurements in Deep-Inelastic ep Scattering at HERA. *Eur. Phys. J. C*, 73(2), 2013. doi: 10.1140/epjc/s10052-013-2311-3.

[27] Georges Aad et al. Measurement of inclusive jet and dijet production in pp collisions at $\sqrt{s} = 7\,\text{TeV}$ using the ATLAS detector. *Phys. Rev.*, D86, 2012. doi: 10.1103/PhysRevD.86.014022.

[28] S. Chatrchyan et al. Measurements of differential jet cross sections in proton-proton collisions at $\sqrt{s} = 7\,\text{TeV}$ with the CMS detector. *Phys. Rev.*, D87(11), 2013. doi: 10.1103/PhysRevD.87.112002,10.1103/PhysRevD.87.119902. [Erratum: Phys. Rev.D87,no.11,119902(2013)].

[29] Georges Aad et al. Measurement of the inclusive jet cross section in pp collisions at $\sqrt{s} = 2.76\,\text{TeV}$ and comparison to the inclusive jet cross section at $\sqrt{s} = 7\,\text{TeV}$ using the ATLAS detector. *Eur. Phys. J. C*, 73(8), 2013. doi: 10.1140/epjc/s10052-013-2509-4.

[30] S. Chatrchyan et al. Measurement of the muon charge asymmetry in inclusive pp $\rightarrow$W +X production at $\sqrt{s} = 7\,\text{TeV}$ and an improved determination of light parton distribution functions. *Phys. Rev.*, D90(3), 2014. doi: 10.1103/PhysRevD.90.032004.

[31] Georges Aad et al. Measurement of the transverse momentum distribution of W bosons in pp collisions at $\sqrt{s} = 7\,\text{TeV}$ with the ATLAS detector. *Phys. Rev.*, D85, 2012. doi: 10.1103/PhysRevD.85.012005.

[32] Georges Aad et al. Measurement of the high-mass Drell–Yan differential cross-section in pp collisions at $\sqrt{s} = 7\,\text{TeV}$ with the ATLAS detector. *Phys. Lett.*, B725, 2013. doi: 10.1016/j.physletb.2013.07.049.

[33] S. Chatrchyan et al. Measurement of the differential and double-differential Drell-Yan cross sections in proton-proton collisions at $\sqrt{s} = 7\,\text{TeV}$. *JHEP*, 12, 2013. doi: 10.1007/JHEP12(2013)030.

[34] S. Chatrchyan et al. Measurement of the $t\bar{t}$ production cross section in the dilepton channel in pp collisions at $\sqrt{s} = 7$ TeV. *JHEP*, 11, 2012. doi: 10.1007/JHEP11(2012)067.

[35] S. Chatrchyan et al. Measurement of the $t\bar{t}$ production cross section in the dilepton channel in pp collisions at $\sqrt{s} = 8$ TeV. *JHEP*, 02, 2014. doi: 10.1007/JHEP02(2014)024,10.1007/JHEP02(2014)102. [Erratum: JHEP02,102(2014)].

[36] Georges Aad et al. Measurement of the cross section for top-quark pair production in pp collisions at $\sqrt{s} = 7$ TeV with the ATLAS detector using final states with two high-pt leptons. *JHEP*, 05, 2012. doi: 10.1007/JHEP05(2012)059.

[37] S. Chatrchyan et al. Measurement of associated W + charm production in pp collisions at $\sqrt{s} = 7$ TeV. *JHEP*, 02, 2014. doi: 10.1007/JHEP02(2014)013.

[38] V. N. Gribov and L. N. Lipatov. Deep inelastic ep scattering in perturbation theory. *Sov. J. Nucl. Phys.*, 15, 1972. [Yad. Fiz.15,781(1972)].

[39] Guido Altarelli and G. Parisi. Asymptotic Freedom in Parton Language. *Nucl. Phys.*, B126, 1977. doi: 10.1016/0550-3213(77)90384-4.

[40] Torbjorn Sjöstrand, Stefan Ask, Jesper R. Christiansen, Richard Corke, Nishita Desai, Philip Ilten, Stephen Mrenna, Stefan Prestel, Christine O. Rasmussen, and Peter Z. Skands. An introduction to PYTHIA 8.2. *Comput. Phys. Commun.*, 191, 2015. doi: 10.1016/j.cpc.2015.01.024.

[41] G. Corcella, I. G. Knowles, G. Marchesini, S. Moretti, K. Odagiri, P. Richardson, M. H. Seymour, and B. R. Webber. HERWIG 6: An Event generator for hadron emission reactions with interfering gluons (including supersymmetric processes). *JHEP*, 01, 2001. doi: 10.1088/1126-6708/2001/01/010.

[42] J. Alwall, R. Frederix, S. Frixione, V. Hirschi, F. Maltoni, O. Mattelaer, H. S. Shao, T. Stelzer, P. Torrielli, and M. Zaro. The automated computation of tree-level and next-to-leading order differential cross sections, and their matching to parton shower simulations. *JHEP*, 07, 2014. doi: 10.1007/JHEP07(2014)079.

[43] S. Alioli et al. A general framework for implementing NLO calculations in shower Monte Carlo programs: the POWHEG BOX. *JHEP*, 06, 2010. doi: 10.1007/JHEP06(2010)043.

[44] Stefano Frixione, Paolo Nason, and Carlo Oleari. Matching NLO QCD computations with Parton Shower simulations: the POWHEG method. *JHEP*, 11, 2007. doi: 10.1088/1126-6708/2007/11/070.

[45] Paolo Nason. A new method for combining NLO QCD with shower Monte Carlo algorithms. *JHEP*, 11, 2004. doi: 10.1088/1126-6708/2004/11/040.

[46] E. Re. Single-top Wt-channel production matched with parton showers using the POWHEG method. *Eur. Phys. J. C*, 71, 2011. doi: 10.1140/epjc/s10052-011-1547-z.

[47] B. R. Webber. A QCD Model for Jet Fragmentation Including Soft Gluon Interference. *Nucl. Phys.*, B238, 1984. doi: 10.1016/0550-3213(84)90333-X.

[48] Bo Andersson, G. Gustafson, G. Ingelman, and T. Sjostrand. Parton Fragmentation and String Dynamics. *Phys. Rept.*, 97, 1983. doi: 10.1016/0370-1573(83)90080-7.

[49] Rabindra N. Mohapatra and Goran Senjanovic. Neutrino Mass and Spontaneous Parity Nonconservation. *Phys. Rev. Lett.*, 44, 1980. doi: 10.1103/PhysRevLett.44.912. [,231(1979)].

[50] Douglas Clowe, Marusa Bradac, Anthony H. Gonzalez, Maxim Markevitch, Scott W. Randall, Christine Jones, and Dennis Zaritsky. A direct empirical proof of the existence of dark matter. *Astrophys. J.*, 648, 2006. doi: 10.1086/508162.

[51] Vera C. Rubin and W. Kent Ford, Jr. Rotation of the Andromeda Nebula from a Spectroscopic Survey of Emission Regions. *Astrophys. J.*, 159, 1970. doi: 10.1086/150317.

[52] Douglas Clowe, Anthony Gonzalez, and Maxim Markevitch. Weak lensing mass reconstruction of the interacting cluster 1E0657-558: Direct evidence for the existence of dark matter. *Astrophys. J.*, 604, 2004. doi: 10.1086/381970.

[53] CMS Luminosity Public Results. URL: `https://twiki.cern.ch/twiki/bin/view/CMSPublic/LumiPublicResults`, 2018. Integrated and peak luminosity, 2015-2018 (run 2 only).

[54] V Karimäki, M Mannelli, P Siegrist, H Breuker, A Caner, R Castaldi, K Freudenreich, G Hall, R Horisberger, M Huhtinen, and A Cattai. The CMS tracker system project: Technical Design Report. 1997. URL `https://cds.cern.ch/record/368412`.

[55] V. Khachatryan et al. The CMS electromagnetic calorimeter project: Technical Design Report. 1997. URL `https://cds.cern.ch/record/349375`.

[56] V. Khachatryan et al. The CMS hadron calorimeter project: Technical Design Report. 1997. URL `https://cds.cern.ch/record/357153`.

[57] V. Khachatryan et al. The CMS muon project: Technical Design Report. 1997. URL `https://cds.cern.ch/record/343814`.

[58] A. M. Sirunyan et al. Particle-flow reconstruction and global event description with the CMS detector. *JINST*, 12, 2017. doi: 10.1088/1748-0221/12/10/P10003.

[59] R. Fruhwirth. Application of Kalman filtering to track and vertex fitting. *Nucl. Instrum. Meth.*, A262, 1987. doi: 10.1016/0168-9002(87)90887-4.

[60] Stephanie Baffioni, Claude Charlot, Federico Ferri, David Futyan, Paolo Meridiani, Ivica Puljak, Chiara Rovelli, Roberto Salerno, and Yves Sirois. Electron reconstruction in CMS. Technical Report CMS-NOTE-2006-040, CERN, Geneva, Feb 2006. URL `http://cds.cern.ch/record/934070`.

[61] V. Khachatryan et al. Performance of electron reconstruction and selection with the CMS detector in proton-proton collisions at $\sqrt{s} = 8\,\mathrm{TeV}$. *JINST*, 10(06), 2015. doi: 10.1088/1748-0221/10/06/P06005.

[62] Matteo Cacciari, Gavin P. Salam, and Gregory Soyez. The anti-k_t jet clustering algorithm. *JHEP*, 04, 2008. doi: 10.1088/1126-6708/2008/04/063.

[63] Matteo Cacciari and Gavin P. Salam. Pileup subtraction using jet areas. *Phys. Lett.*, B659, 2008. doi: 10.1016/j.physletb.2007.09.077.

[64] A. M. Sirunyan et al. Identification of heavy-flavour jets with the CMS detector in pp collisions at 13 TeV. *JINST*, 13, 2018. doi: 10.1088/1748-0221/13/05/P05011.

[65] Dorothea Pfeiffer, Georgi Gorine, Hans Reithler, Bartolomej Biskup, Alasdair Day, Adrian Fabich, Joffrey Germa, Roberto Guida, Martin Jaekel, and Federico Ravotti. The radiation field in the Gamma Irradiation Facility GIF++ at CERN. *Nucl. Instrum. Meth.*, A866, 2017. doi: 10.1016/j.nima.2017.05.045.

[66] V. Khachatryan et al. Measurement of the $\mathrm{t\bar{t}}$ production cross section in the eμ channel in proton-proton collisions at $\sqrt{s}$ = 7 and 8 TeV. *JHEP*, 08, 2016. doi: 10.1007/JHEP08(2016)029.

[67] C. Patrignani et al. Review of Particle Physics. *Chin. Phys.*, C40(10), 2016. doi: 10.1088/1674-1137/40/10/100001.

[68] S. Abachi et al. Observation of the top quark. *Phys. Rev. Lett.*, 74, 1995. doi: 10.1103/PhysRevLett.74.2632.

[69] F. Abe et al. Observation of top quark production in $\bar{p}p$ collisions. *Phys. Rev. Lett.*, 74, 1995. doi: 10.1103/PhysRevLett.74.2626.

[70] Michal Czakon, Paul Fiedler, and Alexander Mitov. Total top-quark pair-production cross section at hadron colliders through $O(\alpha_S^4)$. *Phys. Rev. Lett.*, 110, 2013. doi: 10.1103/PhysRevLett.110.252004.

[71] Michal Czakon and Alexander Mitov. Top++: A program for the calculation of the top-pair cross-section at hadron colliders. *Comput. Phys. Commun.*, 185, 2014. doi: 10.1016/j.cpc.2014.06.021.

[72] CMS Collaboration. Investigations of the impact of the parton shower tuning in Pythia 8 in the modelling of $t\bar{t}$ at $\sqrt{s} = 8$ and 13 TeV. CMS Physics Analysis Summary CMS-PAS-TOP-16-021, CERN, 2016. URL `http://cds.cern.ch/record/2235192`.

[73] Rikkert Frederix and Stefano Frixione. Merging meets matching in MC@NLO. *JHEP*, 12, 2012. doi: 10.1007/JHEP12(2012)061.

[74] S. Agostinelli et al. GEANT4—a simulation toolkit. *Nucl. Instrum. Meth. A*, 506, 2003. doi: 10.1016/S0168-9002(03)01368-8.

[75] Ye Li and Frank Petriello. Combining QCD and electroweak corrections to dilepton production in the framework of the FEWZ simulation code. *Phys. Rev. D*, 86, 2012. doi: 10.1103/PhysRevD.86.094034.

[76] Nikolaos Kidonakis. Theoretical results for electroweak-boson and single-top production. *PoS*, DIS2015, 2015.

[77] John M. Campbell, R. Keith Ellis, and Ciaran Williams. Vector boson pair production at the LHC. *JHEP*, 07, 2011. doi: 10.1007/JHEP07(2011)018.

[78] M. V. Garzelli, A. Kardos, C. G. Papadopoulos, and Z. Trocsanyi. $t\bar{t}W$ and $t\bar{t}Z$ hadroproduction at NLO accuracy in QCD with parton shower and hadronization effects. *JHEP*, 11, 2012. doi: 10.1007/JHEP11(2012)056.

[79] V. Khachatryan et al. Event generator tunes obtained from underlying event and multiparton scattering measurements. *Eur. Phys. J. C*, 76, 2016. doi: 10.1140/epjc/s10052-016-3988-x.

[80] A. M. Sirunyan et al. Performance of the CMS muon detector and muon reconstruction with proton-proton collisions at $\sqrt{s} = 13$ TeV. *JINST*, 13, 2018. doi: 10.1088/1748-0221/13/06/P06015.

[81] CMS Collaboration. CMS luminosity measurements for the 2016 data taking period. CMS Physics Analysis Summary CMS-PAS-LUMI-17-001, CERN, 2017. URL `https://cds.cern.ch/record/2257069`.

[82] V. Khachatryan et al. Jet energy scale and resolution in the CMS experiment in pp collisions at 8 TeV. *JINST*, 12(02), 2017. doi: 10.1088/1748-0221/12/02/P02014.

[83] CMS Collaboration. Jet algorithms performance in 13 TeV data. CMS Physics Analysis Summary CMS-PAS-JME-16-003, CERN, 2017. URL `http://cds.cern.ch/record/2256875`.

[84] A. M. Sirunyan et al. Measurement of the inelastic proton-proton cross section at $\sqrt{s} = 13\,\text{TeV}$. *JHEP*, 07, 2018. doi: 10.1007/JHEP07(2018)161.

[85] A. M. Sirunyan et al. Measurements of differential cross sections of top quark pair production as a function of kinematic event variables in proton-proton collisions at $\sqrt{s} = 13\,\text{TeV}$. *JHEP*, 06, 2018. doi: 10.1007/JHEP06(2018)002.

[86] Peter Skands, Stefano Carrazza, and Juan Rojo. Tuning PYTHIA 8.1: the Monash 2013 Tune. *Eur. Phys. J. C*, 74, 2014. doi: 10.1140/epjc/s10052-014-3024-y.

[87] CMS Luminosity Calibration for the pp Reference Run at $\sqrt{s} = 5.02\,\text{TeV}$. Technical Report CMS-PAS-LUM-16-001, CERN, Geneva, 2016. URL `http://cds.cern.ch/record/2235781`.

[88] M. Aaboud et al. Search for direct top squark pair production in final states with two leptons in $\sqrt{s} = 13\,\text{TeV}$ pp collisions with the ATLAS detector. *Eur. Phys. J. C*, 77, 2017. doi: 10.1140/epjc/s10052-017-5445-x.

[89] Georges Aad et al. ATLAS Run 1 searches for direct pair production of third-generation squarks at the Large Hadron Collider. *Eur. Phys. J. C*, 75, 2015. doi: 10.1140/epjc/s10052-015-3726-9.

[90] Georges Aad et al. Search for top squark pair production in final states with one isolated lepton, jets, and missing transverse momentum in $\sqrt{s} = 8\,\text{TeV}$ pp collisions with the ATLAS detector. *JHEP*, 11, 2014. doi: 10.1007/JHEP11(2014)118.

[91] Georges Aad et al. Search for direct top-squark pair production in final states with two leptons in pp collisions at $\sqrt{s} = 8\,\text{TeV}$ with the ATLAS detector. *JHEP*, 06, 2014. doi: 10.1007/JHEP06(2014)124.

[92] Morad Aaboud et al. Search for top squarks in final states with one isolated lepton, jets, and missing transverse momentum in $\sqrt{s} = 13\,\text{TeV}$ pp collisions with the ATLAS detector. *Phys. Rev. D*, 94, 2016. doi: 10.1103/PhysRevD.94.052009.

[93] A. M. Sirunyan et al. Search for top squark pair production in pp collisions at $\sqrt{s} = 13\,\text{TeV}$ using single lepton events. *JHEP*, 10, 2017. doi: 10.1007/JHEP10(2017)019.

[94] A. M. Sirunyan et al. Search for top squarks and dark matter particles in opposite-charge dilepton final states at $\sqrt{s} = 13$ TeV. *Phys. Rev. D*, 97, 2018. doi: 10.1103/PhysRevD.97.032009.

[95] S. Chatrchyan et al. Search for top-squark pair production in the single-lepton final state in pp collisions at $\sqrt{s} = 8\,\text{TeV}$. *Eur. Phys. J. C*, 73, 2013. doi: 10.1140/epjc/s10052-013-2677-2.

[96] V. Khachatryan et al. Search for direct pair production of scalar top quarks in the single- and dilepton channels in proton-proton collisions at $\sqrt{s} = 8\,TeV$. *JHEP*, 07, 2016. doi: 10.1007/JHEP07(2016)027.

[97] V. Khachatryan et al. Search for top squark pair production in compressed-mass-spectrum scenarios in proton-proton collisions at $\sqrt{s}$ = 8 TeV using the α_{T} variable. *Phys. Lett. B*, 767, 2017. doi: 10.1016/j.physletb.2017.02.007.

[98] A. M. Sirunyan et al. Searches for pair production of third-generation squarks in $\sqrt{s} = 13\,\text{TeV}$ pp collisions. *Eur. Phys. J. C*, 77, 2017. doi: 10.1140/epjc/s10052-017-4853-2.

[99] A. M. Sirunyan et al. Search for direct production of supersymmetric partners of the top quark in the all-jets final state in proton-proton collisions at $\sqrt{s} = 13\,\text{TeV}$. *JHEP*, 10, 2017. doi: 10.1007/JHEP10(2017)005.

[100] A. M. Sirunyan et al. Search for supersymmetry in proton-proton collisions at 13 TeV using identified top quarks. *Phys. Rev. D*, 97, 2018. doi: 10.1103/PhysRevD.97.012007.

[101] CMS Supersymmetry Physics Results. URL: `https://twiki.cern.ch/twiki/bin/view/CMSPublic/PhysicsResultsSUS`, 2018.

[102] Georges Aad et al. Measurement of the $\mathrm{t\bar{t}}$ production cross-section using $e\mu$ events with b-tagged jets in pp collisions at $\sqrt{s}$ = 7 and 8 TeV with the ATLAS detector. *Eur. Phys. J. C*, 74, 2014. doi: 10.1140/epjc/s10052-016-4501-2. [Addendum: *Eur. Phys. J. C* **76**(2016) 642].

[103] Georges Aad et al. Measurement of spin correlation in top-antitop quark events and search for top squark pair production in pp collisions at $\sqrt{s} = 8\,\text{TeV}$ using the ATLAS detector. *Phys. Rev. Lett.*, 114, 2015. doi: 10.1103/PhysRevLett.114.142001.

[104] Savas Dimopoulos and Howard Georgi. Softly broken supersymmetry and SU(5). *Nucl. Phys. B*, 193, 1981. doi: 10.1016/0550-3213(81)90522-8.

[105] R. K. Kaul and P. Majumdar. Cancellation of quadratically divergent mass corrections in globally supersymmetric spontaneously broken gauge theories. *Nucl. Phys. B*, 199, 1982. doi: 10.1016/0550-3213(82)90565-X.

[106] H. Georgi, Helen R. Quinn, and Steven Weinberg. Hierarchy of Interactions in Unified Gauge Theories. *Phys. Rev. Lett.*, 33, 1974. doi: 10.1103/PhysRevLett.33.451.

[107] S. Dimopoulos, S. Raby, and Frank Wilczek. Supersymmetry and the Scale of Unification. *Phys. Rev.*, D24, 1981. doi: 10.1103/PhysRevD.24.1681.

[108] Marcela Carena, S. Pokorski, and C. E. M. Wagner. On the unification of couplings in the minimal supersymmetric Standard Model. *Nucl. Phys.*, B406, 1993. doi: 10.1016/0550-3213(93)90161-H.

[109] Johan Alwall, Philip Schuster, and Natalia Toro. Simplified models for a first characterization of new physics at the LHC. *Phys. Rev. D*, 79, 2009. doi: 10.1103/PhysRevD.79.075020.

[110] Daniele Alves. Simplified models for LHC new physics searches. *J. Phys. G*, 39, 2012. doi: 10.1088/0954-3899/39/10/105005.

[111] Jonathan Richard Ellis. Supersymmetry for Alp Hikers. (hep-ph/0203114. CERN-TH-2002-052), Mar 2002. URL `https://cds.cern.ch/record/542168`.

[112] Hsin-Chia Cheng and Zhenyu Han. Minimal kinematic constraints and m_{T2}. *JHEP*, 12, 2008. doi: 10.1088/1126-6708/2008/12/063.

[113] Christoph Borschensky, Michael Krämer, Anna Kulesza, Michelangelo Mangano, Sanjay Padhi, Tilman Plehn, and Xavier Portell. Squark and gluino production cross sections in pp collisions at $\sqrt{s}$ = 13, 14, 33 and 100 TeV. *Eur. Phys. J. C*, 74, 2014. doi: 10.1140/epjc/s10052-014-3174-y.

[114] W. Beenakker, S. Brensing, M. n Kramer, A. Kulesza, E. Laenen, L. Motyka, and I. Niessen. Squark and gluino hadroproduction. *Int. J. Mod. Phys. A*, 26, 2011. doi: 10.1142/S0217751X11053560.

[115] Wim Beenakker, Silja Brensing, Michael Kramer, Anna Kulesza, Eric Laenen, and Irene Niessen. Soft-gluon resummation for squark and gluino hadroproduction. *JHEP*, 12, 2009. doi: 10.1088/1126-6708/2009/12/041.

[116] A. Kulesza and L. Motyka. Soft gluon resummation for the production of gluino-gluino and squark-antisquark pairs at the LHC. *Phys. Rev. D*, 80, 2009. doi: 10.1103/PhysRevD.80.095004.

[117] A. Kulesza and L. Motyka. Threshold resummation for squark-antisquark and gluino-pair production at the LHC. *Phys. Rev. Lett.*, 102, 2009. doi: 10.1103/PhysRevLett.102.111802.

[118] W. Beenakker, R. Hopker, M. Spira, and P. M. Zerwas. Squark and gluino production at hadron colliders. *Nucl. Phys. B*, 492, 1997. doi: 10.1016/S0550-3213(97)80027-2.

[119] A. M. Sirunyan et al. Search for physics beyond the standard model in events with two leptons of same sign, missing transverse momentum, and jets in proton–proton collisions at $\sqrt{s} = 13\,\text{TeV}$. *Eur. Phys. J. C*, 77(9), 2017. doi: 10.1140/epjc/s10052-017-5079-z.

[120] Glen Cowan, Kyle Cranmer, Eilam Gross, and Ofer Vitells. Asymptotic formulae for likelihood-based tests of new physics. *Eur. Phys. J. C*, 71, 2011. doi: 10.1140/epjc/s10052-011-1554-0.

[121] Thomas Junk. Confidence level computation for combining searches with small statistics. *Nucl. Instrum. Meth. A*, 434, 1999. doi: 10.1016/S0168-9002(99)00498-2.

[122] Alexander L. Read. Presentation of search results: The CL_s technique. *J. Phys. G*, 28, 2002. doi: 10.1088/0954-3899/28/10/313.

[123] The ATLAS Collaboration, The CMS Collaboration, The LHC Higgs Combination Group. Procedure for the LHC Higgs boson search combination in Summer 2011. Technical Report CMS-NOTE-2011-005, ATL-PHYS-PUB-2011-11, 2011. URL `https://cds.cern.ch/record/1379837`.